HYBRID COMPUTATIONAL MODELING OF THERMOMAGNETIC MATERIAL SYSTEMS

A Thesis
Presented to
The Academic Faculty

by

Sookyung Kim

In Partial Fulfillment
of the Requirements for the Degree
Doctor of Philosophy in
Material Science and Engineering

School of Material Science and Engineering
Georgia Institute of Technology
May, 2017

HYBRID COMPUTATIONAL MODELING OF THERMOMAGNETIC MATERIAL SYSTEMS

Approved by:

Prof. Hamid Garmestini, Advisor
School of Material Science and Engineering
Georgia Institute of Technology

Prof. Seung Soon Jang
School of Material Science and Engineering
Georgia Institute of Technology

Prof. Richard Fujimoto
School of Computational Science and Engineering
Georgia Institute of Technology

Prof. Chaitanya S. Deo
School of Mechanical Engineering
Georgia Institute of Technology

Dr. Lorin Benedict
Physical and Life Sciences Directorate
Lawrence Livermore National Lab.

Dr. Mohammad A. Khaleel
Energy and Environmental Sciences Directorate
Oak Ridge National Lab.

Date Approved: Nov 11, 2016

To my Mom and Dad

ACKNOWLEDGEMENTS

First and foremost, I want to give my regard and thank to advisor Hamid Garmestani. It has been a great honor and privilege for me to be his student. I still remember the moment that I first visit Georgia Tech to meet him and talk about my previous research projects on DFT in Columbia University. He gave me a chance to present my previous research works, and understood my ambition to continue my study. I know it would not be easy for him to give an opportunity to me, who already went through tough time in Ph.D program from another school. However, he trusted me and accepted me as his student by dealing with all difficulties and obstacles without any condition, just because he trusted my ambition to continue research. Since that moment, he has taught me, both consciously and unconsciously with unconditional support, how good material research is done. I appreciate all his contributions to finish my Ph.D. successfully. He was the first person in academia who puts such a strong trust on me. Because he trusted me, I have been able to have faith in myself even in hard time. He is really a person who changed my life. Thank you, Prof. Garmestani.

The collaborators in Lawrence Livermore National Laboratory have contributed immensely to my thesis work in spin thermodynamic simulation using Heisenberg Model. The magnetism group in LLNL has been a source of good advice and collaboration. I am especially grateful to Dr. Lorin Benedict and Dr. Mike Surh in LLNL who stuck it out to solve difficult research questions with me, and teach me how to solve the difficult problems in material physics step by step. We worked together on the spin dynamic simulations for about one and half years. Dr. Benedict supported magnetic research project in my summer internship at LLNL as the PI. With brilliant mind in physics, and enthusiasm, he guided my research in every way. I very much appreciated his enthusiasm, intensity, willingness to advise my research and support development of my research career in every way. Dr. Surh always stuck it out to difficult research questions and patiently guided me how to solve those problems. The joy and enthusiasm I had for research discussion with him was contagious and motivated me to pursue post-doc position in LLNL after Ph.D program. I want to thank Dr. Surh for being such a great mentor and excellent example he has provided as a scientific

role-model.

In regards to the MnBi and MnSb project, I thank Dr. Kim Ferris at Pacific Northwest National Laboratory and Dr. Dongsheng Li (formerly at PNNL). They gave me advice on DFT work in early stage of the rare-earth replacement material development project. My fundamental knowledges on computational chemistry has been owing from Dr. Ferris a lot. He taught me the key physical concepts in DFT, and shared with various lessons he learned in his long research career. I would like to thank for his effort and time that he puts to nurture me as a scientist.

In my later work of GPU parallelization of Heisenberg model, I am particularly indebted to Prof. Richard Fujimoto and Robert Lee. Prof. Fujimoto guided the computing side of my thesis work by sharing some of his insights. I very appreciated his support and willingness to allow me to use the computing resources such as Georgia Tech GPU clusters. Robert Lee wrote the initial GPU code to parallelize Monte-Carlo spin simulation using Ising model. He also provided relevant support for Heisenberg model in GPU programing and his insight on high performance computing. It was my pleasure to work with him as a team in Modeling and Simulation class.

For this dissertation I would like to thank my committee members: Prof. Seung Soon Jang, Prof. Richard Fujimoto, Prof. Chaitanya S. Deo, Dr. Mohammad A. Khaleel and Dr. Lorin Benedict for their time, interest, helpful feedbacks, and insightful questions.

Lastly, I would like to express my gratitude and love to my family for all their love and encouragement. Words cannot express how grateful I am to, my mother, and father for all of the sacrifices that they have made on my behalf. They raised me with a love and supported me in every way, spiritually and financially, throughout long years of my education even from South Korea. For my brother and sister who always in my heart encouraged me to do my best even during tough times in the Ph.D. pursuit. And most of all for my beloved husband Joonseok Lee whose faithful support during the all stages of this Ph.D. is so appreciated. Finding him and getting married with him is one of the best outcomes from years of graduate education. I would like to express my love and deep appreciation to him.

Sookyung Kim

Georgia Institute of Technology

December, 2016

Contents

List of Tables

List of Figures

SUMMARY

It is clear that current knowledge of computational material modeling for engineering demands accurate prediction of thermo-magnetic properties of material. Material design and discovery for permanent magnet material alternative to expensive rare-earth element requires accurate modeling of thermo-magnetism. The engineering task of exploring stainless steel also covers physical quantities on thermo-magnetic properties which can be benefited from modeling methods.

Different computational modeling approaches should be considered and selected in a way that fit the specific material systems. In general, thermo-magnetic properties of materials should benefit from ab-initio DFT calculation in some degree. However, DFT alone has the limitation in fully modeling finite temperature properties. Firstly, the concept of statistical physics such as magnetic excitation and magnetic spin interactions are not fully considered in DFT. Secondly, the nature of atomic scale simulation made it difficult to extend to meso-scale simulation. Therefore, a promising route toward this goal is the combination of DFT with concepts of statistical physics, which was shown to yield accurate predictions for a wide range of magnetic and nonmagnetic materials. In the present work, informative study of exploring the material modeling landscapes based on ab-intio techniques for different material systems have been carried out. In this work, we review and compare various computational modeling techniques currently available for predicting thermo-magnetic properties of materials. Many computational modeling approaches are applied in the different systems with the way in which fits the best. With these extensions, I propose new computational modeling routine based currently available methods. Specifically, I propose hybrid methodologies combining DFT and Heisenberg Monte Carlo. A new

Program combining CPA-KKR data and Heisenberg Monte Carlo has been developed specifically for $(Fe_{1-x}Co_x)_2B$ system, and the physical picture of magnetic spin fluctuation in permanent magnetic system has been modeled with high accuracy based on the importance sampling. Also, I propose a new quantum-mechanically driven computational material discovery framework for stainless steel.

The proposed work includes:

1. Predicting thermo-magentic properties of $MnBi$ considering thermal fluctuation of magnetic spin moment using cold-smearing method based first-principle DFT calculation, and compare the important figure of merits with $MnSb$.

2. Predicting thermo-magentic properties of $(Fe_{1-x}Co_x)_2B$ in finite temperature by different Co-concentration using hybrid modeling method combining Green function based KKR-CPA calculation and Monte Carlo simulation based on Heisenberg model.

3. Predicting thermo-magentic properties of austenitic $Fe - Cr - Ni$ stainless steels in finite temperature by changing chemical configuration of alloy using in-house material discovery framework combining DFT and Monte Carlo simulation based on LSF model.

4. Implementing parallel and distributed simulation technique, specially GPU application, in our Heisenberg Monte-Carlo simulation and improve efficiency to predict thermo-magnetic properties in a large atomic system, which is more than several millions of atoms.

By this thorough approach combining Monte-Carlo, KKR-CPA method and ground state DFT, we can achieve our aim to understand the theoretical origin of thermo-magnetic properties of different material systems.

Chapter I

INTRODUCTION

A modern computational material science covers a large variety of physical quantities that need to be optimized for special applications. Specifically, the modeling thermo-magnetic properties of magnetic material are significant for engineering task.

As the first example, the engineering task of exploring the hard permanent magnetic materials is of high interest for computational material modeling. The diverse landscape of engineering application of permanent magnetic materials includes electronic motor application such as maglev train, wind power generator, magnetic memory, and so on. Rare Earth elements such as Nb and Sm are widely used for engineering application. However, expensive cost and insufficient amount of mining site of Rare Earth elements leads the recent interest in searching for permanent magnet materials for engineering applications that are alternatives to Rare-earth elements.

In order to use hard permanent magnet for those applications mentioned above, there are two important design criteria that the candidate material should achieve. Firstly, the material should be able to store large magnetic energy product inside. Secondly, the material should be able to sustain its strong magnetism even in reasonably high temperature. As various materials are explored for their potential applicability in this regard, important figures-of-merit include the energy product related to the area enclosed by the magnetic hysteresis loop and the Curie temperature, T_c. Only a material with a sizable energy product can perform useful work on its surroundings, and the temperature at which this work is performed must be comfortably below the temperature at which its total magnetic moment disappears. While T_c is largely a function of the size of the near-neighbor exchange energies, the energy product, which is closely related to the coercivity, is a multi-scale property, which reflects the tendency of magnetic domains to resist reorientation when placed in an external field, which is misaligned with them. This complex physics of domain wall structure, motion, and pinning is all dependent in part on a microscopic property: the magneto crystalline anisotropy energy (MAE), the energy required to reorient the electron spins in a ferromagnet from easy-to hard-axis directions [81, 48]. Though the energy

product involves much more than the MAE, it is hard to imagine a material with a sizable energy product that does not also have a significant uni-axial MAE. Indeed, permanent magnets in wide industrial use, such as Sm_2Co_{17} and $Nd_2Fe_{14}B$, possess fairly large MAEs [94] resulting from the interplay between the large spin-orbit interaction provided by the RE element together with the enhanced crystal field splitting in these tetragonal structures. There are several compounds to exhibit large MAE other than Rare Earth compounds. For instance, $CoPt$, $FePt$ [94], and the recently studied Li_2FeN_5 [5] are just a few examples of materials with anisotropies which rival or even exceed those of the permanent magnets in wide use. Therefore, computational modeling of rare earth substitutes requires optimization of important physical figure of merits, such as large coercivity, large magnetic anisotropy energy and high Curie temperature. Therefore, sophisticated computational modeling effort is required to accurately predict the thermo-magnetic properties of magnetic materials such as spin-orbit interaction and structural thermal-phase transition.

As the second example, the engineering task of exploring the stainless steel also covers physical quantities on thermo-magnetic properties. The importance of this class of steels in many applications motivates investigations for finding efficient production and shaping methods. Shaping steels under shear stresses involves plastic deformation, a process where the stacking-fault energy (SFE) has a well-known influence [26, 30, 3]. The SFE, in turn, depends on temperature and on the composition of the alloy [108, 110, 109], making it particularly important when considering the thermal treatments and shaping of the metal at high temperatures. In particular, SFE of Fe-Cr-Ni stainless steel, which has been widely used as baseline material for balance of plant applications (BOP) on board fuel cell electric vehicles (FCEVs) is known as largely influenced by the temperature and the chemical composition of alloy. Although temperature dependence of the SFE is influenced by many parameters, in $Fe-Cr-Ni$ stainless steel, it has been reported the magnetic contribution on SFE due to thermo-magnetic fluctuation of magnetic moment of each element take the significant effect [108]. Thus, thermo-magnetic effect of each material in steel should be thoroughly modeled in computational steel design.

From the previous two example mentioned above, it is clear that current knowledge of computational material modeling for engineering task demands accurate prediction of thermo-magnetic properties of material. Then, how can we computationally model the thermo-magnetic properties of system with high precision? In general, the

problem of predicting thermo-magnetic properties of material should benefit from ab-initio electronic structure calculation. In the case of searching rare-earth replacement permanent magnet alternatives, Curie temperature (T_c) and magnetic anisotropic energy (MAE) can be predicted based on DFT. For computational design of steel, there is few ab-initio study on the evaluation of the SFE and the γ-surface in steels with interstitial alloying elements have already been published [52, 1].

There are, however, important challenges connected with such approaches based on DFT that need to be carefully addressed, especially when we calculate thermo-magnetic properties of material. On the one hand, DFT is well known to be particularly suitable for ground state properties of materials. A ground state analysis is however not sufficient for hard permanent magnets or steels, because permanent magnet should be studied up to the very high curie temperature and steels are processed for temperatures ranging from room temperature up to the melting point. An extension to finite temperatures is particularly evident for the presently hot topic of high temperature applications of hard permanent material or steels as, e.g., urgently needed for next generation magnetic device or power plants to sustain their properties in high temperature. Therefore, DFT is not sufficient to predict properties of permanent magnets or stainless steel in finite temperature.

Also, current computational material modeling effort indicates that extreme demands with respect to the precision and accuracy of the methods need to be satisfied, in order to make truly profitable predictions in the prediction of thermo-magnetic properties. It is known that DFT-based quantum-mechanically guided materials design allow a reliable prediction of electronic structure of material with high accuracy. However, the concept of statistical physics such as magnetic excitation and magnetic spin interaction, being of utmost importance for the description of magnetic anisotropic effect of permanent magnets or stacking fault energy of stainless steels, are not fully considered in DFT calculation and remain challenging to incorporate with DFT.

There have been many efforts on theoretical modeling of spin fluctuation in material based on DFT. Recent work of DFT-based fixed spin moment (FSM) electronic structure calculations treats magnetic spin fluctuation in materials close to magnetic order classically [98]. In this method, Landau-Ginzburg-like energy fluctuation is written down, and constructed free energy includes terms describing the interaction between the fluctuations (the mode-mode coupling) and properties such as the static susceptibility, specific heat and resistivity calculated. Then, fixed spin moment electronic

structure calculations can be used to determine the coefficients in this functional. Other than FSM calculation, there have been many informative studies carried out with DFT basis. However, those calculations with such a DFT basis still remain qualitative investigations mainly due to the lack of prescription for the effective number of modes to include in the theory and its variation with temperature [68, 79]. It has been also criticized that Stoner single-particle excitation effect are largely ignored. Especially, in the case of problem of searching reduced Rare Earth permanent magnet alternatives, it is much difficult to use DFT as the computational modeling framework. Because Rare Earth compounds themselves present a formidable challenge, owing to the fact that they often possess narrow-band f-electron levels in the neighborhood of their Fermi energies, which are notoriously difficult to treat predicatively. Various additions to density functional theory (DFT) such as DFT+U have been applied to the prediction of MAE in RE magnets [61, 99], but it is still unclear if such mean-field extensions are indeed suitably predictive for the purpose of designing new materials [8].

Alternatively, widely used quantum Monte Carlo (QMC) approach, the quantum-mechanical extension of statistical modeling approach of materials, can be considered as the method to predict thermo-magnetic fluctuations in finite temperature. However, QMC has a limited applicability due to the so-called negative sign problem. [42, 67]. As a result, for realistic systems such as bcc iron, which are characterized by long-ranged positive as well as negative exchange integrals [82], a QMC solution of Heisenberg Hamiltonian, is generally not feasible.

To sum up, a key prerequisite for the quantum-mechanically guided material design for engineering task of high accuracy and efficiency requires reliable prediction of thermo-magnetic material properties. Different of computational modeling approaches should be considered and selected in a way that fit the best to the specific material systems. In general, thermo-magnetic properties of material should benefit from ab-initio DFT calculation in some degree. However, DFT alone have the limitation in fully modeling finite temperature properties and in considering accurate magnetic spin fluctuation. A promising route toward this goal is the combination of DFT with concepts of statistical physics, which was shown to yield accurate predictions for a wide range of magnetic and nonmagnetic materials [95, 18, 92].

In present work, informative study of exploring the material modeling landscapes

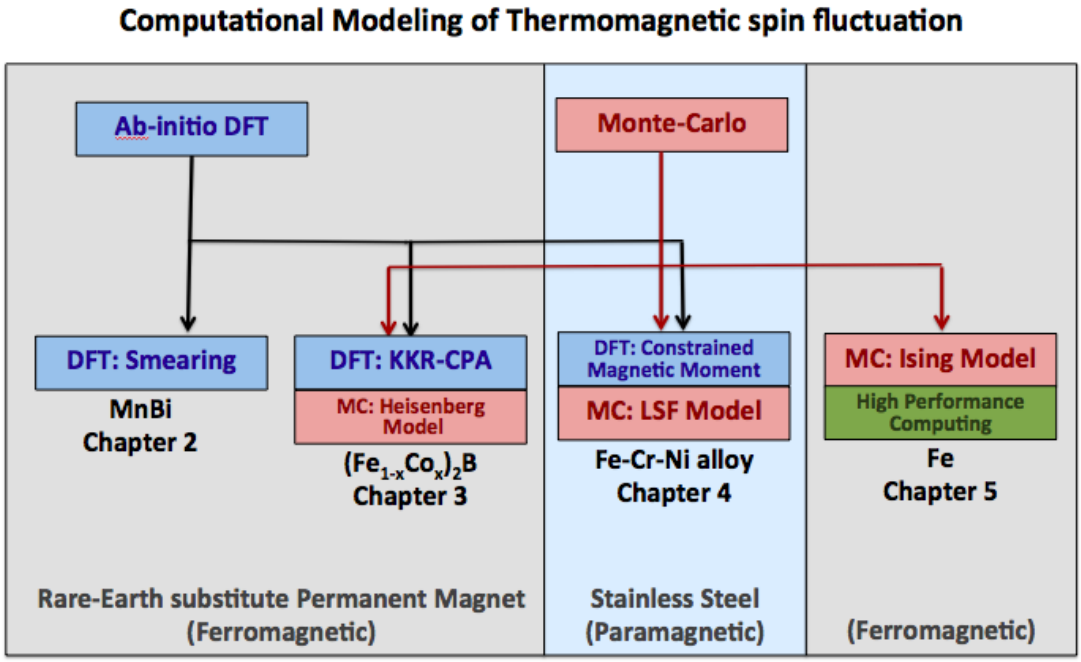

Figure 1.1: Overview of the computational modeling of thermomagnetic spin fluctuation

based ab-intio techniques for different material systems has been carried out. Figure 1.1 shows the brief overview of this work which includes the various computational modeling methods approached for different material systems to predict thermomagnetic properties.

There are two aims of this work. First, I review and compare various computational modeling techniques currently available for predicting thermo-magnetic properties of materials, such as ab-initio DFT, Monte-Carlo methods incorporated with DFT, classical spin Mote Carlo method. Those computational modeling approaches are applied differently for distinct material systems and compared each other. Second, I propose new computational modeling routine based on currently available methods. Specifically, I propose hybrid computational method combining DFT and Heisenberg Monte Carlo. New Program combining CPA-KKR data and Heisenberg Monte Carlo has been developed specifically for $(Fe_{1-x}Co_x)_2B$ system, and the physical picture of magnetic spin fluctuation in permanent magnetic system has been modeled with high accuracy based on importance sampling. Also, I propose new quantum-mechanically driven computational material discovery framework for stainless steel. This framework helps to predict stacking fault energy of stainless steel in high precision with considering contribution from magnetic entropy driven by thermo-magnetic

spin fluctuation. For this, I developed program combining DFT-based data encryption, polynomial data fitting tool and classical Monte-Carlo simulation based on LSF model.

This work is organized as follows. From Chapter 2 to Chapter 4, I present works using DFT and DFT based Monte-Carlo method. Specifically, to calculate the thermodynamic properties of distinct systems in high accuracy, different modeling schemes have been applied for each material system. In Chapter 5, I present high performance computing effort to accelerate Monte-Carlo simulation using parallelization scheme and GPU for simple ferromagnetic Fe system.

Firstly, in Chapter 2, thermo-magnetic properties of $MnBi$, one of the candidate materials for rare-earth substitute, has been predicted. For the $MnBi$ binary alloy, which has been considered thermal smearing of electronic density of state may be the significant factor in its thermo-magnetic properties, DFT-based smearing method has been used.

Secondly, in Chapter 3, thermo-magnetic properties of $(Fe_{1-x}Co_x)_2B$ system, one of the candidate materials for Rare-earth substitute, has been predicted. For $(Fe_{1-x}Co_x)_2B$, the magnetic Heisenberg systems, where magnetic spin fluctuation is utmost important factor in its thermo-magnetic properties, we propose new hybrid modeling routines combining green function based KKR-CPA calculation, classical Monte-Carlo and DFT. Current knowledge indicates that an exact analytical solution of Heisenberg Hamiltonian in realistic system is not known. However, effective classical Monte-Carlo techniques can be used to provide the numerically exact solution for the given set of coupling coefficient, J_{ij}, parameters. As those coupling coefficients can be obtained from the green-function based KKR-CPA calculation, the magnetic free-energy contribution of system with localized magnetic moment can be captured by the mapping of obtained temperature dependent magnetic moment from classical Monte-Carlo onto DFT calculation. This procedure is divided into three steps: first, we calculate coupling coefficients between each magnetic spin moment in system by KKR-CPA calculation. Second, we perform classical Monte-Carlo simulation based on Heisenberg model using obtained coupling coefficients from KKR-CPA. As a result of Monte-Carlo, we obtain magnetic moments at finite temperature. Third, the obtained localized magnetic moments are mapped to DFT calculation to obtain physical figure of merits such as T_c and MAE.

Thirdly, in Chapter 4, magnetic contribution of stacking fault energy of $Fe-Cr-Ni$ stainless steel has been predicted. For the stainless steel alloys, such as Fe-Cr-Ni system, where the system is random alloy with paramagnetic disordered local magnetic (DLM) state, a simple longitudinal spin fluctuation (LSF) model, which assumes the transverse spin fluctuation (the orientation of magnetic moment) always follow the completely disordered configuration and only consider longitudinal spin fluctuation (the size of the magnetic moment), has been used. For modeling the stacking fault energy of austenite $Fe-Cr-Ni$ stainless steel system, we have developed new quantum-mechanically driven computational material discovery framework combining DFT, polynomial data fitting of free energy and classical Monte-Carlo simulation based on LSF model. This procedure is divided into four steps: first, we calculate complete disordered snapshot of magnetic moment spins in system by constraining spins as paramagnetic state using DFT. Second, we constrain the magnitude of magnetic moment of only single atom of system from 0 to maximum value while the configurations of other elements are fixed as obtained from first step and calculate the free energy. By stretching magnitude of moment only one atom at a time and iterate this procedure for every atom, the free energy curves by magnitude of moment for all atoms are obtained. Third, temperature dependent magnetic moment of each atom is simulated by classical Monte-Carlo simulation based on LSF model. For each distinct atom, different free energy curve obtained. Fourth, from obtained magnetic moment of each atom at finite temperature, the magnetic contribution of stacking fault energy is derived using the formulation of temperature dependent magnetic entropy.

Fourthly, in Chapter 5, I propose parallelized Monte-Carlo simulation scheme for Ising model using checkerboard algorithm and GPU. For the simple ferromagnetic binary material, such as simple bcc Iron system, where magnetic frustrations are weak or absent, we used approximated simple Ising model for classical Monte-Carlo simulation. In particular, for this simplified Ising model, high performance computing feature to parallelize classical Monte-Carlo simulation can be easily implemented. I propose the parallelization scheme using GPU and checkerboard algorithm. Thermomagnetic property of BCC Iron has been compared between sequential simulation and accelerated parallel simulation. Then, the maximum speed up with optimized memory scheme and optimized computing parameters has been reported. As a result, more than 200 times accelerated Monte-Carlo simulation using GPU presents almost

identical thermo-magnetic curve with sequential Monte-Carlo simulation in the test case of million of Irons system.

Finally, the conclusions for this study are presented in the last chapter of the work.

Chapter II

THERMOMAGNETIC PROPERTIES OF $MNBI$ USING COLD-SMEARING METHOD

2.1 Motivation

$MnBi$ has emerged as a viable candidate to replace current rare-earth permanent magnets. Extensive experimental studies have shown that $MnBi$ is a strong ferromagnetic compound with a 2.0 T coercive force and a 4.6 MGOe energy product at 400K in the $NiAs$-type hexagonal structure as the ordered low temperature phase (LTP) [89, 114]. More importantly, $MnBi$ has a positive temperature coefficient of coercivity, a valuable trait for applications where magnetic power needs to be maintained at elevated temperatures. Phase transformation in $MnBi$ from a ferromagnetic to a paramagnetic phase occurs at 633K upon heating, and inversely at 613K during cooling. The difference between the transition temperatures is due to the range of cooling processes required to recover the disordered high temperature phase (HTP) from the ordered low temperature phase (LTP). Compared to the LTP form of $MnBi$, there are relatively few investigations of the properties at higher temperatures. From the HTP transition upwards, Guillaud proposed an antiferromagnetic state up to 718K followed by a paramagnetic state [35]. Neutron diffraction investigations on the phase transformations of $MnBi$ conducted by Roberts [90] concluded that the high temperature phase ($> 718K$) was paramagnetic and disordered, with 10% of the Mn atoms moving into the large trigonal bipyramidal holes of the $NiAs$-type structure.

The magnetic anisotropies of $MnBi$ and $MnSb$ are similar in terms of spin alignment, but the difference in the transition temperatures for spin alignment is large. The temperature dependence of the angle between the magnetic moment direction and the c-axis can be determined accurately from the neutron data refinement. From the data analysis of neutron and X-ray powder diffraction data using the program named FULLPROF [114] reported that c-axis is the easy direction of magnetization at high temperatures due to the magnetic moment alignment of Mn. In $MnSb$ the magnetic moment flips into the $a - b$ plane (basal plane) at 510K. The magnetic moment of

$MnBi$ gradually deviates from the c-axis below 142K, and flips into the $a-b$ plane at 90K. Several recent experimental works investigated the spin reorientation and room temperature magnetic anisotropy of $MnBi$. Yang also reported that the magnetic moment of Mn gradually deviated away from the c-axis when cooled below 200K, and further flipped into $a-b$ plane at low 50K. The origin of the low temperature magnetic anisotropy of $MnBi$ is unresolved, with several papers commenting that spin-orbit interactions may play a role in the anisotropy at low temperatures.

An interesting physical property of $MnBi$ is the positive thermal coefficient of coercivity, suggesting considerable potential of $MnBi$ as a permanent magnet material in vehicle and power applications. $MnBi$ LTP has a positive temperature coefficient, a coercivity $\mu_o H_c$ of 12.0T at room temperature, and a high coercivity, even larger than $NdFeB$ at elevated temperatures. Yang suggested that the room temperature magnetic anisotropy of $MnBi$ is the dominant factor leading to the positive temperature coefficient of coercivity and magnetization. It is assumed that the change of easy direction of $MnBi$ from the $a-b$ plane at 0K to uniaxial anisotropy above 200K leads to the increase of coercivity and total magnetization. However, Davenport [120] has reported that the spin-orbit splitting is less than expected. In his recent work, $MnBi$ compounds in the $zincblende-type$ structure and tetragonal phase are both reported to be half-metallic ferromagnetic, and the property of half-metallic ferromagnetism is maintained over a larger volume range for the tetragonal structure than for the cubic structure.

The aim of the present study is to investigate the origin of unique thermomagnetic behavior in $MnBi$ materials through first principles computation and comparisons with the related material, $MnSb$. $MnSb$ has a similar crystallography and electronic structure to $MnBi$ but loses magnetic power at elevated temperatures. To understand potential structural roles in thermomagnetic properties, three crystal structures common to the family MnX (X = Group V element) were investigated for both compounds, the room temperature stable $NiAs$-type structure ($B8_1$), an elevated temperature MnP-type structure ($B31$) noted for $MnSb$, and a $zincblende-type$ structure ($B3$). All three structures have been observed in $MnAs$ by earlier investigator [35]. Temperature effects on the electronic structure and properties were examined by cold smearing scheme and Fermi-Dirac population method. Thermal expansion effects on the $MnBi$ unit cell have also been taken into consideration using the experimental nonlinear thermal expansion coefficient.

2.2 Theoretical Backgrounds

2.2.1 Rare-earth replacement magnetic materials

There is currently an interest in searching for permanent magnet materials for electric motor applications that are alternatives to those in wide use, which possess expensive Rare Earth (RE) elements such as Nb and Sm [13]. As various materials are explored for their potential applicability in this regard, important figures-of-merit include the energy product related to the area enclosed by the magnetic hysteresis loop and the Curie temperature, T_c [81]. Only a material with a sizable energy product can perform useful work on its surroundings, and the temperature at which this work is performed must be comfortably below the temperature at which its total magnetic moment disappears. While T_c is largely a function of the size of the near-neighbor exchange energies, the energy product, which is closely related to the coercivity, is a multi-scale property, which reflects the tendency of magnetic domains to resist reorientation when placed in an external field, which is misaligned with them. This complex physics of domain wall structure, motion, and pinning is all dependent in part on a microscopic property: the magnetocrystalline anisotropy energy (MAE), the energy required to reorient the electron spins in a ferromagnet from easy-to hard-axis directions [81, 48]. Though the energy product involves much more than the MAE, it is hard to imagine a material with a sizable energy product that does not also have a significant uniaxial MAE. Indeed, permanent magnets in wide industrial use, such as Sm_2Co_{17} and $Nd_2Fe_{14}B$, possess fairly large MAEs [94] resulting from the interplay between the large spin-orbit interaction provided by the RE element together with the enhanced crystal field splitting in these tetragonal structures.

Rare Earth compounds are not the only ones to exhibit large MAE, however. For instance, $CoPt$, $FePt$ [94], and the recently-studied Li_2FeN_5 [5] are just a few examples of materials with anisotropies which rival or even exceed those of the permanent magnets in wide use. In general, the problem of searching for new reduced-RE permanent magnet alternatives should benefit from ab initio electronic structure calculations, from which Tc and MAE can be predicted. And in this case, Rare Earth compounds themselves present a formidable challenge, owing to the fact that they often possess narrow-band f-electron levels in the neighborhood of their Fermi energies, which are notoriously difficult to treat predictively. Various additions to density functional theory (DFT) such as DFT+U have been applied to the prediction of MAE in RE

magnets [61, 99], but it is still unclear if such mean-field extensions are indeed suitably predictive for the purpose of designing new materials [8]. For $CoPt$ and other such non-Rare Earth materials, however, the situation is thought to be slightly better with respect to ab initio calculations.

In this work, we discuss density functional theory calculation of the thermo-magnetic properties of two possible candidates for rare-earth replacements, $MnBi$ and $(Fe_{1-x}Co_x)_2B$ with different approaches. As the extension of the current study, detailed analysis of the spin polarization and spin-orbit coupling would be needed to develop a quantitative clarification of the origin of positive thermo magnetic property of rare-earth replacements. I propose the future works to develop a dynamical understanding of the thermal effect in many-body ferromagnetic system combining Monte-Carlo, KKR-method, and Heisenberg model with first-principle DFT.

2.2.2 Density Functional Theory

The quantum mechanical wave function contains, in principle, all the information about a given system. For the case of a simple 2-dimensional square potential of single atomic system, we can solve the Schrodinger equation exactly in order to get the wave function of the system. From the solved wave function, then we can determine the allowed energy states of the system. However, when system size is increased as many-body system, it is impossible to solve the Schrodinger equation due to the complexity of the equation.

Density Functional Theory is the computational method in quantum physics to obtain an approximate solution to this numerically un-solvable Schrodinger equation of a many-body system. By several steps of approximation, the Schrodinger equation in ground state can be formulated as the function of functionals only depend on electron density.

In many-body system, if we assume the system is in stationary electronic state which the nuclei of the system are fixed by the Born Oppenheimer approximation, the electronic structure of system can be described by following many body Schrodinger equation.

$$
\begin{aligned}
H\Psi &= [T+V+U]\Psi \\
&= [\sum_{i=1}^{N}(-\frac{\hbar^2}{2m_i}) + \sum_{i=1}^{N} V(r_i) + \sum_{i=1}^{N} U(r_i, r_j)]\Psi \\
&= E\Psi \\
\Psi &\approx \Psi(r_1, r_2, ..., r_N)
\end{aligned}
\tag{2.1}
$$

where, for the N-electron system, H is the Hamiltonian, E is the total energy, T is the kinetic energy, V is the potential energy from the external field due to positively charged nuclei, and U is the electron-electron interaction energy. The operators T and U are called universal operators as they are the same for any N -electron system, while V is system dependent. Compared with the simple single atom Schrodinger equation, this many body Schrodinger equation contains the electron-electron interaction term, U. Therefore, the many body Schrodinger equation principally cannot be expressed as the combination of single Schrodinger equations.

Density-functional theory is based on two important theorems known as Hohenberg Kohn theorem [44]. Here we briefly describe these two theorems by referring the first chapter of the book Electronic Structure: Basic Theory and Practical Methods authored by Richard Martin [70].

First theorem is that for any many-body system of interacting particles, the external potential $V_{ext}(r)$ is determined uniquely by the ground-state particle density $n_0(r)$. By solving many-body Schrodinger equation with this external potential only depend on the ground-state particle density, the many-body wavefunction can be determined for the ground state as well. Therefore, from this theorem, we can conclude that all properties of the system are completely determined given only the ground-state density $n_0(r)$.

Second theorem is that, we only need the functional $E[n]$ to determine the ground state energy and density. The functional, $E[n]$, can be considered as,

$$
E[n] = F[n] + \int V_{ext}(r) n(r) d^3r + E_{int} \tag{2.2}
$$

where E_{int} is the interaction energy of nuclei, and $F[n]$ is the universal functional of the density including all internal energies (kinetic, $T[n]$, and potential, $E_{int}[n]$) of the interacting electron system:

$$
F[n] = T[n] + E_{int}[n] \tag{2.3}
$$

The practicable method for DFT calculations has been developed by Kohn and Sham [44, 55]. By their method, universal functional 2.3 can be written as following,

$$F[n(r)] = T[n(r)] + \frac{1}{2}\int \frac{n(r)n(r')}{|r-r'|} d^3r d^3r' + E_{XC}[n(r)] \tag{2.4}$$

where $n(r)$ indicates a trial electron density for the non-interacting system, $T[n(r)]$ is the kinetic energy functional for the non-interacting electrons, the second term at the right side is the electrostatic Hartree energy, and $E_{XC}[n(r)]$ is the so-called exchange- correlation energy functional. Here, $F[n(r)]$ is purely related to the system of electrons, and it is independent of the external potential. By applying the Hohenberg-Kohn minimum principle, Kohn and Sham found the following system of equations, known as Kohn-Sham equations,

$$\begin{aligned} V_{KS}(r) &= V_{ext}(r) + \int \frac{n(r')}{|r-r'|} d^3r' + V_{XC}(r) \\ V_{XC}(r) &= \frac{\partial}{\partial n(r)} E_{XC}[n(r)] \\ (-\frac{\partial^2}{\partial r^2} + V_{KS}(r) - \varepsilon_i)\varphi_i(r) &= 0 \\ n(r) &= \sum_{i=1}^{N} |\Psi_i(r)|^2 \end{aligned} \tag{2.5}$$

The Kohn-Sham equations have to be solved self-consistently because it is non-linear equations. Starting from an initial guess, which is usually obtained by a summation over atomic densities, the Kohn-Sham potential V_{KS} and consequently the Hamiltonian are obtained using Eqs. 2.5. Then, diagonalization of this Hamiltonian, Kohn-Sham energies ε_i and Kohn-Sham states φ_i are found, resulting in a new density. This new density, in turn, determines a new Kohn-Sham potential. This cycle is repeated until a converged ground-state density is obtained. Once the ground-state density is obtained, the ground-state energy of the electronic system is found as,

$$E = \sum_{i=1}^{N} \varepsilon_i + E_{XC}[n(r)] - T[n(r)] + \int V_{XC}(r) n(r) d^3r - \frac{1}{2}\int \frac{n(r)n(r')}{|r-r'|} d^3r d^3r' \tag{2.6}$$

All many-body effects can be taken into account in the calculation of the ground state if the exact form of $E_{XC}[n(r)]$ is known. Thus, good approximations of this exchange potential, $E_{XC}[n(r)]$, is very important. This exchange potential, $E_{XC}[n(r)]$, contains all the many-body effects, and has to be approximated for practical applications. Widely used important approximations are the Local Density Approximation (LDA)

and the generalized gradient approximations (GGAs). LDA assumed that, locally, the quantum system under study can be approximated by a homogeneous electron gas. Although this might not seem appropriate for atoms and molecules, the LDA has been remarkably successful. In GGA, instead of taking only the electron density into account, as in the LDA, the gradient of the density is also considered to account for the non-homogeneity of the true electron density. This has led to important improvements in accuracy with respect to the LDA. Because the LDA assumes that the density is the same everywhere, it has a tendency to over-estimate the exchange-correlation energy. GGA corrects for this tendency by considering non-homogeneity of density. With GGA, It is known that accurate results for binding energies, molecular geometries, and vibrational frequencies can be obtained.

2.3 Computational Methods

Density functional theory calculations have been performed for $MnBi$ and $MnSb$ within the local density approximation [56] and plane wave basis using the ABINIT package [29]. Single projector and norm conserving Troullier-Martins pseudopotentials were applied for Mn, Bi and Sb [105], and kinetic energy cutoff of 27 Ha was used with a $10 \times 10 \times 10$ k-point Monkhorst-Pack mesh [77]. Convergence of the total energy was checked by increasing the number of k-points and cutoff energy. The initial geometries for the $MnBi$ and $MnSb$ compounds were taken from the ICSD crystal structure database. The cell lattice and atomic position parameters were fully optimized using the BFGS minimizer with a force criteria of 10^{-6} [83]. The total magnetization and local magnetic moment in easy direction (c-axis) of these two compounds have been calculated as a function of temperature from 30K to 315K. In this preliminary study, however, the physical temperature of the system was approximated by electronic temperature with fixed smearing convergence. Metallic occupation of levels using different occupation schemes was controlled by the corresponding thermal broadening, using the Marzari-Vanderbilt cold smearing scheme [72]. The occupation broadening convolutes the density of states with a broadening δ function, defined as [27, 17, 107]:

$$\delta(x) = \frac{2}{\sqrt{\pi}} e^{-[x-\frac{1}{\sqrt{2}}]^2} (2 - \sqrt{2}x), \quad x = \frac{\mu - \epsilon}{\sigma}$$

The physical temperature of the system is approximated from the independent broadening δ function. The broadening factor x is a function of finite electronic temperature, Fermi energy μ and pseudo energy. The total magnetization of unit cell was calculated as a function of electronic temperature in a range from 30K to 315K with an interval of 30K. Thermal expansion of unit cell of $MnBi$ has been taken into consideration using the experimental isotropic thermal expansion coefficient.

2.4 Results

We have performed a series of first principle density functional theory calculations to compare the physical properties of $MnBi$ and $MnSb$. The total magnetization and local magnetic moment in easy direction (c-axis) of these two compounds have been calculated as a function of temperature in a range from 30K to 315K using the fixed smearing convergence in cold smearing electron occupation. Two kinds of structures, static and thermally expanded structures, of $MnBi$ and $MnSb$ have been used in thermomagnetic properties calculation by first principle DFT calculation. Experimental results of the linear thermal expansion coefficient were utilized for unit cell lattice thermal expansion in the latter case.

Three different types of structures, $NiAs$, MnP and *zincblende* were used in this study. Static structures for $MnBi$ and $MnSb$ were optimized using BFGS optimization scheme before computation of the total magnetization at specific electronic temperatures using cold smearing method. In the case of the thermally expanded structure, total magnetization at different temperatures was calculated by expanding the lattice constant of the compound according to the experimental data from neutron diffraction. The electronic structure of $MnBi$ has been compared with the related compounds, $MnSb$ and $MnAs$ [16]. In particular, $MnSb$ starts at low temperature with a similar band structure, structural phase and magnetic properties as $MnBi$. Experimentally, $MnSb$ has a transition temperature at 585K, a small deviation from that of $MnBi$, 633K. Coehoorn [12] discussed the similarities of the electronic structures in the low temperature phase between $MnSb$ and $MnBi$ by a self-consistent band structure calculation. Those results showed strong covalent $Mn-Bi$ interaction just as in $MnSb$. Without p(Sb or Bi)-d(Mn) hybridization, the width of the d-bands is mainly due to $d-d$ overlap of Mn along the c-axis which leads to the strong ferro-magnetism along c-direction. The $p-d$ hybridization induces a negative

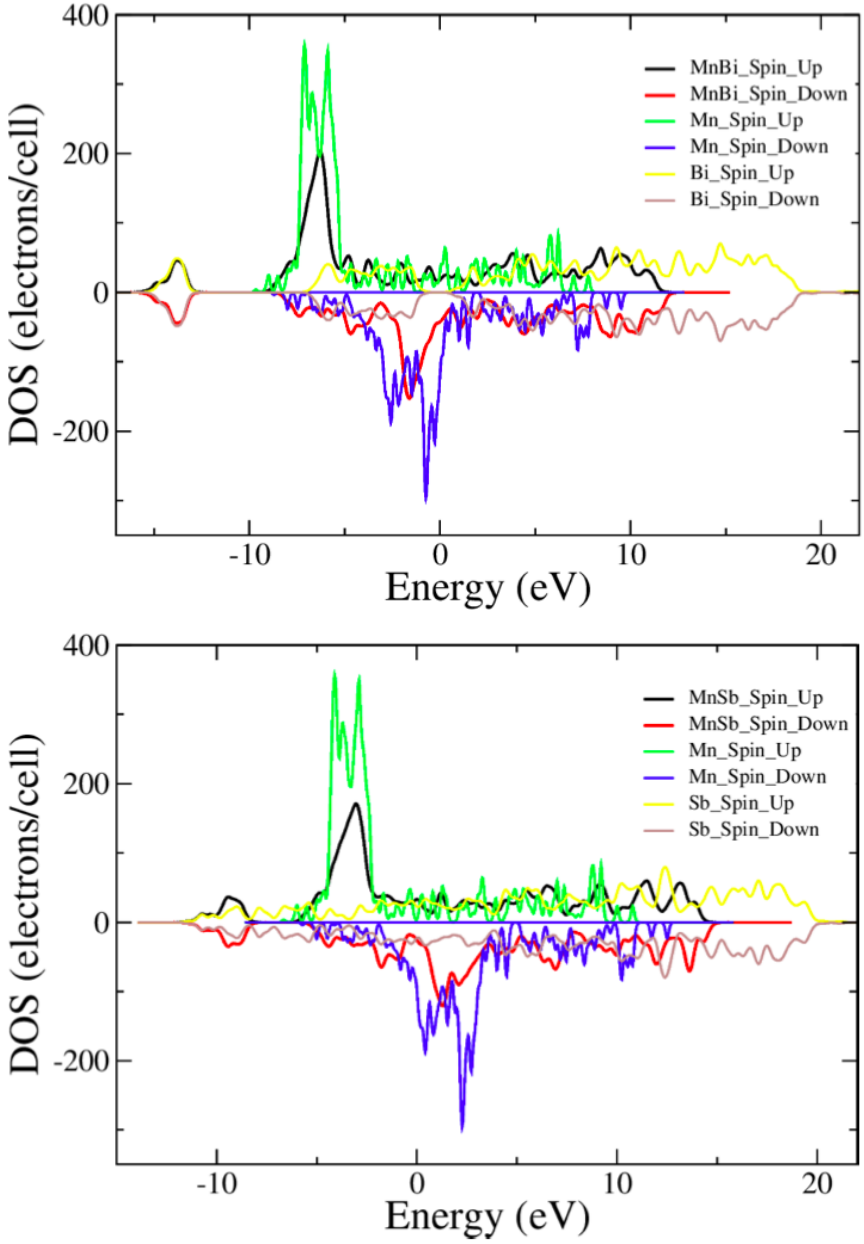

Figure 2.1: (Color online) Spin up and spin down density of states of Mn with relaxed hexagonal $NiAs$ structure. (a) Density of states of $MnBi$ compound and partial density of states of Mn and Bi atoms. (b) Density of states of $MnSb$ compound and partial density of states of Mn and Sb atoms. The DOS figures have been shifted by their relative Fermi levels, $MnBi(-1.82eV)$ and $MnSb(-1.56eV)$ respectively, to facilitate side-by-side comparisons.

Table 2.1: Total energy and energy differences (eV) for $MnBi$ and $MnSb$ in different structural forms in each unit cell (2 atoms per cell). Energy differences relative to the most stable form ($NiAs$) are given in parenthesis.

	NiAs	ZB	MnP
MnBi	-657.0726 (0.0)	-656.1521 (0.921)	-655.7885 (1.284)
MnSb	-655.6155 (0.0)	-655.4010 (0.215)	-654.9110 (0.705)

spin magnetic moment on the Bi and Sb sites but negligible compared with the positive magnetic moment of Mn. Figure 2.1 shows the densities of states of $MnBi$ and $MnSb$ from our first principle DFT calculation. The diagrams of density of states of both compounds are also very similar, but d-bands in $MnBi$ are narrower than $MnSb$ because of the larger $Mn - Mn$ distance in $MnBi$. This leads to larger spin contributions to the local magnetic moments on Mn atom: $3.87\mu B$ for $MnBi$ and $3.32\mu B$ for $MnSb$, with two atoms per unit cell. It is in agreement with the reported values of $3.61\mu B$ for $MnBi$ and $3.30\mu B$ for $MnSb$ measured by Coehoorn [12].

2.4.1 Predicted crystal structure parameters for MnBi and related compounds

Thermomagnetic properties of $MnBi$ and $MnSb$ have been calculated in the force optimized $NiAs$, MnP and $zincblende - type$ structures using force convergence criteria of 5×10^{-6}. Upon convergence, the energy differences between experimental and relaxed structure (Table 2.1) indicate that the $NiAs$-type structure is favored for both $MnBi$ and $MnSb$ relative to both the distorted $zincblende$ and $MnP - type$ forms. Experimental crystal structures are found in the ICSD crystal structure database for the $NiAs$ and MnP forms of $MnBi$ and $MnAs$, and the $NiAs$ form of $MnSb$. The $zincblende$ form of $MnBi$ has been investigated by Zheng [121, 120] who found that there was a mechanical instability in the idealized structure, which could be stabilized by local distortion along the c-axis.

The $NiAs$-type lattice structure is a hexagonal phase (space group P63/mmc, no. 194) with two atoms in the primitive unit cell. It is the equilibrium lattice structure (low temperature phase) of MnX family below the transition temperature. The crystallographic arrangement is shown in Figure 2.2. Experimentally, bulk $MnBi$ has lattice constants of $a = 4.341$Å, $c = 5.973$Å, with a c/a ratio of 1.376; and $MnSb$

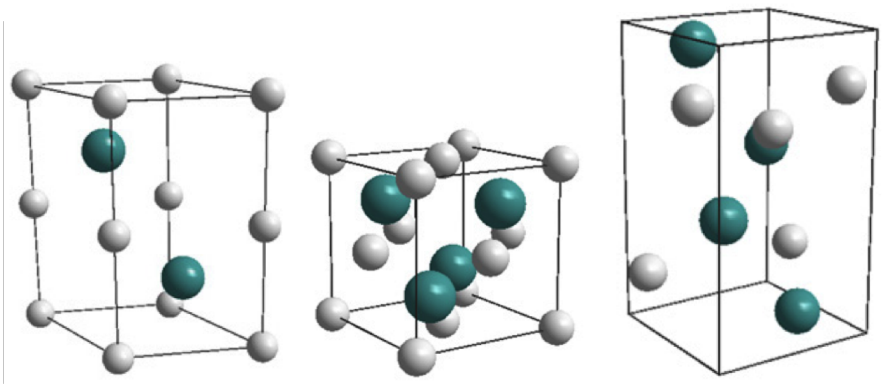

Figure 2.2: (Color online) Unit cell structure of $MnBi$: (a) hexagonal phase $NiAs$-type [experimentally observed], (b) orthorhombic phase MnP-type and (c) cubic phase $Zincblende-type$.

has lattice constant of $a = 4.15$Å, $c = 5.78$Å, and a c/a ratio of 1.393 [100, 118]. The calculated structural parameters ($a = 4.287$ Å, $c = 6.008$ Å, $c/a = 1.401$ Å) show good agreement with experimentally measured parameters, with the largest difference along c-axis $\Delta c = 0.228$, only 4% deviated from the experimental value.

The MnP-type lattice structure is an orthorhombic phase (space group $Pnma$) with two atoms in the primitive unit cell. It is reported that $MnAs$, $CrAs$, and $CoAs$ have phase transitions from $NiAs$-type to the MnP-type at $T_t = 398$K, 800K and 1200K, respectively [100]. Accompanying the crystal structure change, these pnictide compounds also exhibit a first-order ferromagnetic to paramagnetic transition when heated over T_t [51], with distortions of the upper and lower As layers, moving up and down respectively, to converge into MnP-type structure [78]. Although the transformation from $NiAs$-type to MnP-type has not been observed yet for the compounds with transition metal elements Sb and Bi, we still investigated the thermomagnetic properties of MnP-type in this preliminary study. Figure 2.2(c) shows the unit cell of cubic $MnBi$ with a $zincblende-type$ lattice structure (space group F43 m). Energetically, the MnP structure is less stable than the $zincblende-type$ structure for $MnSb$, and more so for $MnBi$, as reflected in Table 2.1. Calculations by Zheng [120] have shown that the cubic $zincblende$ structure of $MnBi$ and $MnSb$ is mechanically unstable. Tetragonal distortions of this structure stabilize this compound and introduce half-metallic ferromagnetic behavior, making them potential useful spintronic materials. We have used this form in our $zincblende$ computations.

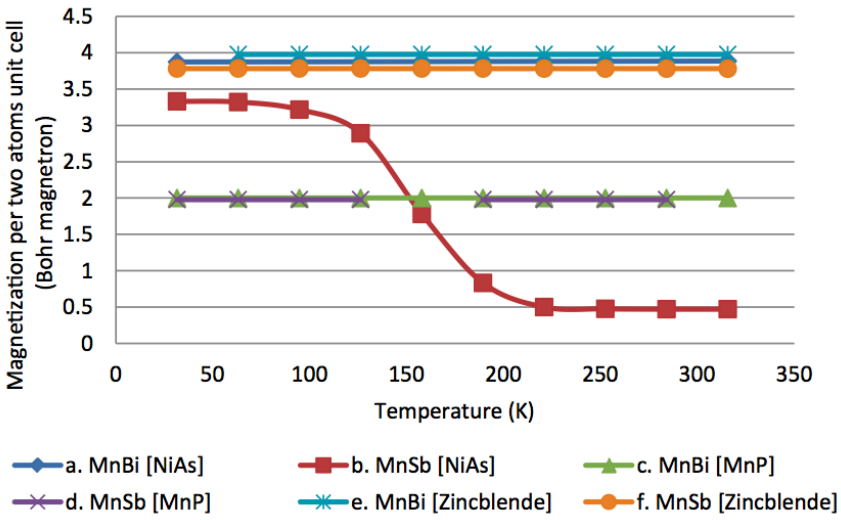

Figure 2.3: (Color online) Temperature dependent total magnetization per two atoms unit cell of $MnBi$ and $MnSb$ compound as a function of structural phase: (a) $MnBi-NiAs$ type (hexagonal), (b) $MnSb-NiAs$ type (hexagonal), (c) $MnBi-MnP$ type (orthorhombic), (d) $MnSb-MnP$ type (orthorhombic), (e) $MnBi-Zincblende$ type (tetragonal) and (f) $MnSb-Zincblende$ type (tetragonal). The $NiAs$ phase is a naturally occurring form at room temperature ambient conditions.

2.4.2 Thermomagnetic properties of MnBi and MnSb

The total magnetization and local magnetic moment in the easy direction (c-axis) of these two compounds have been calculated as a function of electronic temperature from 30K to 315K (Figure 2.3). For the hexagonal $NiAs$-type structure, the thermomagnetic curves were notably different between $MnBi$ and $MnSb$ (Figs. 2.3(a) and 2.3(b)), in agreement with experimental results. Although the increase of total magnetization of $MnBi$ is very small over the investigated temperature range compared to the experimental results showing a larger positive thermomagnetic coefficient, there is a clear difference between the thermomagnetic behavior of $MnBi$ and $MnSb$ compound [66]. The total magnetization of $MnSb$ decreases with a negative concave-shaped with first derivative function. Compared to $MnBi$, total magnetizations of $MnSb$ in MnP-type and $zincblende-type$ structure show only slight decreases with varying temperature. The total magnetization of $MnSb$ is slightly lower than $MnBi$, roughly proportional to the relative decrease in the $Mn-Mn$ distances in these compounds. The magnetization of the MnP structure is markedly lower, beyond the range of scaled density differences among these structures.

In Table 2.2, the differences in the magnetizations for $MnBi$ and $MnSb$ in the different structural forms at room temperature (300K) are given. Combining these results, the computational model points to a structure-dependent role for the experimentally observed positive thermomagnetic coefficient of $MnBi$. There are several possibilities to account for the positive thermomagnetic character of $MnBi$ compared with $MnSb$ in $NiAs$-phase. First, the temperature dependence of the $Mn-Mn$ distance may be greater in $MnBi$ than in $MnSb$. This would result in the d-bands being somewhat getting narrower in $MnBi$ than in $MnSb$, and lead to higher magnetization due to larger spin contributions to the local magnetic moment on the Mn atom. Second, a low temperature magnetic anisotropy mainly driven by the spin-orbit interaction may play a role. The magnetic anisotropy of $MnBi$ and $MnSb$ shows some similarities. At high temperatures the c-axis is the easy direction of magnetization and the magnetic moment flip into $a-b$ plane at critical temperature. However, previous analysis of density of states with and without spin-orbit coupling [12] suggests that the spin-orbit coupling does not play a dominant role in total magnetization change. The third possibility would be a result of different fractional occupations for $MnBi$ and $MnSb$ with increasing temperatures. The thermal variations of major and minor electronic contribution (occupation number) in the two compounds might be opposite or at different degrees. Decreasing $Mn3d$ DOS and the increasing $p(Bi/Sb)-d(Mn)$ hybridizations would contribute to the loss of total magnetization in the $MnSb$ compound.

In the second approach a thermally expanded cell has been investigated. Thermal expansion coefficients were determined from experimental lattice constants over a temperature range before and after the Curie temperature using X-ray and neutron diffraction. According to Willis and Roberts [112, 90], the a and c lattice constants for $MnBi$ increase almost linearly until 613K.

At 613K, a discontinuous structural transformation occurs, and the c-axis contracts 3% and the a-axis expands 1%. It has been suggested that this change was caused by material decomposition, not a Curie point phenomenon. Starting from the optimized hexagonal $NiAs$-type geometry of $MnBi$, cell lattice parameters are expanded corresponding to this experimental data. The total magnetization (Figure 2.4) shows a linear increase following the cell expansion. The sharp drop occurring at 613K reflects the structural changes due to the transformation reported in the Willis results. After this transition temperature, 613K, the dramatic drop of total magnetization is shown

Table 2.2: Comparison of the room temperature magnetizations (μB) of $MnBi$ and $MnSb$ for the $NiAs$, MnP, and $Zincblende$ structure forms for unit cell (two atoms per cell).

	NiAs	ZB	MnP
MnBi	3.885	2.000	3.976
MnSb	0.471	1.980	3.781

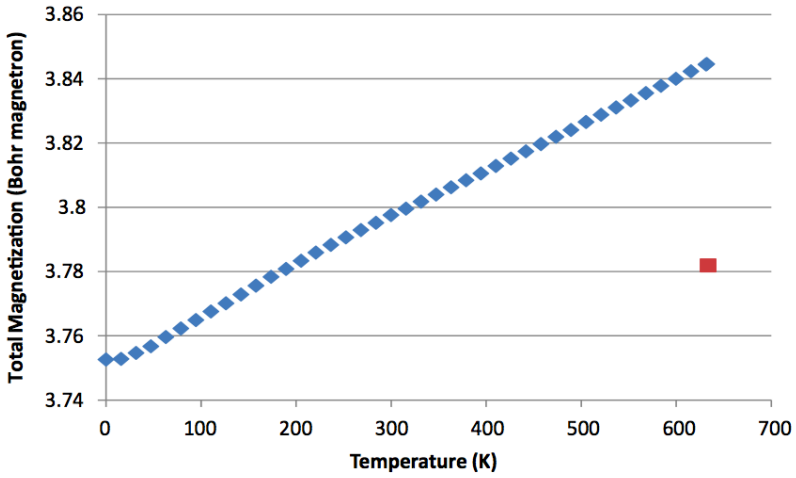

Figure 2.4: (Color online) Temperature dependence of the $MnBi$ total magnetization in the $NiAs$ structural form including thermal expansion of the unit cell when lattice expansion considered. The "isolated" data point is the magnetization value for a transformed cell occurring at 633K. Values are two atoms per cell unit.

in good agreement with experimental results from Willis and Roberts.

2.5 Discussions

The change in the total magnetization of $MnBi$ over the temperature range up to 300K for the static structure, however, was less than $0.05\mu B$ (Figure 2.3); while for the expanding unit cell with temperature range up to 600K, the change is also small, less than $0.1\mu B$ (Figure 2.4). These observations point toward two possibilities. First, the broadening of electronic occupation numbers by the smearing method is too small since the lattice temperature remained in a static ground state in our calculation. To address the temperature dependent phonon effects, alternative computational methodologies, such as ab initio molecular dynamics or warm DFT [93]

could be explored. Warm-DFT is the Kohn-Sham realization of thermal density functional theory to generate a potential surface for ionic motion using approximate ground-state exchange correlation functionals with the temperature dependence of the exchange correlation free energy picked up implicitly from the temperature dependence of the density. According to these authors, it was their estimation that the effects of warm-DFT for the temperature range. below 1000K would be minimal. Second, spin reorientation effect in $MnBi$ observed in the 90K – 150K temperature range could be existed. Scalar relativistic pseudo potentials do not take into account spin-orbit coupling effects, although previous investigation has estimated these to be small [120, 10]. Despite the fact that the fixed smearing convergence in cold smearing method of our current work is coarse, it still is one of the few ways to simulate thermal excitation specially in low temperature range. Beyond the trend analysis of this current work, a detailed analysis of the spin polarization and spin-orbit coupling would be needed to develop a quantitative clarification of the origin of positive thermo magnetic property of $MnBi$. Our future works will focus on developing a dynamical understanding of the thermal effect, and further comparisons with structurally similar magnetic compounds.

To sum up, we have investigated the thermomagnetic properties of $MnBi$ and $MnSb$ as a function of electronic temperature for the $NiAs$, MnP and *zincblende* structures. The first principles calculation has shown good agreement with experimental structural and thermomagnetic results for $MnBi$ and $MnSb$. Comparing results from the $NiAs$, MnP and $zincblende - type$ structures, our results clearly show a structural role in the thermomagnetic behavior of these compounds, with marked temperature sensitivity for $MnBi$ in its room temperature $NiAs$-type structure. $MnSb$ shows little temperature dependence. The magnetization of $MnSb$ and $MnBi$ in the MnP structure is markedly lower than the distorted *Zincblende* values. Using thermal expansion effects derived from experimental measurement, total magnetization of $MnBi$ shows a small increase with larger cell volumes.

Chapter III

COMPUTATIONAL STUDY OF RARE-EARTH SUBSTITUTES $(FE_{1-X}CO_X)_2B$. USING HEISENBERG MONTE CARLO MODELING

3.1 Motivation

Recently, a team searching for Rare earth-free permanent magnets suggested the compound $(Fe_{1-x}Co_x)_2B$ for $x \approx 0.3$ as a potential candidate [59]. They showed experimentally that both the coercivity and the MAE peak for the specific value $x \approx 0.3$, in agreement with earlier measurements from several decades before by Iga [45] and Takacs et al. [101]. Though the value of the MAE for this family of materials is well below that of some other candidates (such as $CoPt$, for instance), several features of the system are quite interesting from the perspectives of both applications and theory:

1. The T_C are reasonably high, and are known experimentally as a function of Co-concentration, x [101].

2. The Magnetic Anisotropic Energy(MAE) is known not only as a function of x, but also as a function of temperature, T, throughout the full range of x [45, 101]. (Figure 3.1)

3. The crystal structure is thought to be essentially unchanged, modulo small changes in lattice parameters, throughout the full range of (x, T) [45].

4. The electronic structure is devoid of partially occupied f-electron states.

Point 4 notes well for the application of the first principles electronic structure calculations of the DFT variety, while point 3 suggests that additional complications arising from structural complexity may not play a large role. Point 2 ensures that there is a wealth of data to which to compare, challenging the theoretical community to predict both the detailed concentration- and temperature-dependence of the MAE,

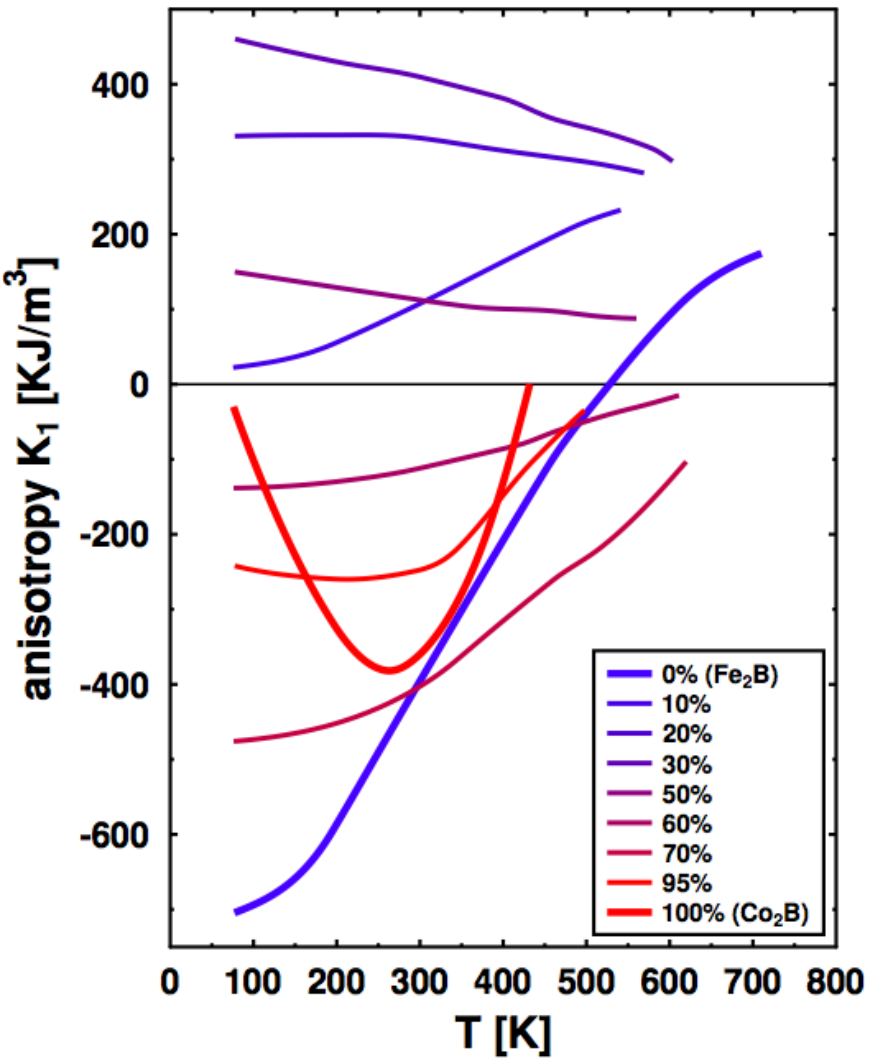

Figure 3.1: Temperature dependent magnetic anisotropy constant K of $(Fe_{1-x}Co_x)_2B$ system (Source: Atsushi Iga et.al, Magnetocrystallin anisotropy in $(Fe_{1-x}Co_x)_2B$ system [45])

thereby providing a very useful testing ground for current and developing strategies to predict this important quantity.

In this work, we perform the hybrid computational modeling combining KKR-CPA calculation, ab initio electronic structure calculations, and Monte-Carlo simulation to predict T_C as a function of Co-concentration for $(Fe_{1-x}Co_x)_2B$.

3.2 Theoretical backgrounds

3.2.1 Theory of magneto-crystalline anisotropy

Magnetic anisotropy is the directional dependence of a material's magnetic properties. The magnetic moment of magnetically anisotropic materials will tend to align with an 'easy axis', which is an energetically favorable direction of spontaneous magnetization. The two opposite directions along an easy axis are usually equivalent, and the actual direction of magnetization can be along either of them. Magnetic anisotropy strongly affects the shape of hysteresis loops and controls the coercivity and remanence. Anisotropy is also of considerable practical importance because it is exploited in the design of most magnetic materials of commercial importance.

There are several different types of anisotropy depends on (1) crystal structure (Magnetocrystalline anisotropy), (2) grain shape (Shape anisotropy), (3) applied or residual stresses (Stress anisotropy). Here, I focus on microscopic magnetocrystalline anisotropy arising from the spin-orbit coupling.

3.2.1.1 Magneto-crystalline anisotropy

Magneto-crystalline anisotropy is an intrinsic property of a ferri- and ferro- magnet, independent of grain size and shape. It can be most easily understood by measuring magnetization curves along different crystal directions. Depending on the crystallographic orientation of the sample in the magnetic field, the magnetization reaches saturation in different fields. The direction where the magnetization reaches saturation in lowest magnetic field called easy direction which represents the direction where the spin tends to be easily aligned with that direction. The direction where the magnetization reaches saturation in largest magnetic field called hard direction which represents the last direction where spin would like to be aligned. Magneto-crystalline anisotropy energy (MAE) is the energy necessary to deflect the magnetic moment in a single crystal from the easy to the hard direction. Thus, the lager MAE, the harder to flip the magnetic moment from the easy to the hard direction, which means the material has strong tendency to aligned to easy-direction, so the strong magnet. To sustain strong magnetism as the permanent magnet application, rare-earth replacement candidate materials should have reasonably high Magneto-crystalline anisotropy energy. The easy and hard directions arise from the interaction of the spin magnetic

moment with the crystal lattice (spin-orbit coupling).

3.2.1.2 The Magnetic Spin-Orbit Coupling

Spin-orbit interaction is a phenomenon that manifests itself in lifting the degeneracy of one-electron energy levels in atoms, molecules, and solids. The non-relativistic Schrodinger equation is frequently used as a first approximation, e.g. in electron band-structure calculations. Without relativistic corrections, it leads to doubly-degenerated bands, spin-up and spin- down, which can be split by a spin-dependent term in the Hamiltonian. In this approach, spin-orbit interaction can be included as a relativistic correction to the Schrodinger equation.

By taking the non-relativistic limit of the Dirac equation, one arrives at the Pauli equation. By including the next order in v/c, one obtains additional terms. In this case one obtains the Hamiltonian, in spinor space,

$$H = \frac{p^2}{2m_e} + V(r) - \frac{p^4}{8(m_e)^3c^2} + \frac{\hbar}{2m_e^2c^2}\frac{1}{r}\frac{dV}{dr}s\cdot l + \frac{\hbar^2}{8me^2c^2}\nabla^2 V$$

First two term is H_o, non-relativistic hamiltonian. Third term is the correction to kinetic energy. Fourth term is the spin-orbit coupling energy. Fifth term is the correction to potential term. The last term is also called the 'Darwin term'. The spin-orbit coupling is the only term relevant for us now.

$$H_{so} = \frac{\hbar}{2m_e^2c^2}\frac{1}{r}\frac{dV}{dr}s\cdot l$$

For the Coulomb potential of the nucleus,

$$H_{so} = \frac{\hbar}{2m_e^2c^2}\frac{Ze^2}{4\pi\varepsilon_o}\frac{1}{r}\frac{d}{dr}s\cdot l = \frac{\hbar}{2m_e^2c^2}\frac{Ze^2}{4\pi\varepsilon_o}\frac{s\cdot l}{r^3} = \frac{\mu_0}{4\pi}g{\mu_B}^2Z\frac{s\cdot l}{r^3}$$

We assume g=2. For several electrons in an incompletely filled shell, the operator of spin-orbit coupling is

$$H_{so} = \frac{\mu_0}{4\pi}g{\mu_B}^2Z\sum_i\frac{s_i\cdot l_i}{r_i^3}$$

In principle, we should include not only the nuclear potential but the full effective potential of the Hartree approximation. In practice, this is expressed by replacing the atomic number Z by an effective one, Z_{eff} which is smaller than Z. We now evaluate the contribution of spin-orbit coupling to the energy, treating H_{so} as a weak perturbation to H_o. Then

$$E_{so} = \langle H_{so}\rangle = \frac{\mu_0}{4\pi}g{\mu_B}^2Z_{eff}\sum_i\left\langle\frac{s_i\cdot l_i}{r_i^3}\right\rangle$$

Because for free ions, the radial wave function $R_{nl}(r)$ is the same for all orbitals comprising a shell. Thus

$$E_{so} = \frac{\mu_0}{4\pi} g{\mu_B}^2 Z_{eff} \left\langle \frac{1}{r^3} \right\rangle_{nl} \sum_i \langle s_i \cdot l_i \rangle$$

We now call the electrons with spin parallel to S "spin up" and the others "spin down". Furthermore, s_i and l_i commute. We can thus replace, in the expectation value, s_i by $S/2S$ for spin up and by $-S/2S$ for spin down, respectively. The s_i has magnitude $1/2$. Thus,

$$E_{so} = \frac{\mu_0}{4\pi} g{\mu_B}^2 Z_{eff} \left\langle \frac{1}{r^3} \right\rangle_{nl} \left(\sum_{i=\text{spin up}} \frac{\langle s_i \cdot l_i \rangle}{2S} - \sum_{i=\text{spin down}} \frac{\langle s_i \cdot l_i \rangle}{2S} \right)$$

We have found that the spin-orbit Hamiltonian can be expressed as,

$$H_{so} = \xi(r) L \cdot S$$

As the magnetism of transition metals is due to the d electrons, it is sufficient to consider only the spin-orbit interaction for d electrons. Thus, the spin-orbit coupling finally writes,

$$H_{so} = \xi L \cdot S$$

in the Hamiltonian, where $\xi > 0$ ($\xi < 0$) for less (more) then half filled shells. The ξ, the spinorbit constant, is the radial average of $\xi(r)$ over d-orbitals. In transition metal, ξ increases considerably with increasing atomic number Z, as shown in equations above. We have found that the spinorbit coupling in a free atom or ion also behaves, within perturbation theory, like a term

$$H_{so} = \xi L \cdot S$$

In a free atom or ion, the Hamiltonian is spherically symmetric, and the total orbital moment L a good quantum number; thus, the ground state has a non-zero orbital moment. This is essentially the case for rare-earth $4f$ ions.

3.2.2 KKR-CPA calculation

In Chapter 2, the brief description of Density functional theory has been presented. DFT summarized with Hohenberg-Kohn theorem and Kohn-Sham equation. The Kohn-Sham formalism reduces the problem of minimizing the energy functional to the

problem of solving a set of single-electron Schrodinger equations. Many approaches have been developed in order to solve these single-electron equations, differing mainly in the choice of the basis set for the single-particle orbitals. As a consequence of this choice of basis set, It has been represented difference in performance. In solid state calculations, two basic classes of methods are used: Hamiltonian methods, based on the diagonalization of the Hamiltonian and Green's function techniques relying on the multiple-scattering formalism. Ab initio Korringa Kohn Rostoker coherent-potential-approximation (KKR-CPA) method is the method to solve single-electron Schrodinger equation by Green's function technique with multiple scattering theory. It effectively characterize the effects of chemical disorder on the electronic and magnetic properties.

The KKR method have been introduced in 1947 by Korringa [15] and extended in 1954 by Kohn and Rostoker [57]. The KKR-CPA method, implemented within density functional theory, provides an ab initio theoretical description of the effects of disorder on the underlying electronic structure. An important aspect of the KKR-CPA is that it is specifically formulated to calculate the configurationally averaged electronic structure, including local and total densities of states (DOS) and magnetic moments within a single-site (or mean-field) theory. [21]

As mentioned above, the main characteristic feature of this method is the use of the multiple scattering theory(MST) for solving the Schrodinger equation. In this way the problem is broken up into two parts which is potential related part and geometry related part. In first potential related part, one solves the single site scattering problem by a single potential in free space. In second geometry related part, one solves the multiple scattering problem. The multiple scattering problem by solved in a way that the incident wave to each potential should be the sum of the outgoing waves from all other scattering centers. In this way, the resulting equations show a separation between potential and geometry properties being characteristic for the KKR method.

Another important strength of the KKR method is that, in the KKR method one solves the radial Schrodinger equation for each site exactly using multiple scattering theory. Therefore, it does not rely on a finite basis set for the expansion of the wave functions as practically all other methods of electronic structure calculations do. This is the great strength of multiple scattering theory can be much better exploited than in the wave function scheme without worrying about proper choice of basis set.

There are many application for KKR-CPA method. In particular, due to the use of

the complex energy integration of typical diagonalization methods it is well suited for ground-state calculations with the computational efficiency. The application of KKR-CPA method includes solids with reduced symmetry, as, for example an impurity in an otherwise ordered host crystal, or surfaces, layered systems, etc. Another important application is the investigation of randomly disordered alloy.

In this chapter, in order to obtain coupling coefficients in Heisenberg Hamiltonian for $(Fe_{1-x}Co_x)_2B$ families, we used spin-polarized KKR-CPA method relies on simplifying the many-body Schrodinger equation to a number of single particle Kohn-Sham equations.

Here, I will briefly sketch the basic idea of the KKR Green's function method with two way (1) by matching technique and (2) by multiple scattering theory [20].

Firstly, KKR-GF can be conceptually interpreted by the matching technique. The KKR method start from a decomposition of total system into atomic region. Such atomic region representing a system, such as molecule, atomic cluster, solid, etc, is treated as an isolated system embedded in a free-electron environment. Then, for a given potential, the single site radial Schrodinger problem is solved in a non-relativistic way to obtain the angular momentum l and energy dependent radial wave function $R_l(r, E)$. Note that the single site in radial Schrodinger problem is representing our system rather than real single atom. In s next step, the solution inside atomic regions are matched together coherently with each other assuming free-electron like behavior. Matching can be done only for certain energies corresponding to the energy eigenvalues of the system.

Secondly, KKR-GF can more numerically interpreted in terms of multiple scattering theory. The potential connected with an atomic region gives rise to scattering of an incoming electron wave into an outgoing wave as shown in Figure 3.2. This scattering event can be represented by a phase shift $\delta(r - r')$ of the partial wave function $R_l(r, E)$. The way that radial wave function shifts its phase is represented as a corresponding single site scattering t-matrix t_i. The free energy like wave propagation between scattering centers is described by the free electron Green function, $G^0(r, r', E)$. Now, the matching condition referred above corresponded to the requirement that the wave function coming in and at an atomic site is same with the superposition of the waves outgoing from all other sites. This event can be directly interpreted by in-homogeneous Schrodinger equation with single electron Green function $G(r, r', E)$

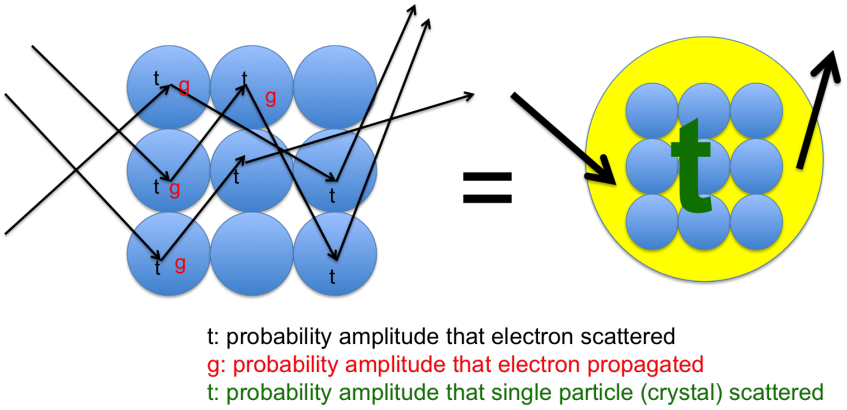

Figure 3.2: t-matrix describes scattering due to each potential. Multiple scattering is successive scattering due to many potentials. The total scattering amplitude is the sum of the amplitudes of those processes.

as following,

$$(E - H)G(r, r', E) = \delta(r - r') \tag{3.1}$$

where H is the Hamiltonian of the system. With a free electron green function, $G^0(r, r', E)$, the single-site green function can be introduced via a Dyson equation.

$$G(r, r', E) = G^0(r, r', E) + G^0(r, r', E)t_n G^0(r, r', E) \tag{3.2}$$

Here, t_n is the single-site t-matrix. In KKR-CPA, the full green function is then evaluated through a multiple-scattering formalism so that,

$$G(r, r', E) = G^0(r, r', E) + G^0(r, r', E)TG^0(r, r', E) \tag{3.3}$$

where

$$T = \sum_{n',n} \tau_{n,n'} \tag{3.4}$$

$\tau_{n,n'}$is the scattering path operator which brings an incoming electron at site n to an outgoing at site n'. For a crystal these may be evaluated via Lloyd's formula. [119] The method outlined above allows for evaluation of the energy dispersion relation $E(k)$.

3.2.3 Obtaining Coupling Coefficient J_{ij} from KKR-CPA calculation

The exchange coupling parameter J_{ij} in Heisenberg Hamiltonian can be found from ab initio based KKR Green's function method using the formulation of Lichtenstein

et al [65].

$$J_{ij} = \frac{1}{4pi} \int_{E_F} \mathbf{Trace}(t^{-1}_{i(up)} - t^{-1}_{i(down)}) \tau^{ij}_{up} (t^{-1}_{i(up)} - {}^{-1}_{i(down)}) \tau^{ji}_{down} dE \tag{3.5}$$

The site i in these calculations is assumed to be positioned in the center of a cluster of radius $R_{clu} = max|R_i - R_j|$. The exchange coupling parameters are calculated with respect to the central site i of a cluster with the radius R_{clu}.

3.2.4 Monte-Carlo Method

Monte Carlo simulation is a very important class of stochastic methods for calculating thermal properties of many-particle systems. Arguably these are the most important numerical techniques in statistical physics. [60] Monte Carlo simulation methods are related to the elementary Monte Carlo integration methods, but are based on more efficient non-uniform sampling schemes which rely on repeated random sampling to obtain numerical results. Their essential idea is using randomness to solve problems that might be deterministic in principle. By using importance sampling, the configurations (particle positions, spin directions, etc.) of a finite but large many-body system (up to millions of degrees of freedom) can be generated according to the Boltzmann distribution, so that thermal expectation values are obtained as simple arithmetic averages of functions measured on the configurations.

As a simple illustration of the advantage of important sampling according to the Boltzmann probability, let's consider one dimensional integral for obtaining thermal expectation of observable - A. $P_{arb}(x)$ is an arbitrary probability distribution.

$$< A >= \int_{-L}^{L} P_{arb}(x) A(x) dx, \int_{-L}^{L} P_{arb}(x) dx = 1 \tag{3.6}$$

Now, let's consider we randomly sample M points $x_1, x_2, ..., x_M$ in the range [-L,L], then the expectation value is estimated as

$$< A > \approx \frac{2L}{M} \sum_{M}^{i=1} P_{arb}(x_i) A(x_i) \tag{3.7}$$

Now, let's consider that $P_{arb}(x)$ is sharply peaked in a small region, then the statistical fluctuation of this estimate will be determined by only a small fraction of the generated points which fall within the dominant region. Then, if we sample the points according

to some probability distribution $W(x)$, which is picking a point in an infinitesimal range $[x, x + dx]$, the estimate for the expectation value would be,

$$< A > \approx \frac{1}{M} \sum_{M}^{i=1} \frac{P_{arb}(x_i)}{W(x)} A(x_i) \tag{3.8}$$

This has less statistical fluctuations than the previous estimation of uniform sampling. In general, it is impossible to find the optimal $W(x)$ to minimize the fluctuation, but if $P_{arb}(x)$ has much variation than $A(x)$, a very good solution is to use $W(x) = P(x)$.

In statistical physics, the probability of electron occupation - P is a sharply peaked exponential function $e^{\frac{-E}{k_B T}}$ of the energy and the measured configuration - A is typically a linear or low-order polynomial function of the system degrees of freedom. The fluctuations in P are thus very large relative to those of A and the sampling using P as the probability distribution is then close to optimal. This is what is meant by the term importance sampling. Using importance sampling instead of uniform random sampling is crucial when a small fraction of the configuration space dominates the partition function, which is always the case with the Boltzmann probability in statistical mechanics models at temperatures of interest.

One of the primary utilities of Monte Carlo simulation is in studies of phase transitions and critical phenomena. This will be the focus of applications discussed here. Although there are analogous simulations methods available also for quantum systems (called quantum Monte Carlo methods), we will here consider only Monte Carlo simulations of classical many-body models to simulate thermal fluctuation of spins.

3.2.5 Heisenberg Model

The Heisenberg model is a statistical mechanical model used in the study of critical points and phase transitions of magnetic systems, in which the spins of the magnetic systems are treated quantum mechanically. In the prototypical Ising model, defined on a d-dimensional lattice, at each lattice site, a spin s_i which is either $+1$ or -1 represents a microscopic magnetic dipole to which the magnetic moment is either up or down. However, in Heisenberg model, we treat rotating spin with spherical direction rather then aligned with only up or down directions in Ising model. Heisenberg model is a more realistic model in that it treats the spins quantum-mechanically, by replacing the spin by a quantum operator (Pauli spin -1/2 matrices at spin 1/2), and the coupling constants J_x, J_y, and J_z in 3-dimensions. The leading exchange

interaction between spins in ionic crystals is usually of the form,

$$H = -\frac{1}{2}\sum_{i=ij} J_{ij}\vec{s}_i\vec{s}_j$$

where in the sum i and j run over all sites in 3-dimensions, $J_{ij} = J_{ji}$ is symmetric and the factor $1/2$ corrects for double counting. The set of spins of the unit length is represented as,

$$\vec{s}_i \in \mathbb{R}^3, |\vec{s}_i| = 1$$

each one placed on a lattice node. The coupling constant represents coupling between each spins,

$$J_{ij} = J \quad \text{if } i,j \text{ are neighbor, and} \quad 0 \text{ otherwise.}$$

3.3 Computational Methods

Fe_2B and Co_2B have the same crystal structures, space group 140, $I4/mcm$, also known as the $CuAl_2$ prototype or $C16$. The boron atoms occupy the 4a (0,0,1/4) positions, and the iron or copper atoms the 8h (ξ,1/2+ξ,0) sites. Experimental values for ξ are 0.1661 for Fe_2B and 0.1663 for Co_2B [45]. The crystal structure is shown in Figure 3.3. For intermediate concentrations, the crystal structure is assumed to be the same throughout the paper. This is compatible with the limited x-ray diffraction studies performed on this suite of materials for intermediate x [45], and the efficacy of this assumption will be further strengthened when our results for T_C are compared to those of experiment.

There are three steps we have obtained Currie temperature, T_C.

1. SPR-KKR calculation to obtain coupling constant, J_{ij} in Heisenberg model
2. Monte Carlo simulation of magnetic moment spins at finite temperature
3. Obtaining T_C from Monte Carlo simulation

For our calculations of T_C for various Co-concentrations, we repeated the steps as increasing Co-concentration from $x = 0$ to $x = 1$ with the interval of 0.05.

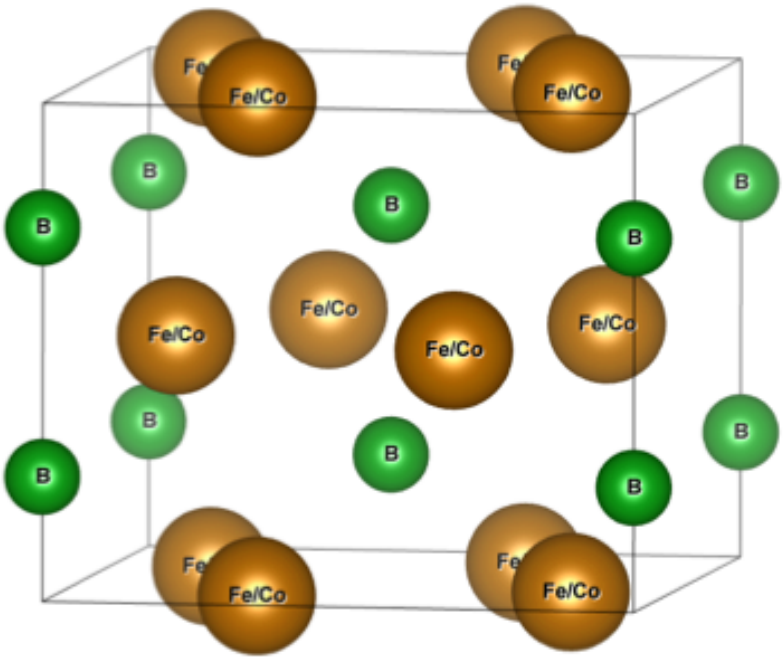

Figure 3.3: $(Fe/Co)_2B$ cell (Al_2Cu prototype (C16)), spacegroup 140, I4/mcm. B occupies the 4a (0,0,1/4) Wyckoff positions, Fe and Co the 8h (ξ,1/2+ξ,0) with ξ=0.1661(Fe_2B) and ξ=0.1663 (Co_2B).

3.3.1 KKR-CPA calculation

As the first step, we have used the Korringa-Kohn-Rostoker (KKR) [28, 29] DFT code, Hutsepot, within the coherent potential approximation (CPA) [96, 102, 113, 49, 50, 38, 37]. This allows us to obtain Heisenberg exchange energy (coupling constant) J_{ij}. [64]

All such KKR calculations, to obtain the effective J_{ij} parameters, are performed within the collinear spin density functional formalism (using PBE), in which no spin-orbit interaction is considered.

3.3.2 Monte Carlo simulation using *Full Spin MC*

From the calculated J_{ij}, the Hamiltonian of Heisenberg model is generated. The spin-orbit energy from Heisenberg Hamiltonian is used as the decision parameter in Monte-Carlo algorithm in step 2. For the Monte Carlo simulation combining atomic data sets with obtained coupling constant (J_{ij}), Heisenberg Monte Carlo software package (*Full Spin MC*) has been developed using C++. *Full Spin MC* read atomic

structure of system (primitive lattice vectors), initial collinear magnetic moments of each atoms and calculated coupling constant J_{ij} with VASP format, and generate new 3-d crystal structure. Monte Carlo simulation is performed in this 3-d crystal structure which is extended from initial primitive lattice. Our Monte Carlo simulation is based on standard Metropolis-Hasting algorithm and we considered periodic boundary condition to induce long range interaction between spins. As there's no commercial software combining KKR-CPA and Monte-Carlo, we have developed in-house Monte Carlo program based on Heisenberg model for particular study of $(Fe_{1-x}Co_x)_2B$ system. Here I present brief description of frame work of our in-house Heisenberg Monte Carlo program, *Full Spin MC* version 1.

3.3.2.1 Model Description of Simulation

The objective of this simulation is to demonstrate accurate physical picture of thermal spin fluctuation and obtain snapshot of converged spin map. The system under investigation is the ferromagnetic material systems in 3 dimensional space. Each atom has its own magnetic spin moment, and we can think of spin vectors with specific direction and specific magnitude are located in 3-d crystal structure. Thus, Monte-Carlo simulation is done for these spin moments and accepting criteria is determined by the total energy calculated by Heisenberg Hamiltonian. To adequately model the system using Heisenberg Hamiltonian, we abstract it using the activity based conceptual model. In the subsection below, we describe the various components of our conceptual model as well as details of our reasoning behind the model.

- **Input**

  To initialize Monte-Carlo simulation using Heisenberg model, firstly, following input parameters are accepted as the starting criteria.

  1. **Spin magnetic moment:** S_i

     We are assuming our system is in paramagnetic state initially which is in high temperature, and then decrease temperature that makes ordering on spin snapshot. Thus, Initial magnetic moment spin vector should be totally randomized in its orientation. Depending on the type of material we would like to model, we decide the magnitude of magnetic moment spin as the same value with element's experimental magnetic moment. Our moment spins have been determined as random direction in 3-d spherical

coordinates. We generated two pseudo random numbers for ϕ from 0 to π, and for θ from 0 to 2π using implemented random number generator in C++. By fixing $r = 1$, random unit vector of spin magnetic moment (r, θ, ϕ) has been defined in spherical coordinate. The experimental magnetic moment is, then, multiplied with this random unit vector later to generate initial magnetic spin moment.

2. **Experimental magnetic moment:** m

   The magnitude of initial spin moment, S_i, is determined by the experimental magnetic moment of material. For example, the magnitude of initial magnetic moment of Fe is $5\mu_b$. As code doesn't know what is starting magnitude of spin, we put the experimental magnetic moments of each atom as input.

3. **Temperature:** T

   Our goal is obtaining mean magnetic moment for each temperature point. Thus, we accept temperature as input and obtain mean magnetic moment from statistically converged spin map at specific temperature. The unit of temperature in simulation is $\frac{J}{k_B}$.

4. **Length of many particle system:** L_x, L_y, L_z

   The magnitude of many particle system that we would like to simulate has been defined by the length of box in Cartesian coordinate. One spin is allocated in each cell, so the number of total spins(atoms) is $L_x \times L_y \times L_z$.

5. **External magnetic field:** H

   As external magnetic field is also the component to calculate energy of system by Heisenberg Hamiltonian, we accept external magnetic field as the input. The code initially ask user to put the external magnetic field with vector format in Cartesian coordinate, and use H value to calculate energy to perform Metropolis Monte Carlo simulation.

6. **Coupling Coefficient (Exchange Interaction Term) :** J_{ij}

   The exchange interaction, J_{ij}, is the energy coefficient that determines the strength of the force exerted in an interaction between s_i (i-th spin) and s_j (j-th spin). Usually, the Lagrangian or the Hamiltonian of a system describing an interaction can be separated into a kinetic part and an interaction part. The coupling coefficient determines the strength of the

Table 3.1: Input variable for Monte-Carlo simulation using Heisenberg model

Variable	Description
S_i	Spin magnetic moment
m	Experimental magnetic moment
T	Finite Temperature
L_x, L_y, L_z	Length of many particle system
h	External magnetic field
J_{ij}	Coupling Coefficient
(x, y, z)	Atomic positions of crystal structure

interaction part with respect to the kinetic part. For the test toy model of hypothetical ferromagnetic system, we defined coupling coefficient for all pair of spins as 1. However, when we validate our simulation using test ferromagnetic material, $(Fe_{1-x}Co_x)_2B$, we accepted theoretical J_{ij} values as separate input data set and plugged into our simulation. This input file of J_{ij} values is used to calculate energy using Heisenberg model. Theoretical coupling coefficient of $(Fe_{1-x}Co_x)_2B$ has been calculated using KKR-CPA method as described above.

7. **Crystal Structure**

   Likewise, crystal structure of $(Fe_{1-x}Co_x)_2B$ has been read in our simulation program as separate input file. To make the software package compatible with DFT calculation, our simulation package is programmed to accept input file of crystal structure with $VASP$ format.($POSCAR$) For the simplified toy model, however, we didn't accept crystal structure as separate input file. Rather, we generate simple cubic structure atomic system with the magnitude of L_x,L_y and L_z.

These input variables and their descriptions are summarized in Table 3.1.

- **Output**

From the snapshot of converged spin map which we obtained from our Monte-Carlo simulation, these figure of merits have been obtained to validata simulation result.

1. **Total magnetization :** M

   When total number of spin is N, total magnetization at specific temperature T has been calculated by summing all spins up. Thus, total magnetization is magnitude of vector sum of all spins.

$$M = \sum_{i=1}^{N} s_i.$$

2. **Magnetization per one spin :** $< m >$

   $< m >$ is averaged magnetic moment per one spin.

$$< m >= \frac{\sum_{i=1}^{N} s_i}{N} = \frac{M}{N}$$

3. **Total Energy :** E

   Total energy, E, is calculated by Heisenberg Hamiltonian in converged spin map at specific temperature.

$$H = -\frac{1}{2} \sum_{ij} J_{ij} s_i s_j - \mu \sum_{i} h_i s_i$$

4. **Heat Capacity :** C_v

   From the calculated total energy for each temperature point, we can calculated heat capacity. We assume that volume is constant as increasing temperature in order to apply Gibbs Halemholtz Equation in thermodynamics.

$$C_v = \frac{dE}{dT}$$

5. **Magnetic Susceptability :** χ_m

   From the calculated total magnetization for each temperature point, we can calculated magnetic susceptability χ.

$$\chi_m = \frac{dM}{dT}$$

Table 3.2: put variable for Monte-Carlo simulation using Heisenberg model

Variable	Description
M	Total magnetic moment
$< m >$	Mean magnetic moment per unit spin
E	Total Energy in system
C_v	Heat Capacity
χ_m	Magnetic susceptability

These output variables and their descriptions are summarized in Table 3.2.

- **Activity**

1. **Metropolis Monte-Carlo Simulation**

   The main algorithm is based on conventional Metropolis Monte-Carlo simulation. Metropolis algorithm is a modified Monte Carlo scheme, where, instead of choosing configurations randomly, then weighting them with $e^{\frac{-\Delta E}{kT}}$, we choose configurations with a probability $e^{\frac{-\Delta E}{kT}}$ and weight them evenly. The activity of Monte-Carlo simulation is shown in flowchart Figure 3.4.

   Following are steps of procedure which done repeatably until achieve convergence.

   - As the very first step, we optimize δr, the movement of spin vector for each Monte-Carlo step by the acceptance rate of Metropolis algorithm. Details of optimization algorithm has been described below.
   - We place the N spins in Cartesian coordinate configuration, according to the input values L_x, L_y, L_z, in Cartesian coordinate.
   - The total energy of initial state of spin map, V, is calculated by Heisenberg Hamiltonian.
   - Then we move each of the spin in random order. The movement of spin, δr is determined by the first optimization step.
   - We calculate the total energy, V', in the modified spin map. The change in energy of the system, $\delta E = |V - V'|$ is also obtained.

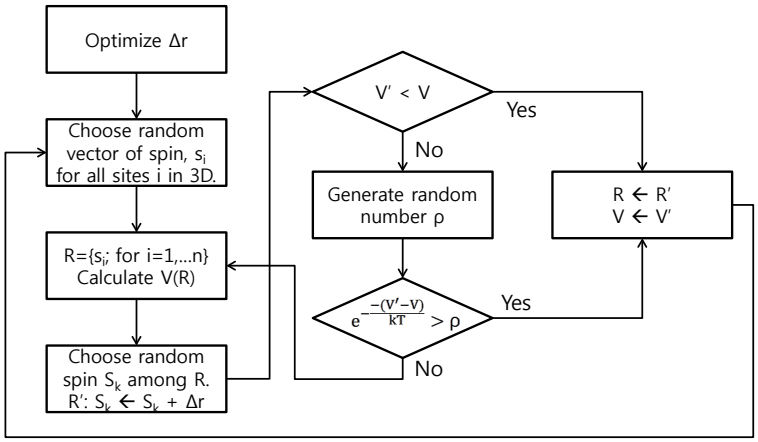

Figure 3.4: Flowchart of Monte-Carlo simulation using Heisenberg model

- If $\delta E < 0$,(i.e., if the movement would bring the system to a state of lower energy), we accept the movement and put the spin in its new position. If $\delta E > 0$, we accept the move with probability $e^{\frac{-E}{kT}}$.
- Then, depending the movement has been allowed or not,(i.e., whether we are in a different configuration or in the original configuration), we consider that we are in updated configuration.

2. **Optimization of spin movement,** δr

   As shown in Figure 3.4, we add the function to optimize step size of spin movement, δr, before we start the loop of Metropolis code. The detail of the optimization algorithm has been shown in Fig 3.6. The ideal acceptance ratio, A_r, in our Monte-Carlo calculation is 0.5. Thus, the goal of this optimization step is determine optimal δr value in our system that makes acceptance ratio as close as possible to 0.5. Firstly, we start from the initial value of $\delta r = 0.1$. Then, we calculate how many spin movements are accepted from our input system of N spins by running several Metropolis steps (We choose 1000 MC steps to obtain A_r). If acceptance ratio is less than 0.45, that means not enough movements are yet accepted and too many of them are rejected. This is because the spin movement is too large for each step and makes many of them rejected. Thus, we have to reduce the interval of movement δr by multiplying 0.99 on previous value. Otherwise, If acceptance ratio is larger than 0.55, than too many spin movements are accepted. That means movement is too conservative and too many of them are accepted. (Please refer the flowchart of Fig 3.4.

If the interval of movement, δr is zero, then $V' = V$. That makes Boltzmann probability, $e^{\frac{-(V'-V)}{kT}}$, as 1. Because 1 is always larger than random probability p, we always accept the spin movement and acceptance ratio becomes larger.) Thus, we have to increase the interval of movement δr by multiplying 1.01 on previous value.

3. **Constructing magnet object from Input file**

   The object named $Magnet$ has been constructed to define simulating topology of material system including crystal structure, magnetic moment, coupling coefficient between spins. Separate input files of crystal structure (defined in $file.dat$ with VASP format), magnetic moment $< m >$ (defined in $magnet.dat$) and coupling coefficient J_{ij} (defined in $tmp\_jrs.dat$) are combined together and generated topology of our test system to simulate.

   Here are short descriptions of input files to construct magnet object.

   - $file.dat$

     $file.dat$ is description of crystal structure in VASP format. (This input file is same as POSCAR in VASP format.) It defines lattice constant of unit cell, primitive lattice of unit cell, and location of atom in unit cell. By reading the information of crystal structure of system, code generates structure of test system to simulate.

   - $magnet.dat$

     $magnet.dat$ file defines experimental magnetic moment of specific atoms. By reading experimental values of each material, code generate initial snap shot of spins with specific magnitude of each spin.

   - $tmp\_jrs.dat$

     $tmp\_jrs.dat$ is the part of output of ab-initio calculation. Using green function based ab-initio KKR-CPA calculation, we can predict coupling coefficient, J_{ij}. Then, we have used those coupling coefficients for Monte Carlo simulation. KKR-CPA calculation is ground state calculation. However, the statistical spin fluctuation itself shows not change dramatically by the small deviation of coupling coefficient, and we assumed that it is possible to consider thermal fluctuation of spins using J_{ij} parameter from ground state calculation from KKR-CPA.

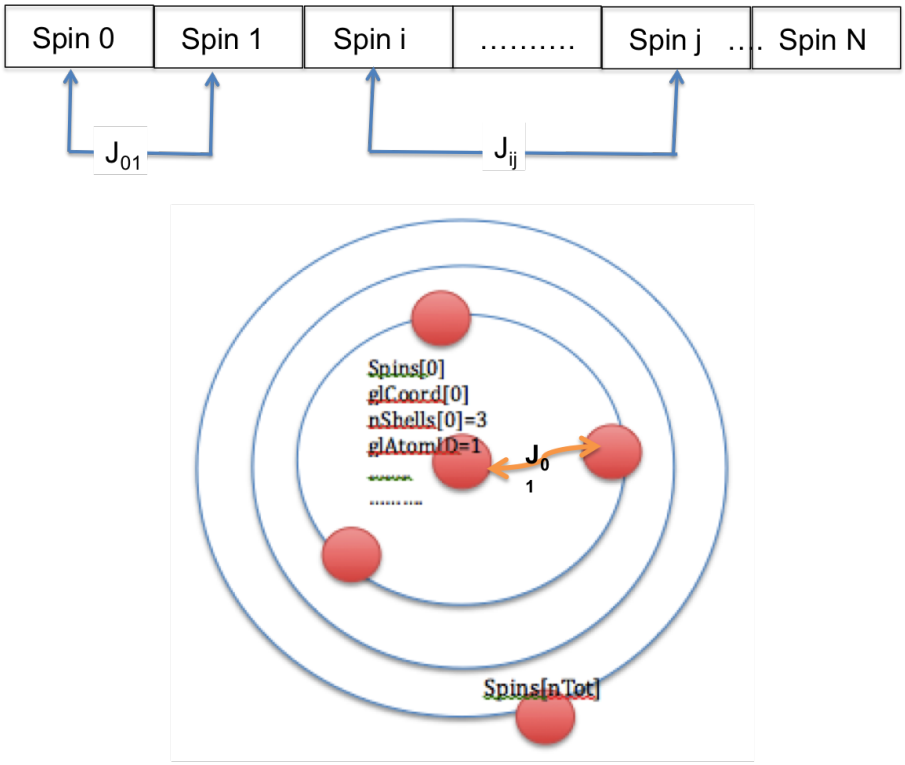

Figure 3.5: Topology of target material system as the shell structured magnetic moment spins

tmp_jrs.dat contains all pair interaction terms between each pair of atoms in shell, which is generated by KKR-DFT code, *Hutsepot*. When we run Monte-Carlo, the code read *tmp_jrs.dat* between each atom and use J_{ij} values in energy calculation using Heisenberg Hamiltonian.

The topology of spin system can be abstract and complicate. To simplify this, we can think it as the onion shaped shell structure in 3 dimensions spherical coordinate. Lets imagine there's a long list of data with N spins and each spin has its own data set describing magnetic moment of spin, position of spin in system and so on. Then, this 1 dimension data of list can be rolled as shell shape, and coupling coefficient between nearest neighboring spins are defined with coupling coefficient, J_{ij}. To better understand of input data structure, topology of spin system has been shown in Figure 3.5.

Here are some key variables in magnet object used for defining target material systems.

- **nSpecies:** number of species in system
- **nAtoms[1-nSpecies]:** number of atoms of each species in the simulation cell
- **basis[1-nSpecies][1-nAtoms]:** coordinates of each atom of each species
- **nTot:** total number of atoms of all species in the simulation cell
- **glCoord[1-nTot]:** coordinate of each atom
- **spins[1-nTot]:** spin vector for each atom
- **glSpeciesID[1-nTot]**: type of species for each atom in the global list (values are 0 to nSpecies-1)
- **glAtomID[1-nTot]:** ID number of atom (values are 0 to nAtoms-1 for each species)
- **nShells[1-nTot]:** total number of neighbor shells around each atom
- **shellRadius[1-nTot][1-nShells]:** squared distance to each neighbor shell
- **shellSize[1-nTot][1-nShells]:** number of neighbors in each shell
- **shellNbr[1-nTot][1-nShells][[1-shellSize]:** index of the neighbors in this shell (values are 0 to $nTot - 1$)
- **J[1-nTot][1-nShells][1-shellSize]:** coupling constant for each pair

4. **Calculating outputs from converged spin map**
   From the convergence test of total energy and total magnetization, the proper number of Monte-Carlo steps has been obtained. Typically, 10^4 Monte-Carlo steps are enough to converge spin map for 32 atomic system of $(Fe_{1-x}Co_x)B$. From the snapshot of converged spin map, the figure of merits have been obtained.

3.3.2.2 Details of source code package

Our package contains bunch of files including (1) source files (*.cpp) and header files(*.h) ,(2) makefile, (3) bashscript. Here are the brief descriptions of each files.

1. **Source and header files**

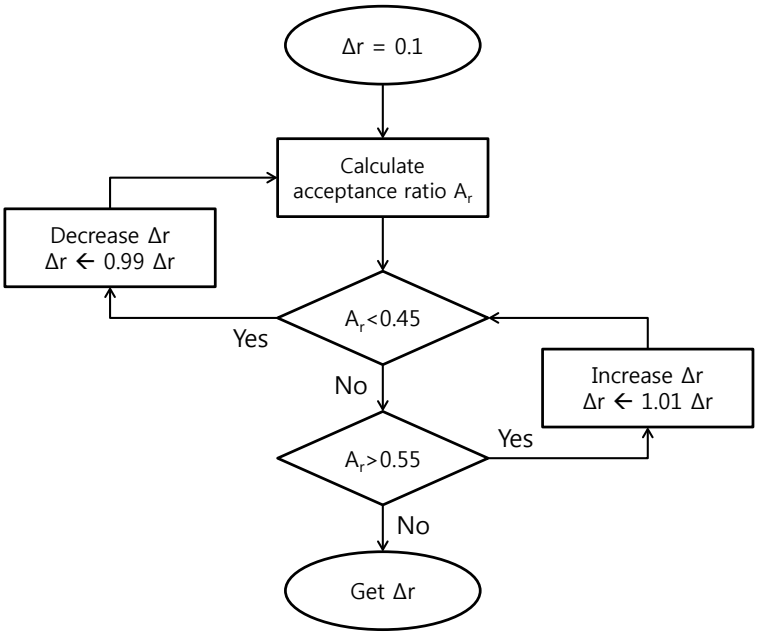

Figure 3.6: Algorithm to optimize δr, the movement of spin vector

- KKR.cpp KKR.h:
  It parses the data of all pair interaction terms between each pair of atoms in shell in $tmp\_jrs.dat$, which is generated by KKR-DFT calculation and use them to construct crystal topology.
- crystal.cpp crystal.h:
  It reads the crystal structure (unit cell lattice, species, atomic basis, analogous to pieces of VASP INCAR file), and construct a periodic super-cell.
- magnet.cpp magnet.h:
  It plug J_{ij} parameters read from KKR module on crystal structure read from *crystal* module to define spin configuration on the top of crystal structure to perform Monte Carlo Calculation. Magnet code contains many functions dealing with structure. The main role is to read the crystal structure through *crystal* and J data through KKR and replicate the structure $n \times n \times n$ times and reformat as a magnet structure.
- vector.cpp vector.h:
  This module is combination of some math functions related to the vector calculations that we will use for Hamiltonian calculation containing transpose, determination, dot product and normalization etc.
- findnRhomb.cpp:

It determines the dimension that we will perform Monte Carlo calculation. Considering we have big spin configuration in our system, we can select specific part of spherical volume and do the Heisenberg MC calculation only inside of the specific regime. We firstly give the radius of sphere,r_{max} , and code finds how many unit cells we must sum over to encompass that sphere.

- heisenberg.h heisenberg.cpp:
  This is the core module which contains main function to perform Heisenberg Monte Carlo calculation including initialization of random spin configuration, thermalization and actual Monte Carlo steps starting from magnet object. Again, *magnet* module inherit KKR module containing J coupling information for each pair of atoms and crystal objects containing crystal structure and coordination information.

2. **Makefile**
   It compiles all the source code, connect each other and generate one executable named $heisenberg$.

3. **Bachscript**
   This script is for the automation purpose. The $run\_multi.sh$ containing all sequential inputs we will put into executable.

Basically, our Heisenberg program can be divided by big 6 parts depending on its functions. Every parts are supposed to be done sequentially.

- **Part 1: Get data and construct magnet object**

  Here, we need $file.dat$ and $mfile.dat$ in addition to $tmp\_jrs.dat$ to construct *magnet* object. $file.dat$ is coordination information with VASP format[58] containing information such as lattice constant, coordination of atomic positions and primitive lattice vectors. $mfile.dat$ is the information of spin vector. The initial spin snapshot is generated using $Heisenberg\_init.cpp$ with totally randomized direction. Once we construct atomic structure from $file.dat$ and match with spin vector from $mfile.dat$, coupling constant(J) between each pair

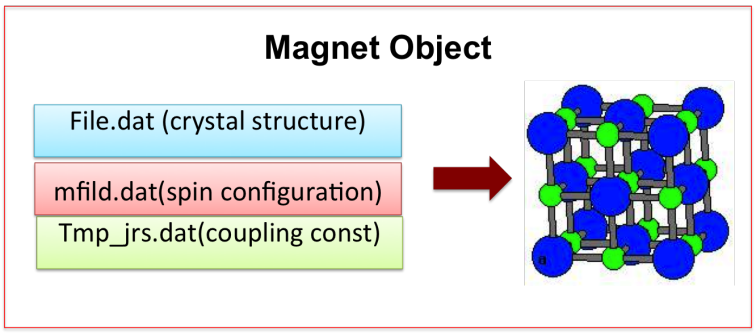

Figure 3.7: Constructing magnet object from input files

of atom is matched between each spin. Magnet object is chunk of data structure combined those three data sets to describe physical property of material, $file.dat$, $mfile.dat$ and $tmp\_jrs.dat$, to describe physical property of material (Figure 3.7).

- **Part 2: Replicate super cell from unit cell**

  In this part, program accept the input L_x, L_y, L_z from user and replicate unit cell by $L_x \times L_y \times L_z$. The total number of atom (nTot) of system would be same as the number of atoms in unit cell times $(L_x \times L_y \times L_z)$.

- **Part 3: Initialize spin as a random fluctuation**

  This is the part to initialize all the necessary parameters we need to run Monte Carlo. Code accept input of temperature (T), magnetic field (H) from the user and save it into the *magnet* object. In addition, it generate randomly distributed spin map which is being used as the initial starting data of Monte Carlo step. We also put the optional question whether we will start our Monte Carlo calculation from previous run or not. This is because sometimes MC couldn't finish for long step sizes due to the time limit. In this case, we can continue the MC calculation from previous MC step rather than starting from the very first step to save running time and computational cost. If we choose to do so, the code is not generating random initial spin map but get the spin map output from previous calculation. The spin map is automatically stored as the name of $Initial\_T.data$ and this data set is updated for each MC step. Thus, we should keep in mind whether $initial\_T.data$ from previous MC run

is stored in same folder where we run the Heisenberg program before we start.

- **Part 4: Copy magnet object to dummag and optimize deltamax**

  The *deltamax*, δr is the rotation step size of spin depending on temperature. At low temperature, the spin fluctuation would be conservative so as low deltamax. Obviously, opposite in high temperature (large spin fluctuation and higher deltamax.) In part 4, we optimize the spin movement step size (*deltamax*) depends on temperature. Generically, we change the step size depending on acceptance ratio of metropolis MC algorithm as described in previous section.

- **Part 5: Accept local magnetic moments of each material**

  In this part, we get the input of local magnetic moment of materials in our system as the input for the purpose to obtain total mean local magnetic moment of each different species as the output later on.

- **Part 6: All Monte Carlo Steps for MCStep sizes**

  In this part, we start the loop of Monte Carlo calculation. The code is programmed to perform MC steps for single temperature point calculation. First, we start thermalization by doing several Monte Carlo spin update procedure and perform MC steps for long step sizes (typically more then 1000 steps). At the end of the MC runs, code calculates $< m >$-total average magnetic moment, $< m\_A >$-local magnetic moment of material A ,$< m\_B >$-local magnetic moment of material B, $< e >$-energy, Cv-heat capacity ($= \frac{dE}{dT}$) for given temperature point. Then, calculated figure of merits are written on *output_T* file. There are three output files that the code generate as the output. (1) *output_T* containing physical properties (m, e, C_v) (2)*iniitla_T.data* writing spin configuration of latest MC step, (3)*time_consumption.out* tracking consumed time for each time step.

3.3.3 Obtaining T_C from Monte Carlo simulation

We calculate T_C from a standard Monte-Carlo algorithm in step 3 above. We find that including the interactions with the nearest 1000 neighboring sites is sufficient to converge the Monte Carlo calculations with the Heisenberg Hamiltonian. There are two ways to determine the T_C from Monte-Carlo result. First method is plotting the normalized average magnetic moment from converged spin map, $< m > /m_{max}$, versus temperature, and read the temperature where the normalized average magnetic moment is 0.5. Second method is identifying the peak in the T-dependent heat capacity, C_v, for each concentration. We determined T_C by the second method.

3.4 Results

There are two parts in this section. Firstly, I present output analysis obtained from our program *Full Spin MC*. The calculated figure of merits are shown as the result of our Monte Carlo simulation program using Heisenberg model. Secondly, the capability of our program, *Full Spin MC*, to predict curie temperature of $(Fe_{1-x}Co_x)_2B$ ferromagnetic family has been discussed by comparing with experimental data.

3.4.1 Output analysis from Monte Carlo simulation

3.4.1.1 Obtained Figure of Merits from Full Spin MC

The system of Fe atoms in 3-d cubic lattice structure has been selected as our test material. This is because: (1) Iron is most well-known ferro-magnet with magnetic moment of $5\mu_B$ and almost same coupling coefficient $J = 1$ for all sties. (2) The simple bcc structure of Iron in cubic lattice is easy to simulate. (3) Experimental values of thermo-magnetic figure of merits are well-known, thus validation of our simulation is easy. The figure of merits in Fe system, which are described in this section, have been calculated using our Monte-Carlo simulation based on Heisenberg model. Obtained figure of merits are shown in Figure 3.10

1. **Magnetic moment $< m >$ versus temperature**
   In case of zero external field, It shows sharp decrease at around $750K$. This means that the initially aligned spin (i.e.: $< m >$=1) at zero temperature

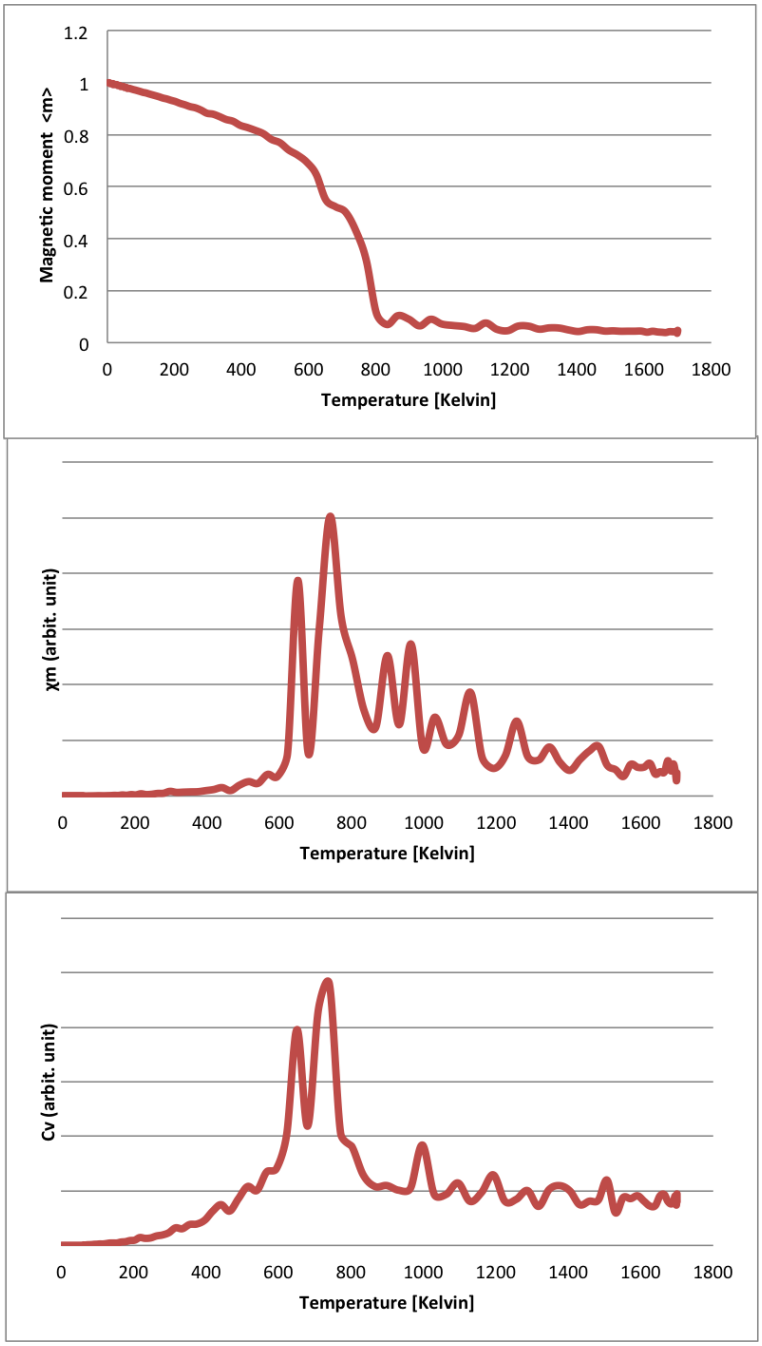

Figure 3.8: Obtained outputs from Heisenberg Monte Carlo simulation. From top to bottom, magnetic moment per single spin ($< m >$) versus temperature, magnetic susceptibility per spin (χ_m) versus temperature and heat capacity at constant volume in system (C_V) versus temperature

abruptly randomized at specific temperature as increasing temperature and finally reaching to zero. (i.e: $< m >$=0). This is the second order transition from ferromagnet to paramagnet. Curie temperature is the temperature where the second phase transition occurs. We can obtain T_C by reading the temperature point where $< m >$ is half in this plot. In case of Fe cubic system, It shows T_C is around $750K$ which is little bit underestimated than experimental value of $840K$.

2. **Magnetic susceptibility χ versus temperature**
   The magnetic susceptibility of the system measures the response to changes of magnetization in temperature.

$$\chi_m = \frac{dM}{dT} = \frac{1}{k_B T}(< M^2 > - < M >^2)$$

   In the source code, we simply calculated $< M^2 > - < M >^2$ as susceptibility with arbitrary unit. Magnetic susceptibility χ_m versus T in Figure 3.10 shows that χ_m diverges at around T_C which is $750K$. Again, It is second order phase transition. Above T_C, it is paramagnetic.

3. **Heat Capacity C_V versus temperature**
   The heat capacity at constant magnetic field H of the system measures the response of total energy changes by temperature.

$$C_V = \frac{dE}{dT} = \frac{1}{k_B T^2}(< E^2 > - < E >^2)$$

   The heat capacity can be measured in two ways.

   (a) Measure <E> as a function of temperature T and find the derivative numerically.

   (b) Measure the fluctuations of the energy at fixed temperature using the fluctuation-dissipation formula.

   In the source code, we simply calculated $< E^2 > - < E >^2$ as heat capacity with arbitrary unit. The deviation of C_V at around T_C which is 750 $Kelvin$ shows second phase transition from ferromagnetic to paramagnetic.

3.4.1.2 Finite Size Scaling

Finite-size scaling or Finite-size effects are related to the fact that we can only simulate systems of finite sizes. Contrarily, in nature, systems usually approach very large sizes, i.e. they are in the thermodynamic limit. [46] When the length scale is smaller than correlation length, the correlation length in simulation is reduced and this will affect to the simulation result. We call this as 'Percolation effect'. Let's discuss the percolation effect in our simulation model. In our Monte-Carlo simulation, the size of the system is the number of spin sites in the lattice. There is a single control variable, which is a probability p that a lattice site is occupied. Now, let's consider a square lattice with $N \times N$ sites. A site can be occupied or empty, so its state can be represented using a Boolean variable, say true for occupied or false for empty. Each interior lattice site has six nearest neighbor in 3-dimensional cubic lattice. A cluster on the lattice is a set of occupied sites mutually connected as nearest neighbors.

A percolating cluster or spanning cluster has at least one site on each of the six boundaries of the lattice. The percolation problem assumes that each site can be used to generate a typical sample. There is a critical probability p_c below which spanning clusters are extremely rare and above which they become a increasingly common. As total number of atom, N, is increasing to infinity, this transition becomes sharp, like the phase transition from a ferro-magnetic to a para-magnetic at the Curie temperature T_c. Contrarily, If N is too small compared with correlation length, It is hard to reach to the critical probability p_c to generate domain cluster. In this case, there shows convergence problem in simulation result. For example, mean magnetic moment required more energy (higher temperature) to randomize spin domains by fluctuation, thus higher Curie temperature then it should be as shown in Figure 3.9.

3.4.2 Results for $(Fe_{1-x}Co_x)_2B$

As mentioned above, $(Fe_{1-x}Co_x)_2B$ has interesting property in Curie temperature that varies by different Co-concentration, x-value. Thus, we choose this material to validate our simulation model whether it correctly predict correct Curie temperature by varying x-values in $(Fe_{1-x}Co_x)_2B$. To do this, average magnetic moment $< m >$

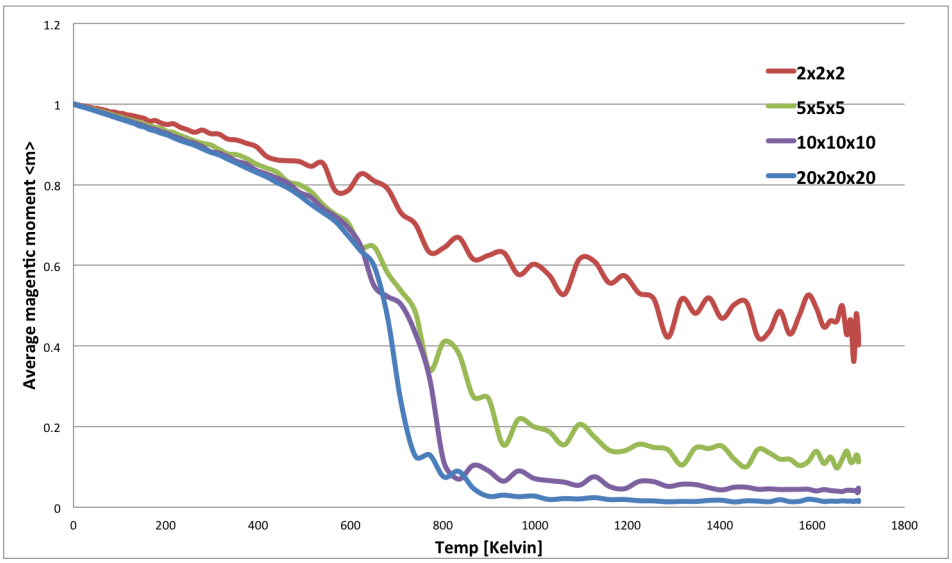

Figure 3.9: Magnetic moment per single spin ($< m >$) versus temperature with varying length scale. As length scale increases, the aligned spin system (clustered spin system at T=0K) is randomized faster so T_C is reaching to the right value (for Fe $T_C = 800K$) and curve becomes more sharp. This shows the convergence problem induced by finite size scaling effect

have plotted versus temperature for different Co-concentrations. The Curie temperature is, then, collected from magnetic moment curve by reading temperature where $< m >$ is half of maximum ($i.e$: 0.5 %). As the results shown (Figure 3.10), Curie temperature has decreased as increasing x, Co-concentration. As shown in plots, T_c is about 1100 K at x=0, 900 K at x=0.50,700 K at x=0.75 and 500 K at x=0.90.

Likewise, curie temperatures for all x value from 0 to 1 have been collected and compared with experimental data and conventional DFT result. Figure 3.11 displays our results (dashed red curve) along with those of experiment [101] (dashed blue curve) and DFT calculation with mean-field approximation (solid black curve). As shown in Figure 3.11, the result from our simulation shows great agreement with experimental values. Compared with mean-field DFT calculation which is overestimated T_c about 40% (when x =0) to 50% (when x=1), the agreement is excellent, though notable deviations can be seen for small x. Still, this level of agreement indicates that our assumptions regarding the absence of major x-dependent structural modifications are probably correct, since significant (x, T)-dependent modifications to the crystal structure of the real system would likely result in larger changes to $T_C(x)$ (it is noteworthy that the elemental Fe and Co systems in their native lattices have $T_C[Fe] < T_C[Co]$, in contrast to the result shown here and in [101] for Fe_2B and Co_2B). While this

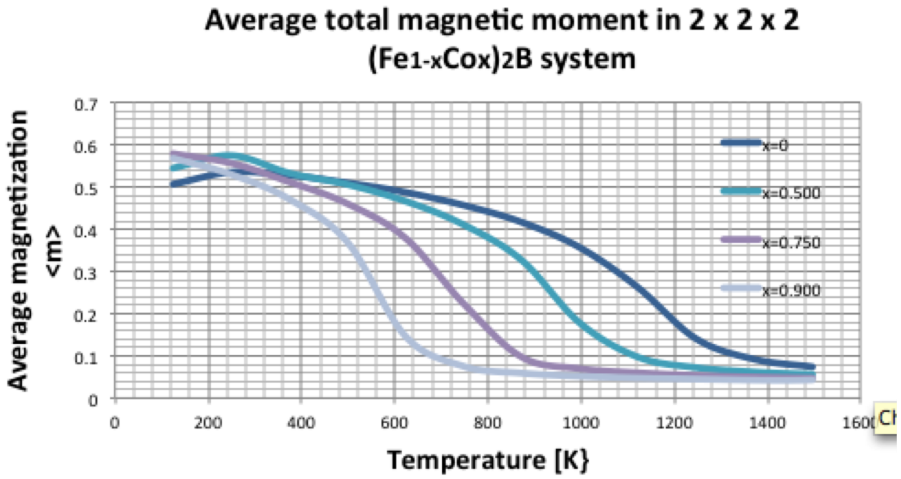

Figure 3.10: magnetic moment per atom in $(Fe_{1-x}Co_x)_2B$ versus temperature for different Co-concentration,$x - value$.

result for the Curie temperature is somewhat decoupled from those that follow, it is at least encouraging that this important property is described well by PBE pseudo potential for the assumed $C16$ structure with complete $FeCo$ substitutional disorder as modeled by the CPA.

3.5 Discussion

As shown in Chapter 2, ab-inito DFT method can be used to predict thermo-magnetic properties of material especially when electronic entropy or vibration entropy is the key modeling criteria to define physical figure of merits or materials, and other effects, such as configuration entropy change or thermal magnetic entropy contributions, are considered negligible. However, in solving problems dealing with hard permanent families such as searching rare-earth substitutes, It has been noted that there's significant limitation in applying DFT method alone. Because the complex magnetic degree of freedom presents in material systems which is not been covered in DFT method. Also, the ground state analysis is not sufficient for permanent magnets which should be investigated from low temperature to extreme high Curie temperature. Most importantly, the statistical interaction between thermo-magnetic spin movement are neglected in DFT calculation. Therefore, an extension of DFT method to finite temperature in particular for permanent hard magnets requires new hybrid modeling routine combining DFT method with statistical simulation of thermodynamics between each spins. In this Chapter, we have been resolved these issues by

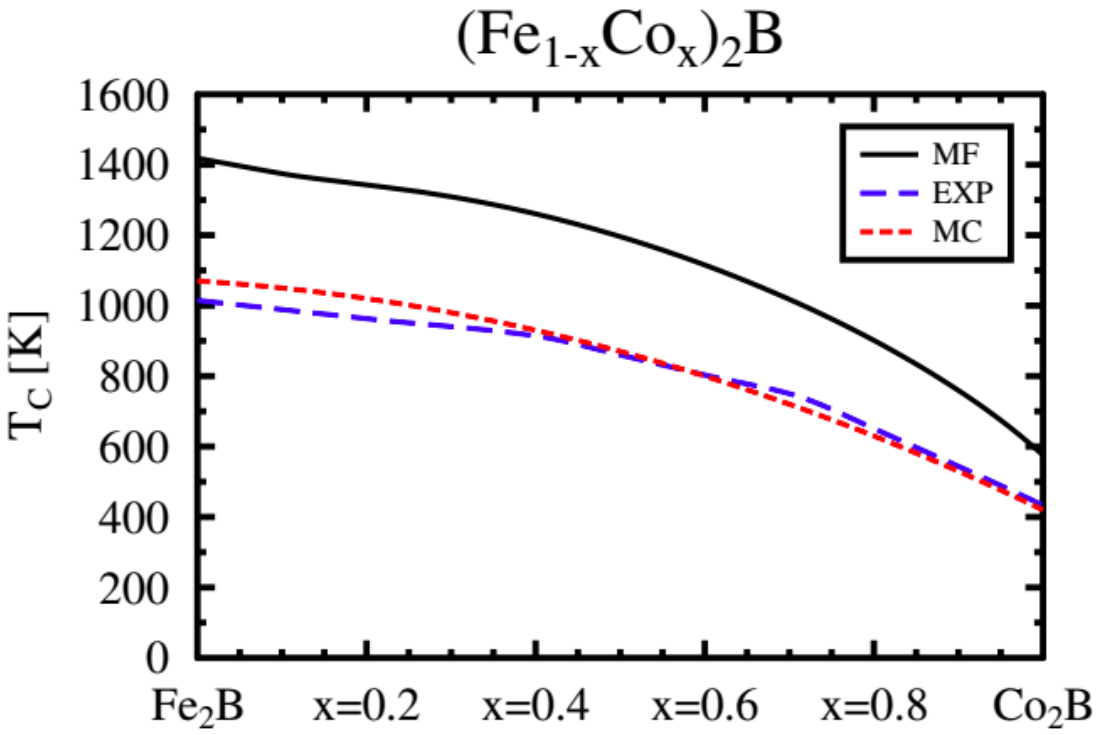

Figure 3.11: Curie temperatures, T_C, versus Co-concentration for the $(Fe/Co)_2B$ system. Experimental data [101] are indicated by blue bashed curve. Black solid curve shows the result of our DFT calculation using mean-field approximation(MFA) using KKR implementing disordered-local moment and CPA. The local CPA is employed to describe the disordered system, in accordance with the mean-field nature of the probability density. Red dashed curve shows the results of our PBE calculation of exchange parameters using KKR-CPA, together with a determination of T_C using a Monte Carlo (MC) approach as applied to the resulting Heisenberg Hamiltonian, in which 1000 nearest-neighbor couplings are used.

combining Monte Carlo simulation with ab-initio KKR-CPA method. Because the most established magnetic Hamiltonian for ferromagnetic state of permanent magnet is the Heisenberg model, and we used Heisenberg model based Metropolis Monte Carlo method for our system,$(Fe_{1-x}Co_x)_2B$. The observation of Curie temperature in $(Fe_{1-x}Co_x)_2B$ in results showed, Monte-Carlo simulation of thermal fluctuation of magnetic moment can statistically address spin orbit coupling and dynamics in high temperature. Heisenberg model considering every spherical orientation of magnetic spin moment will achieve our aim to represent accurate spin reorientation in finite temperature.

The modeling routine have three steps of procedure,

- Step 1: Obtaining coupling constant J_{ij} in Heisenberg Hamiltonian from KKR-CPA calculation in zero-temperature.
- Step 2: Plug in J_{ij} parameters between each atoms and experimental magnetic moments of Fe, Co and B in our Monte-Carlo source code.
- Step 3: Run the Monte-Carlo simulation and obtaining snap shot of spin dynamics and Curie temperature.

The result from our simulation procedure shows great agreement with experimental values. Compared with mean-field DFT calculation which is overestimated Tc about 40%, the agreement is excellent, though notable deviations can be seen for small x. Our result clearly shows that our hybrid modeling method combining DFT and Heisenberg Monte Carlo has the better capability in predicting thermo-magnetic properties of $(Fe_{1-x}Co_x)_2B$ compared with single DFT method. Our results also suggest that the task to predict thermo-magnetic properties of hard permanent material systems, other than our test system of $(Fe_{1-x}Co_x)_2B$, can be fully benefited from this new hybrid modeling approach that we have proposed here.

Chapter IV

CALCULATING MAGNETIC CONTRIBUTION OF STACKING FAULT ENERGY IN STAINLESS STEEL USING LSF-MC SIMULATION

4.1 Motivation

The austenitic stainless steel is used for many engineering application. Specifically, annealed (i.e, low-strength) type 316/316L stainless steel with nickel content greater than 12 wt% is widely used for the baseline material for balance of plant(BOP) applications on-board fuel cell electric vehicles (FCEVs). Since the cost of austenitic stainless steel alloy is roughly proportional to the nickel content inside, it would have the large amount of economical benefit if alloys with lower nickel content can be substituted. Also, low-strength requires thicker walls and heavier components. Therefore, by identifying low-nickel, high-strength alternatives to type 316, the cost and weight of components for BOP can be significantly reduced. The primary objective of this project is to search stainless steel alloys with low-Ni content (and thus lower cost) and with reasonably low-strength to replace type 316/316L for BOP application. To achieve this goal, we have screened a wide range of compositional space of $Fe-Cr-Ni$ Stainless Steel system to identify alloy composition that have potential to replace 316/316L and calculated stacking fault energy for the systems.

To accurately calculate stacking fault energy of the given systems, we have developed a quantum-based material exploration and design capability - one that combines ab-initio DFT calculation and Monte-Carlo based on Longitudinal Spin Fluctuation (LSF) model. Specifically, It is well known that the local magnetic moments in Fe, Cr, and Ni survive in their high-temperature paramagnetic states. Also, low magnetic transition temperature Fe-rich $Fe-Cr-Ni$ solid solutions suggests the possibility that in $Fe-Cr-Ni$ stainless steel alloys disordered local magnetic moments might be present at ambient conditions as well. Therefore, those persisting moments give rise to sizable contributions to the specific heat and entropy, and the magnetic entropy from magnetic moment fluctuation becomes critical role to domain

total stacking fault energy of austenitic $Fe-Cr-Ni$ stainless steel. We have used hybrid-method combining ab-initio DFT calculation and Spin Monte-Carlo simulation based on Longitudinal Spin Fluctuation model to calculate the snapshot of magnetic moment spins due to thermal fluctuation in certain temperature range of paramagnetic state. From obtained snapshot of magnetic moment at different temperature, we have calculated magnetic contribution of stacking fault energy on different chemical composition of $Fe-Ni-Cr$ austenitic stainless steel at different temperatures.

4.2 Theoretical Background

4.2.1 SFE in Stainless Steel

A stacking fault (SF) is a planner defect in a crystal which is the interruption in the perfect stacking sequence of the atomic layers [43]. Fully austenitic stainless steels are composed mainly of Fe, Cr, and Ni, and have the face centered cubic (fcc) crystallographic structure of γ-Fe (Fig. 4.1). Therefore, I present a short description of stacking faults in fcc crystals here. From the lattice vectors of the cubic cell of the fcc structure, we can see the stacking direction is indicated by [111], and the close-packed layers lie within the {111} planes.

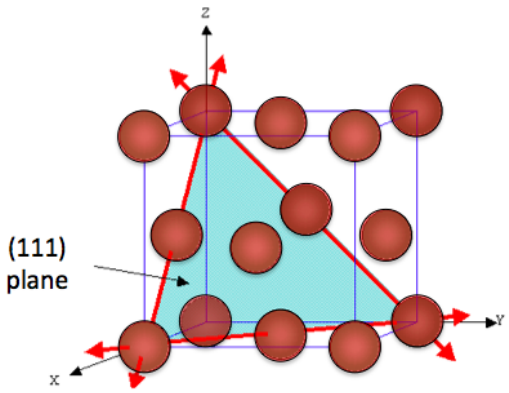

Figure 4.1: Face Centered Cubic Crystallographic Structure of γ-Fe

The stacking direction is determined by the plane which three lattice vectors of crystal structure generates. In case of the cubic cell of the fcc structure, the stacking direction is [111] using the lattice vectors. Therefore, the close-packed layers also lie within the {111} planes.

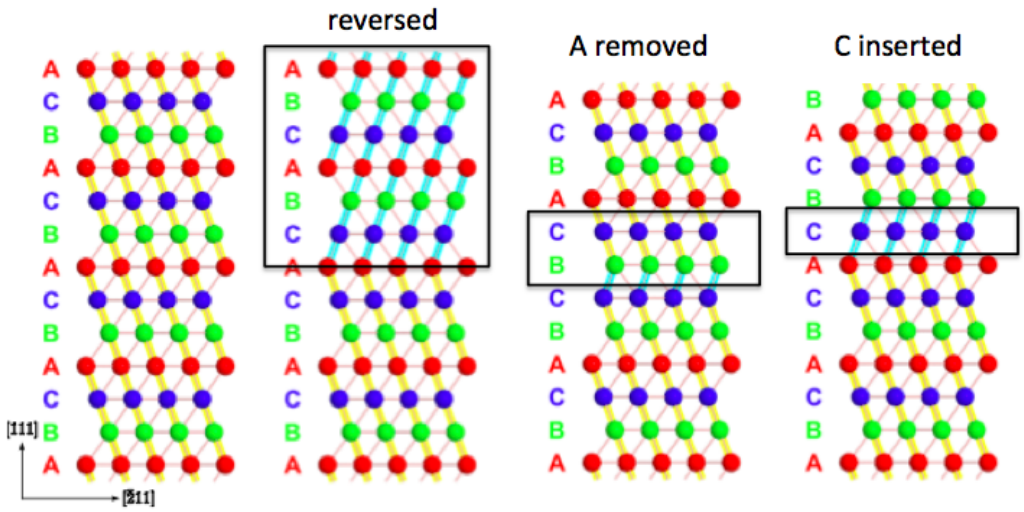

Figure 4.2: Left most figure: The stacking sequence in a perfect fcc structure. (The perfect stacking sequence has been highlighted by yellow color.) Second figure: The structure with the reversed stacking sequence. Third figure: An intrinsic SF is generated by removing A-layer from the perfect sequence. Right most figure: An extrinsic SF is generated by inserting C-layer into the perfect sequence (Source: John Price Hirth and Jens Lothe. Theory of Dislocations. John Wiley & Sons, 2 edition)

Three types of stacking fault can be generated in fcc structure. (Fig. 4.2) Firstly, stacking fault can be driven by twinning. Twinning is considered as 180deg of one crystal half in glide plane which is {111} planes in case of the cubic fcc structure. Twinning can be considered as the mirror plane reflection about the {111} plane. As shown on the second figure in Fig. 4.2, based on the centering layer A on the middle, the order of stacking of the close-packed layers is mirrored. In this case, centering layer A is the twin plane and also the center of the fault. Secondly, the intrinsic stacking fault can be generated by removing a layer from the prefect sequence. As shown on the third figure in Fig. 4.2, an intrinsic stacking fault corresponds to removing the centering layer A in perfect crystal. In this case, the normal sequence remains unchanged on either side of the faults right up and right down to the fault plane. Therefore, the perfect stacking sequence (which has been highlighted by yellow color) would be same as **...A-B-C...** on above and below side of the fault plane (which has been highlighted by black box) in Fig.4.2. Thirdly, the extrinsic stacking fault can be generated by inserting a layer from the perfect sequence. As shown on the left most figure in Figure 4.2, the extrinsic stacking fault corresponds by inserting the centering layer C in perfect crystal which has been highlighted by black box. Again, the normal sequence remains unchanged on either side of the fault plane.

The stacking fault rearranges the close-packed layers in a lattice. Therefore, the total energy of the crystal changes due to the stacking fault. This energy change is defined as the stacking-fault energy (SFE), which is a material property on a very small scale, in units of milli-Joules per square meter (mJ/m^2). The most common stacking fault in an fcc crystal is the intrinsic staking fault by missing [111] layer from the perfect lattice. Thus, the stacking fault energy in an fcc crystal, γ can be defined as the excess free energy δF per unit interface area.

The most sophisticated method to calculate stacking fault energy is using first-principles DFT calculation applying super-cell techniques. However, as it requires large cell, this method takes lots of effort to make system converged and also computationally expensive. The alternative and more efficient method is to obtain stacking fault energy by the difference of the free energies of bulk unit-cells with fcc, hcp and double-hcp (dhcp) structure. The excess free energy δF is driven from the free energies of the hcp, dhcp, and fcc lattices by taking into account interaction between layers up to the third nearest neighbor within the axial interaction model. Here, I presents brief summary of method to obtain the excess free energy δF by applying, so-called, the axial-next-nearest-neighbor Ising (ANNNI) model [53, 2].

The axial-next-nearest-neighbor Ising model is a variant of the Ising model in which competing ferromagnetic and antiferromagnetic exchange interactions couple spins at nearest and next-nearest neighbor sites along one of the crystallographic axes of the lattice. The model is a prototype for complicated spatially modulated magnetic superstructures in crystals. In ANNI model, we represent the Helmholtz free energy as the interaction between Ising spins in a similar fashion as Heisenberg model but using Ising spins. On each closely packed layer, the Ising spin S_i for layer i, has a value $+1$ if the next layer with $i+1$ does confirm the ideal stacking sequence. Otherwise, the Ising spin S_i for layer i has a value -1 if the next layer with $i+1$ does not matched with the ideal stacking sequence. Using the representation of ANNNI model, the Helmholtz free energy of any arbitrary stacking sequence can be represented as following,

$$F = F_0 - J_1 \sum_i S_i S_{i+1} - J_2 \sum_i S_i S_{i+2} - J_3 \sum_i S_i S_{i+3} \tag{4.1}$$

The F_0 is the energy contribution the energy contribution disregarding all interactions between layer. The parameter J_n is the interaction energies between two layers that are nearest neighbors (J_1), next-nearest neighbors (J_2). As the interaction energies

decreases as increasing spacing between each later, it is expected that the magnitude of J_n decreases for increasing n. By definition, in the ANNNI model, all J_n with $n \geq 3$ are neglected.

In the fcc lattice, an intrinsic stacking fault, which corresponds to the removing of one atomic layer(let say A-layer as an example) from the perfect $ABCABCABC$ structure, can be represented as the arrangement of atomic layers with repeat unit of $ABCBC(ABC)^n$ ($n = 0, 1, 2, ...$), of N layers ($N = 5, 8, 11, 14, ...$) in the limit $N \to \infty$. In the limit of large N, we can represent the Helmholtz free energies of different crystal structural phase, fcc, dhcp, hcp, using above equation (4.1) according to the stacking sequence with different repeat units. In this case, note that the energies are normalized to a unit cell in one layer, and J_0 is the energy per unit cell in one layer if the interaction between layers are disregarded.

ABC $\qquad F^{fcc} = J_0 - J_1 - J_2 - J_3 - J_4....$

AB $\qquad F^{hcp} = J_0 + J_1 - J_2 + J_2 - J_4....$

$ABAC$ $\qquad F^{dhcp} = J_0 \quad + J_2 \quad - J_4....$

Using the above three Helmholtz energy for three structural phases, fcc, hcp, dhcp, J_0 can be derived as,

$$J_0 = \frac{F^{fcc} + F^{hcp} + 2F^{dhcp}}{4} + O(J_4) \tag{4.2}$$

Also, using above Eq. (4.1), we can derive the Helmholtz energy for stacking with intrinsic stacking fault,$ABCBC(ABC)^n$, as following.

$$ABCBC(ABC)^n \qquad F^{ISF} = J_0 - \frac{N-4}{N}J_1 - \frac{N-4}{N}J_2 - \frac{N-4}{N}J_3.... \tag{4.3}$$

Combining Eq. 4.2 and 4.3, the energy difference between a structure with a ISF and the fcc bulk structure, both of the same thickness equal to N layers, is defined as following,

$$\begin{aligned} \lim_{N\to\infty} N(F^{ISF} - F^{fcc}) &= 4(J_1 + J + 2 + J_3 + J_4 + ...) \\ &= -4(F^{FCC} - J_0) \\ &= F^{hcp} + 2F^{dhcp} - 3F^{fcc} + O(J_4) \end{aligned} \tag{4.4}$$

In ANNNI model, we assume that the interaction term, J_n is negligible when $n \geq 4$. Thus, the last term, $O(J_4)$ can be dropped. As the fcc, hcp and dhcp structure can

be represented as the layered structure in hexagonal plane, the number of atomic sites per volume is equal in ideal fcc, hcp, and dhcp structure. Therefore, we can rewrite the above equation in terms of the Helmholtz free energies per atomic site, F, by dividing above equation with area, A, in a close-packed layer occupied by a single atom site. The area, A, can be derived as the area of triangular unit cell on hexagonal close-packed area in terms of the fcc lattice parameter as following:

$$SFE(T) = \frac{F^{hcp}(T) + 2F^{dhcp}(T) - 3F^{fcc}(T)}{A} \tag{4.5}$$

$$A = \frac{\sqrt{3}}{4} a_{fcc}^2 \tag{4.6}$$

4.2.2 Fe-Cr-Ni system

Austenite phase is one of the major constituent phases of stainless steels. Austenitic stainless steels, so-called 300 series, make up the major part of the stainless steel production. The chemical composition of austenitic stainless steels usually include carbon which kept to low level, chromium content ranging from 16 to 28 wt%, and nickel content ranging from 3.5 to 32 wt%. Such a chemical composition allows stainless steels maintain an austenitic structure for the large temperature ranges (from cryogenic temperature to the melting point of the alloy). Austenitic stainless steels widely used for many applications because of its high corrosion resistance and excellent mechanical properties such as ductility and toughness [14]. Also, this steels represent the primary choice for nonmagnetic engineering materials. One of the applications is annealed type $316/316L$ austenitic stainless steel which is used for balance of plant (BOP) application on-board fuel cell electric vehicle. The importance of austenitic stainless steels in many application motivates investigations for finding efficient production and shaping method which apply shear stresses on steels. Therefore, accurately predicting SFE of austenitic stainless steels is significant for application purpose.

It is known that, provided a sufficient amount of Ni and proper heat treatment, fully austenitic stainless steels are composed mainly of Fe-Cr-Ni alloy over a broad range of temperature including room temperature, and have face centered cubic crystallographic structure of $\gamma - Fe$. The SFE of Fe-Cr-Ni alloy, in turn, depends on temperature on the chemical composition of the alloy. This is because magnetic properties of Fe-Cr-Ni alloy dynamically varies through temperature ranges. At low temperature,

depending on the chemical composition of the alloy, the magnetic structure of Fe-Cr-Ni system exhibit a large variety ranging from ferromagnetic phase to spin-glass and anti-ferromagnetic alignment. [69, 80] When temperature goes up to an ambient condition, the austenitic steels have low magnetic permeability and are regarded as nonmagnetic.

As mentioned, the SFE of Fe-Cr-Ni system depends on temperature. This is because the local magnetic moments in Fe, Cr and Ni still persist in their high-temperature paramagnetic states [97, 39, 85]. The magnetic transition temperature of Fe-rich Fe-Cr-Ni alloy are solid solution are unexpectedly low which is below 100 K [69]. This suggest that these alloys disordered local magnetic moments might be also present at ambient condition. Those surviving disordered local magnetic moments make the contribution to the specific heat and entropy, and the magnetic entropy contribution is not negligible to ignore. Therefore, we are considering magnetic entropy contribution on total stacking fault energy of stainless steels. In particular, by using computational framework based on first-principle alloy theory combining ab-initio DFT calculation and Monte-Carlo method, the direct estimation of the magnetic entropy term due to the magnetic spin fluctuation in Fe-Cr-Ni, and verify the importance of thermo-magnetic properties on mechanical strength of austenitic Fe-Cr-Ni stainless steels.

4.2.3 Magnetic Entropy Contribution

In finite temperature, the various excitation may occur in random alloy that change microscopic configuration of system. The total entropy is calculated by considering variations of all microscopic configurations that correspond to a thermodynamic system in a state specified by certain macroscopic variables. There are four types of entropy depending on the excitation of microscopic configuration: vibration entropy, configuration entropy, electronic entropy, and magnetic entropy. Then, total entropy of system is represented as the summation of those four entropies as following,

$$S = S_{vib} + S_{conf} + S_{mag} + S_{el} \tag{4.7}$$

Vibration entropy comes from vibrational excitation which is small displacement of atoms around their lattice sites. In finite temperature, each atom starts to vibrate due to the thermal excitation and microscopic configuration of whole system changes. It is known that there are no available theoretical tools available in the current state of the art to accurately determine the vibration entropy. Recent work [108], however,

reported that the free energy difference between each structural phase in Fe-Cr-Ni stainless steel due to the vibration entropy is relatively small. In this work, they have predicted the error that may come from the SFE as a result of excluding the vibration entropy. They started from the assumption that the vibrational free energies for fcc and dhcp lattices are same, and they approximated the vibration free energy as the difference between vibrational free energies between hcp and fcc. Then, using the high temperature expansion of the phonon entropy, for two solids with similar Debye temperature, Θ, the have derived vibration entropy as following [31]:

$$\Delta F_{vib} \approx F_{vib}^{hcp} - F_{vib}^{fcc} \approx 3k_B T \frac{\Delta\Theta}{\Theta} \tag{4.8}$$

Then, using above equation, they obtain the vibration entropy, ΔF_{vib}, as 0.75 meV/atom, which corresponds to a contribution of SFE as $\Delta SFE \approx 2mJ/m^2$. Therefore, vibration entropy is ignored to estimate total entropy in Fe-Cr-Ni stainless system.

Configuration entropy comes from the positional interchange between atoms of different type due to the thermodynamic effect. Because in paramagnetic state of $Fe - Cr - Ni$ stainless steel, we consider totally randomized alloys. In this case of totally randomized state, the configuration entropy can be approximated as only on the function of chemical composition as following [84],

$$\Delta S_{conf} = -k_B \sum_{s \in species} c_s \ln(c_s) \tag{4.9}$$

where c_s in above equation denotes the atomic concentration of element s. As we initially assumes that our system is totally randomized, the atomic concentrations of each element, Fe, Ni,and Cr, are same for all three structural phases. In other word, atomic concentration of Fe is all same in fcc, hcp and dhcp structure. Therefore, an assumption of totally randomized alloy results in exactly equal configuration entropies for all structural phases with the same chemical compositions. As SFE is represented as the difference of free energies between each structural phases as Eq. (4.5) denotes, the contribution of configuration entropy would be zero by canceling each other out in Eq. (4.5). Therefore, we can ignore the contribution of configuration entropy in estimation of SFE of our $Fe - Cr - Ni$ system.

Electronic entropy comes from the electronic excitation which are changes in the electronic structure of the metal as electrons are excited to levels higher then the Fermi level due to the thermal excitation. The density of states of system changes as the result of electronic excitation, and the occupation of a state with specific

energy is changed. This effect can be represented as smearing the Fermi distribution function depending on specific temperature. The Fermi distribution function is the probability of occupation of a state with energy at temperature, T [22, 19]. There are many ways to smear electronic distribution function other than Fermi smearing methods, and electronic structure with smearing function can be easily calculated with ab-initio DFT method by setting so-called electronic temperature. However, recent work [41] presented that the influence of the electronic entropy on the final SFE in Fe-Cr-Ni alloy is very small. Therefore, the contribution of electronic entropy has been neglected in full estimation of SFE.

In $Fe-Cr-Ni$ alloy, the most significant factor in total entropy is magnetic entropy. Magnetic entropy comes from the magnetic excitation which is fluctuation in the size or the orientation of the atomic magnetic moments. In $Fe-Cr-Ni$ alloy, the above mentioned entropy contributions to the free energy are not sufficient for a complete description of thermodynamic properties. However, for Fe-based metallic alloys with strong local magnetic moments, such as Fe-Cr-Ni stainless steel, it is obvious that an accurate determination of the free-energy contribution from magnetic excitation is crucial [91]. Currently the entropy due to magnetic excitation cannot directly be determined within DFT. There is a previous work to use the GW approximation in order to solve the many-body problem of spin excitation in electronic system [24]. In this work, they take account for the itinerant nature of magnetism and succeed in particular to simulate spectral properties such as magnon dispersion and life time. But, the free energy calculations based on this approach have not been possible yet due to the methodological and computational complexity. Alternatively, for iron and its alloys, the assumption of a localized magnetic model has been turned out to work surprisingly well. In a system of the ideal paramagnetic state, localized magnetic moments can be simplified as of the same size and completely disordered orientation. In this approximated state, the magnetic entropy can be evaluated using the mean-field approximation as following [31],

$$S_{mag} = k_B \sum_{s \in species} c_s \ln(m_s(T) + 1) \tag{4.10}$$

where $m_s(T)$ is the average local magnetic moment of element, s. The rationale behind this approximation is, in ideal paramagnetic states, the thermal excitation of long-range order (LSO) , which is the position and the type of atoms in the entire lattice, has vanished. But, the thermal excitation of short-range order (SRO), which

is the local tendency for preference of like or unlike neighbor pairs in atomic interaction, might exist. Therefore, in a paramagnetic state, only the atomic SRO exists in finite temperature where the atomic LRO has already vanished. Based on the paramagnetic assumption, using above equation (Equ. (4.10)), the magnetic entropy is typically obtained using a two step procedure. In a first step, the interaction of the localized magnetic moments is captured by a magnetic model Hamiltonian, the parameters of which are determined by DFT calculations. In a second step, the magnetic Hamiltonian is solved in order to derive the desired thermodynamic potentials using Monte-Carlo method.

4.2.4 Magnetic Hamiltonian: LSF model

Our scheme is based on the use of the disordered local moment (DLM) approach which approximates the paramagnetic state as an uncorrelated ensemble which has the zero spin-spin correlation function. The paramagnetic DLM state includes both transverse and longitudinal spin fluctuation. Transverse spin fluctuations is the fluctuations in the orientation of the magnetic moment. Longitudinal spin fluctuation is the fluctuations in the size of the magnetic moment. In longitudinal spin fluctuation(LSF) model, we assume that the transverse spin fluctuation always follow the completely disordered configuration (,i.e: Fixed orientation of magnetic moment as completely random picture), and only longitudinal spin fluctuation occurs (, i.e: Fluctuating the size of magnetic moment).

In our software, we used more simplified LSF model, which is single-site LSF. As there is no spin-spin correlation function in DLM state, we assume there is only single atom, and the free energy is dominated by single-site magnetic fluctuations in the paramagnetic DLM site. In other words, for the 64 atom system, our Monte-Carlo calculates the magnetic moment for one atom at a time, and totally 64 runs of Monte Carlo are performed to complete whole system.

Here is the LSF magnetic Hamiltonian of a system consist of identical atom,

$$H_{mag} = \sum_i J^{(0)}(< M >) + \sum_i J^{(1)}(< M >, M_i) + \sum_{ij} J^{(2)}_{ij}(< M >, M_i, M_j) M_i \cdot M_j \tag{4.11}$$

The vector M_i is the local spin moment of an atom at site i, and magnitude of M_i can have any positive value. $< M >$ is the average value of the local magnetic moments in the system. $J^{(0)}(< M >)$ is the zeroth order term defined as the energy

of homogeneous DLM state representing a system of randomly oriented spin with a fixed value of the magnetic moments $< M >$. $J^{(1)}(< M >, M_i)$ is the on-site term, the LSF energy, which is the energy required to change the size of the magnetic moment of the atom in position i, from the corresponding DLM value $< M >$ to M_i. $J_{ij}^{(2)}(< M >, M_i, M_j)$ is the pair exchange interaction parameter, which describes the magnetic interaction between atoms at site i and j, with local magnetic moment M_i and M_j embedded in the DLM effective medium.

However, as we assume that the free energy is dominated only by single-site fluctuation, $i = j = 1$. Thus, the third-term drop to zero. Also, as there is only one site and only one element in system, the average value of the local magnetic moment in system $< M >$ is equal to $M_i = M_1$. Thus, the second term will be $J^{(1)}(< M >, M_1) = J^{(1)}(M_1, M_1) = 0$, which drop to zero as well. In other word, we don't need to consider energy required to excite $i-th$ site moment, $< M_i >$ from LSM state $< M >$ because it will be already considered in first term. Thus our Hamiltonian include only the first term of (4.11). Now, we can simplify the Hamiltonian as,

$$H_{mag} = J^{(0)}(< M >) = J^{(0)}(M_1) \tag{4.12}$$

As we only have single term in our magnetic Hamiltonian and only one element in our system, let's delete the superscript of J and the subscript of M. Also, let's change M to m because M is misguiding as total magnetization as common notation. Then, we have approximated form of simplified magnetic Hamiltonian for single atom binary system.

$$H_{mag} = J(m) \tag{4.13}$$

This equation can be applied independently and separately for the species in the alloy (For example, s = Fe, Cr, and Ni in Fe-Cr-Ni system). Note that this Hamiltonian only allow us to run Monte Carlo one atom at a time. M is the magnitude of magnetic moments of element. $J(m)$ is the energy required to excite the moment from 0 to the value m in the DLM paramagnetic state.

4.3 Computational Method

For austenitic Fe-Ni-Cr stainless steels, we assumed a localized magnetic model which works well. In particular, longitudinal spin fluctuation (LSF) model has been applied for paramagentic state. Based on this assumption, a evaluation of the magnetic

entropy is typically obtained using two step procedure. In a first step, the interaction of the localized magnetic moment is captured by a magnetic model Hamiltonian, the parameters of which are determined by DFT calculation. In a second step, the magnetic Hamiltonian is solved in order to the desired thermodynamic potential. Assuming LSF model, the first step is the procedure to obtain $J(m)$ term in Equ (4.13) using DFT calculation. The second step is the procedure to obtain magnetic moment of element in specific temperature using Equ (4.13) as potential and simulate thermal fluctuation of magnetic moment spin using Monte-Carlo simulation based on LSF model.

4.3.1 DFT for obtaining $J(m)$

In Fe-Cr-Ni alloy, we assume LSF model. As the first step, we have started assessing the impact of temperature on the magnetic moments of Fe, Cr and Ni atom. We assume the dominant single-site magnetic fluctuations in the paramagnetic state can be captured by a magnetic Hamiltonian describing local spin fluctuation(LSF) that is the sum of energies needed to excite the magnetic moment of each atom, which is $J(m)$ in (4.13). In order to capture the paramagentic state in all system, we need to estimate every $J^i(m)$ for all sites i as each site of atom has different $J(m)$. In other word, we have to obtain different $J^i(m)$ separately for $i = 1, 2, ...$,number of sites. This is because the Monte Carlo simulation computes temperature dependent magnetic moment one atom at a time using equation (4.13).

$J^{(i)}(m)$ for $i - th$ sites in system can be obtained from DFT calculation with constrained magnetic moment. Within VASP, we approximate the sum of energies needed to excite the magnetic moment of each atom from total energy calculations obtained by constraining the magnetic moment of a particular atom to the desired excited value, while fixing the magnetic moments on the other atoms to their ground-state values obtained at zero temperature. Here are brief technical details of how we obtained all $J^{(i)}(m)$ in 64-atomic Fe-Cr-Ni alloy using VASP.

1. **Generate structure**

   First step is the generation of structure of stainless steel. We have generated special quasi-random structure of a given chemical composition of stainless steels using random mixing. Specifically, we have used a Monte-Carlo based annealing loop to seek the structure with minimum energy, so-called quasi-random

structure method. In that way, statistically random configuration is obtained. This is the preferred literature method for generating disordered crystalline or solid alloy.

2. **Relax structure**

   Second step is relaxing volume and atomic position and get the optimized structure. Starting from the quasi-random structure, we have performed a geometry optimization using density functional theory. In particular, the BFGS structural optimization scheme has been used to find the unit cell with minimum energy. In our optimization, the lattice parameters (volume of unit-cell) are being fixed to the experimental value of A316-Fe-Cr-Ni stainless steel. From our DFT results, It has been showed that there is no significant difference in energy per atom and volume as increasing system size from 64, 212 and 300 atoms. Therefore, rather than try to use large system, we perform calculations on a smaller system, which is a 64-atom system.

3. **Ground state calculation of paramagnetic state**

   From optimized structure, we have obtained paramagnetic configuration of snapshot of magnetic moments in Ground states. Within VASP, this can be achieved by constraining total sum of all magnetic moments as zero by setting NUPDOWN = 0 in INCAR. We turned on spin-orbit coupling parameter (LSORBIT = TRUE) and let all magnetic moment spins relaxed including orientation and direction by setting the weight factor of penalty term to change magnetic moments as zero (LAMBDA = ZERO). After SCF calculations, we got the ground state magnetic moment configuration of paramagnetic state of system from output, **OSZICAR**. Therefore, for the case of 64 atom Fe-Cr-Ni system, we got 64 Cartesian vectors as paramagnetic snapshot of spins in ground state (zero temperature) for all sites.

4. **Obtain $J^{(i)}(m)$ from all $i-th$ site**

   Once we obtain paramagnetic spin configuration in ground state for our Fe-Cr-Ni alloy from step 2, we can give the system small perturbation from magnetic moments in ground state. If we fix all moments as ground state, and only change the magnitude of moment on $i-th$ site as m, the energy required to excite magnetic moment on $i-th$ site can be obtained by the difference of total energy between ground state and perturbed state. In this way, $J^{(i)}(m)$ obtained

as the difference of total energy between ground state and perturbed state which have only the magnitude of magnetic moment on $i-th$ site with excited value while others are fixed as ground state. For example, in case of 64 atomic system, we obtained spin snapshot of ground state of 64 atoms in step2 such as, $(x_1, y_1, z_1), (x_2, y_2, z_2), (x_3, y_3, z_3)...(x_i, y_i, z_i)..(x_{64}, y_{64}, z_{64})$. Then, we can give perturbation only on $i-th$ atom by changing only (x_i, y_i, z_i) accordingly. As we are dealing with LSF model which fix all orientation of spins as paramagnetic ground state, and only change magnitude, we only give the perturbation to the magnitude of spin. Let's consider we only change the magnitude of $i-th$ spin, $\sqrt{x_i^2 + y_i^2 + z_i^2}$, to certain value $|m_i^{(1)}|$ while fixing other 63 spins as same as paramagnetic ground state. Then, let's call this configuration as perturbed spin snapshot. Then, from this single total energy calculation of perturbed spin snapshot, we can obtain one point of $(m, J^i(m))$ on $J^{(i)}(m)$ curve from the difference between total energy of ground state and total from energy of perturbed state, such as

$$J^{(i)}(m_i = m_i^{(1)}) = total\_energy(perturbed\ state) - total\_energy(ground\ state). \tag{4.14}$$

Likewise, by calculating total energy of system as stretching the magnitude on $i-th$ magnetic moment spin, from 0 to maximum value, we can get multiple data points to construct $J^{(i)}(m)$.

Again, magnetic moment of all sites can be constrained by setting M_CONSTR parameter in **INCAR**. We can obtain the snapshot of ground state for spins from previous step. The maximum value of the magnitude of spin to stretch has been decided as the experimental magnetic moment of species. All procedures above using DFT have been automated in our case by in-house python program.

5. **Fit $J^{(i)}(m)$ curve using fifth order polynomial**

   After obtaining all points of total energy for different magnitudes of m, we fit $J^{(i)}(m)$ curve using least squares regression method to 5-th order polynomial function.

   By iterating Step 3 and Step 4 for all sites of system, we obtain $J^{(i)}(m)$ curve for every site in system. Below Figure (4.3) represents schematic description of step 3 and 4.

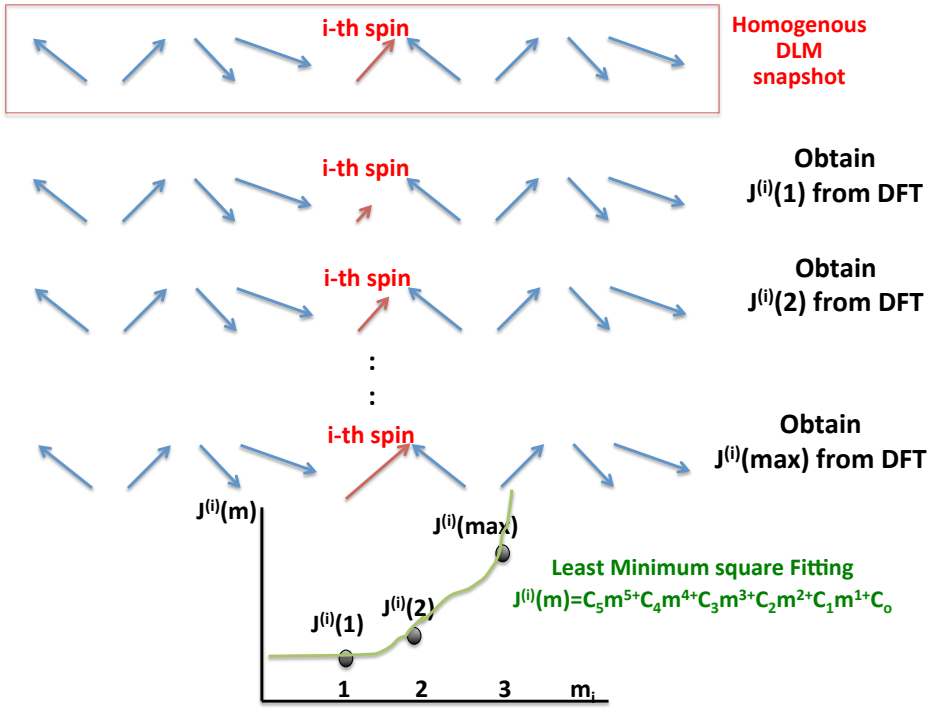

Figure 4.3: Obtaining $J^{(i)}(m)$ from constrained magnetic moment DFT calculation

4.3.2 Monte-Carlo simulation

In order to calculate the magnitude of magnetic moment at specific temperature, the classical Metropolis Monte-Carlo simulation is used. Monte Carlo simulations use random moves to explore the search space to find out some information about the space. The Metropolis algorithm starts with a random state of the system. Then, on the basis of the current state, a random new state is generated and proposed as a follow-up of the current state. This proposed state is accepted with a certain probability. The acceptance criterion is such that the relative importance of the current and proposed states estimated by the Boltzmann probability. The proposed state is unconditionally accepted if it is more probable and it is conditionally accepted, relative to importance of the current state, if it is less important (also estimated by Boltzmann probability). So, the proposed or the old state will be used as the new state of the system. For austenitic Fe-Cr-Ni Stainless steels, we have used LSF model to determine total energy of state, and the description of detailed algorithmic framework is following in next section - Material Design Framework for Fe-Cr-Ni stainless steels.

4.4 Material Design Framework for Fe-Cr-Ni system

As mentioned above, our main goal is the computational discovery of austenitic Fe-Cr-Ni stainless steels with low-Ni content (and thus low cost) to be used in balance of plant components that are compatible for commercial fuel cell electric vehicle. To achieve this goal from a computational perspective, we have developed a material design framework which combines sophisticated optimization and uncertainty quantification combining with ab-initio DFT calculation and Monte-Carlo calculation based on LSF model as described above. In particular, the developed modeling subroutine is predicting magnetic contribution of stacking fault energy in finite temperature for austenitic stainless steel system. By developing in-house computational material design framework, we have created the database and material design relations that identify stainless steel alloy that optimize stacking fault energy with reduced Ni content. Here is brief description about in-house material design framework which have been developed for austenitic Fe-Cr-Ni stainless steels in specific.

4.4.1 Inputs

In our software framework, we accept two inputs as following,

- $J^{(i)}(m)$ **for all sites:** The polynomial fitting function of free energy by magnitude of magnetic moment for $i-th$ site and species s should be given to the program previously. The text file named **coeff.txt** is the input file contains all parameters of polynomial fit functions of all atoms and all species. In order to obtain $J(m)$ fit function, first principle calculation with density functional theory has been used. Basically, the total free energy has been calculated using DFT with different constrained magnetic moment, and from the data of free energy for different constraint magnetic moment, the fifth order polynomial function has been obtained by least square fitting method.

- M_{max} : When we pick the random magnitude of magnetic moment, we use the uniform sampling between 0 to maximum possible value of magnetic moment of specific species. The maximum possible value of moment of specific species, M_{max} is asked to user at the beginning of program and user should give the value to the program as the input. Usually, experimental magnetic moment of the species is the good estimation for M_{max}.

4.4.2 Algorithmic Steps

In our simplified single-site LSF model, a system of each Monte-Carlo simulation only have single atom. Thus, the target single atom started from random magnitude between 0 to maximum possible value, and progressively altered by changing the size of magnetic moment in a random manner and deciding whether or not it accept the random movement by Boltzmann probability.

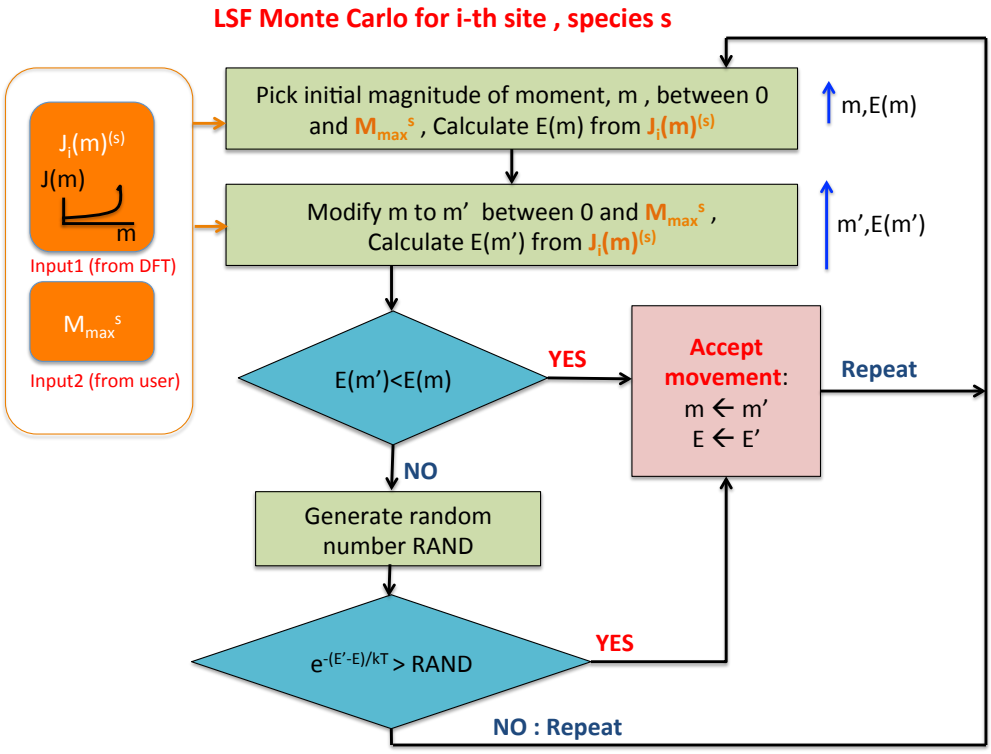

Figure 4.4: Flowchart of our LSF based Monte-Carlo software.

The flowchart in Figure 1 shows details of Monte-Carlo algorithm in our software. We perform Monte-Carlo simulation for each different site and each different species separately and in independent manner. For example, if the target system has 5 atoms with 2 Fe - 2 Cr - 1 Ni, we performs 5 independent monte-carlo simulations which include all (i-th site, s-species) such as (1,Fe), (2,Fe), (3,Cr), (4,Cr) ,(5,Ni). Given flowchart in Figure 1 represents general case of i-th site and for the species, s.

Here are the brief descriptions of each step in our LSF based Monte-Carlo simulation.

1. Obtain $J(m)$ from the input file, **coeff.txt** and obtain M_{max} from user.

2. Pick the magnitude of magnetic moment, m, by random sampling between 0 to M_{max}.

3. For the picked value m, calculate energy of m, $E(m)$, from $J(m)$ function.

4. Modify m to m' by random sampling between 0 to M_{max}.

5. For the modified value m', calculate energy of m', $E(m')$, from $J(m)$ function.

6. Compare $E(m')$ and $E(m)$. If modified moment, m', has lower energy than before, accept the change to m', and save to m_i. If modified moment, m', increase the energy, accept the change to m' only when random number between 0 and 1, $RAND$, is lower than Boltzmann probability, $e^{-\frac{E'-E}{k_B T}}$.

4.4.3 Output

As the output file, our program generates text file named **LSF_MC.data** which contains magnitudes of magnetic moment at finite temperature for every target atoms ($i.e: J^{(i)}(m)$ for all sites that have been given in **coeff.txt** file.)

4.5 Results

4.5.1 Ab-initio molecular dynamic calculation

In order to understand the effect of magnetic spin configuration and entropy in austenitic Fe-Cr-Ni stainless steel system, we have performed the ab initio molecular dynamic simulation. The ab-initio molecular dynamic simulation presented here was carried out on a 64-atom system (fcc; $Fe_{66}Ni_{17}Cr_{17}$) at the DFT/PBE level of theory using 2 fs time steps. Based on previous results, a 64-atom system is relatively invariant to alloy configuration. The ab-initio molecular dynamic simulations were performed at 300K and the total energy and net magnetic moment have been plotted as a function of time in Figure 4.5.

The results hint at the paramagnetic nature of the material, as the total energy/atom (red curve in Figure 4.5) is at or close to a minima with both positive (e.g. at 375 fs) and negative (e.g. at 900 fs) total net magnetic moments. If the simulation was carried out for a longer period of time the average net magnetic moment would go to zero, as oppose to the current median value of -4.3 μ_B. Further insights into the spin

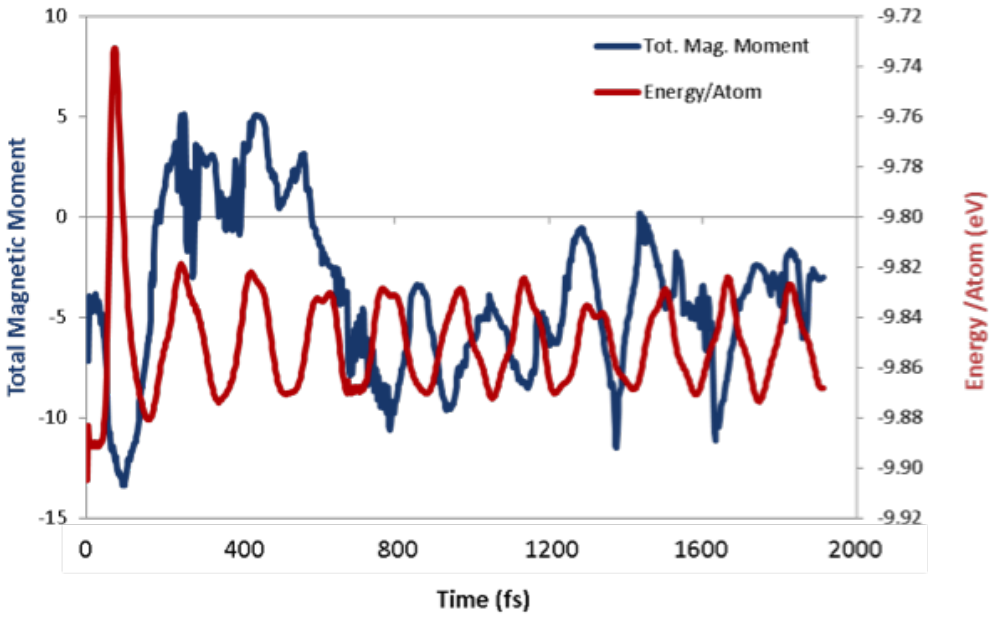

Figure 4.5: Total magnetic moment (left axis) and total energy per atom (right axis) as a function of time (fs) in ($Fe_{66}Cr_{17}Ni_{17}$) alloy.

fluctuations at room temperature (300K) have been gained by plotting the magnetic moment of the individual atoms during the ab-initio molecular dynamic simulation, shown in Figure 4.6. Visually, this data seems to capture the paramagnetic nature of the material. The average magnetic moment appears to be zero for each element type. The observed non-zero net magnetic moment (-4.3 μ_B) seems to be because of an imbalance of atomic spin at a specific or short interval of time. It is believed that with a much larger unit cell or longer simulation time, the net magnetic moment would approach zero. The results provide two important insights of the system. Firstly, the spin fluctuations at room temperature suggests the paramagnetic state of alloy. Secondly, significant spin fluctuations also suggest that we cannot ignore effect of magnetic entropy in evaluation of stacking fault energy. The entropy, including magnetic spin fluctuations, at 300K is shown to be 50 meV per atom (the first 300 time steps were neglected to allow the system to equilibrate).

4.5.2 Size and alloy configuration dependence on DFT

Using a method to calculate a crystal's stacking fault energy (SFE) from a combination of cohesive energies for the face-centered cubic (fcc), hexagonal close-packed

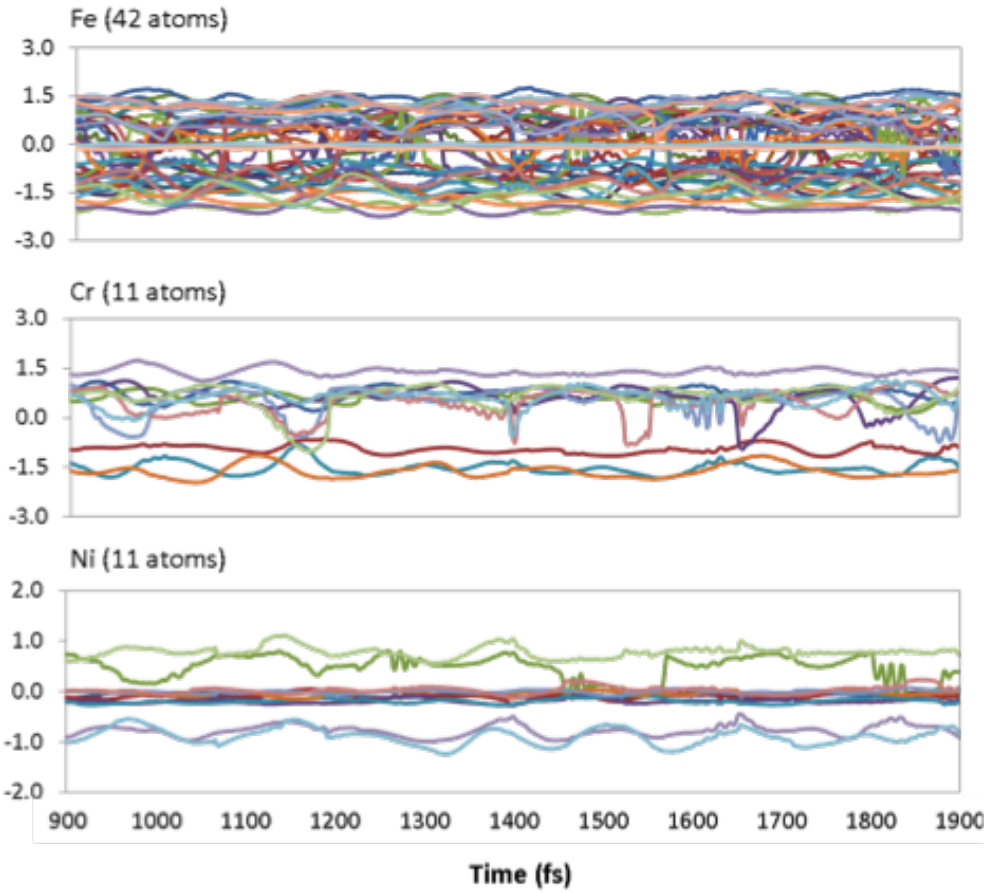

Figure 4.6: Magnetic moment of the individual atoms in the 64 atom unit cell as a function of time (fs): top âĂŞ Fe atoms; middle âĂŞ Cr atoms; bottom âĂŞ Ni atoms in ($Fe_{66}Cr_{17}Ni_{17}$) alloy.

(hcp) and double hcp (dhcp) structures, we have investigated the size dependence of alloy configuration by creating randomly oriented systems of the different molecular size such as 64, 212 and 300 atoms, and same chemical composition (same weight percent of Fe, Cr and Ni). Our DFT results, based on a molecular systems composed of 64, 212 and 300 atoms, showed virtually no variability in energy per atom and volume. This result prompted us to perform calculations on a smaller system, Therefore, 64-atom system, the smallest system in testing bed, has been investigated to reduce computational cost. The results from a 64-atom system are shown in Fig. 4.7.

The energy-volume curves demonstrate that a relatively small system can be used without encountering variability due to alloy configuration. Moreover, the effect of the initial spin state of the atoms was also included by generating a random initial spin state (up or down) for each atom. It is worth to note that the total magnetic

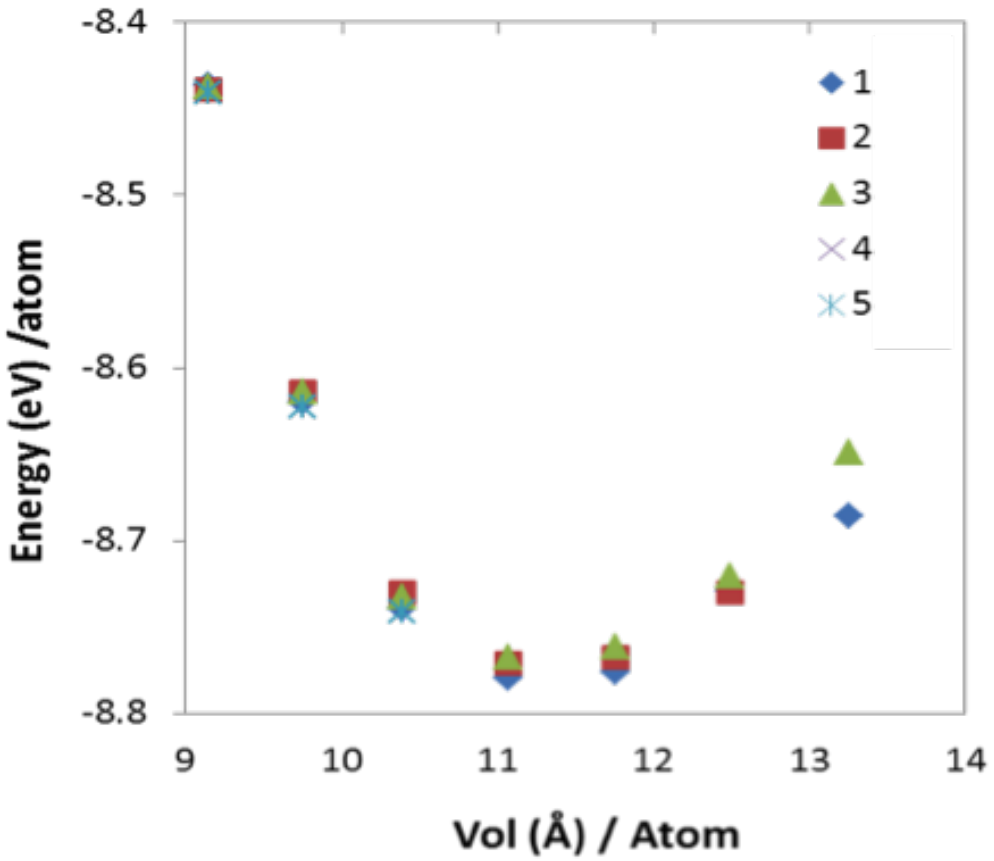

Figure 4.7: Volume vs. energy per atom for 5 randomly generated austenitic stainless steel alloys ($Fe_{42}Cr_9Ni_{13}$) composed of 64 atoms.

moment of the system was constrained to zero since austenitic Stainless Steel is well known to be paramagnetic. The ability to be able to model a relatively small system is of tremendous potential for two reasons: Firstly, the computational time is greatly reduced enabling other alloying elements and compositions to be screened. Secondly, higher level calculations, such as hybrid density functionals, and consideration of temperature effects can be enabled.

4.5.3 Dependence of DFT-functional on SFE

We have performed calculations utilizing several different density functionals in order to gain insight into the complexity of predicting the SFE, see Table 1. Although a few functionals predict reasonable values of SFE consistent with results known from the literature, most of the DFT functionals predict a negative SFE at zero temperature. This result may indicate instability of the different crystal phases (e.g. fcc) at low

	FCC		HCP		dHCP		SFE
	E/atom	V/atom	E/atom	V/atom	E/atom	V/atom	(mJ/m^2)
PBE	-9.11	10.80	-9.12	10.63	-9.10	10.68	-21
PBEsol	-9.84	10.08	-9.86	10.07	-9.85	10.12	-152
PBE+U	-5.54	14.00	-5.55	13.82	-5.50	13.66	167
PW91	-7.72	10.81	-7.74	10.67	-7.73	10.73	-131
LDA	-10.25	9.78	-10.25	9.76	-10.24	9.78	36
AM05	-9.54	10.09	-9.59	10.00	-9.58	10.04	-388

Table 4.1: The energy/atom, volume/atom and predicted stacking fault energy (SFE) of a austenitic stainless steel alloy ($Fe_{42}Cr_9Ni_{13}$) using different density functionals. The results are based on a model system composed of 64 atoms; energies (E) are in units of eV and volumes (V) are in units of (ang^3).

temperature, and emphasizes the importance of including aspects relevant at higher temperatures, such as thermal expansion of the lattice and inclusion of vibration and magnetic entropy. Although the result from LDA showed the closest agreement with experimental SFE and the results from recent literature [108, 109], we choose PBE functional for our calculation due to its small variability due to alloy configuration than LDA.

4.5.4 $J^{(i)}(m)$

Using the procedure described in above section, we have obtained LSF energy, $J^{(i)}(m)$, in magnetic Hamiltonian (Equ (4.13)), for 64-atomic Fe-Cr-Ni stainless steels.

Figure 4.8 shows the calculated LSF energy for a certain Fe, Cr and Ni atom in a 64-atom super cell of the alloy in the fcc structure. The minimum value of the excitation energy, $J^{(i)}(m)$, is realized for the zero temperature ground state magnetic moments. One can see that it is energetically costly to excite the magnetic moment of a Ni atom. The magnetic moment on Ni atoms can exist only as a thermal excitation. While at zero temperature, a finite magnetic moment can exist on Cr sites. it is Fe atoms that have the highest magnetic moments. Also, it is apparent that thermal excitations are the most favorable for Fe atoms. As we do not rely on the coherent potential approximation (CPA) approach, each of the atom sites shows a different LSF behavior. Figure 4.7 (b) shows such differences for two different Fe atoms in the 64-atom fcc super-cell. We can observe light differences between two sites of Fe atom.

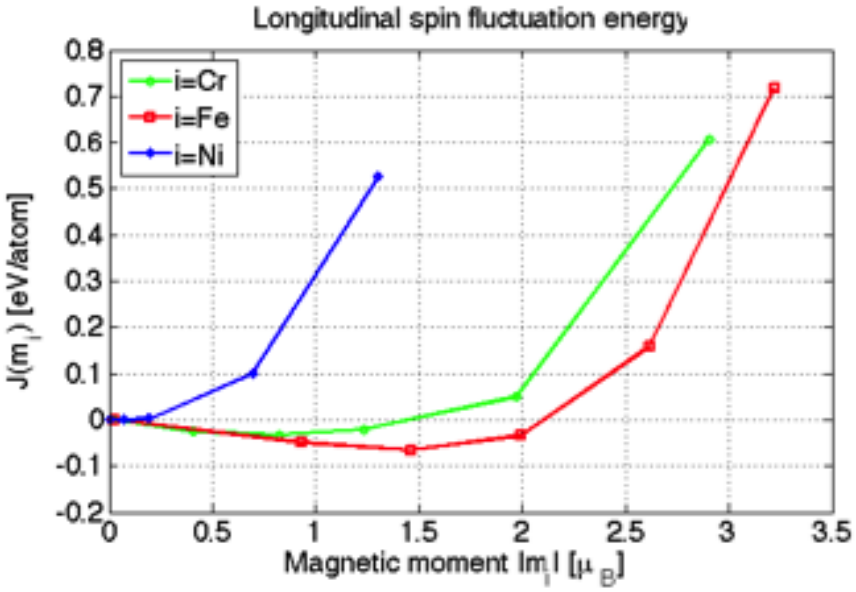

(a)

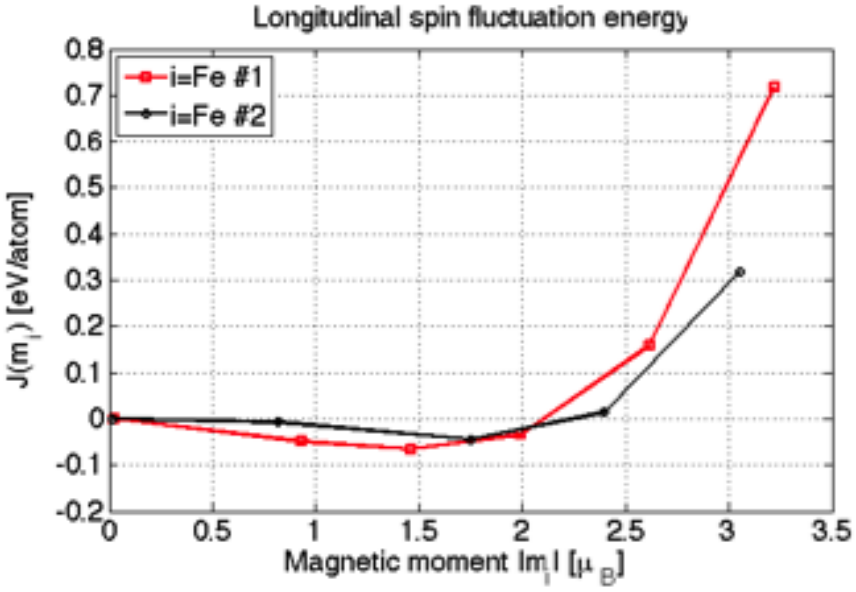

(b)

Figure 4.8: Energies needed to excite the magnetic moment of select atom in ($Fe_{42}Cr_9Ni_{13}$) composed of 64 atoms. (a) variations between Fe, Cr and Ni atoms (b) variations between Fe atoms at two different sites within an fcc lattice

4.5.5 Stacking Fault Energy

Our approach estimates SFE from a combination of cohesive free energies for the face-centered cubic (fcc), hexagonal close-packed (hcp) and double hcp (dhcp) crystal structures. These free energies depend not only on the volume and arrangement of atoms within the lattice (the enthalpy contribution to free energy), but also on the temperature and the average magnetic moment of the constituent atoms at that temperature (the entropy contribution). Therefore, we calculate (1) the enthalpy contribution to SFE, and (2) the magnetic entropy contribution to SFE, then sum those two terms to obtain full stacking fault energy in alloy. Our current computational procedure for predicting SFE involves two steps.

1. Calculating SFE from enthalpy term:

   From the quasi-random structure of alloy, we determine the enthalpy. Specifically, the enthalpy for each dhcp, hcp and fcc structural phase is calculated using the VASP density functional theory code, the magnetic moments that minimize this enthalpy at zero temperature, and the volume of the fcc crystal at the desired temperature as determined in experiments. Then, SFE is calculated by the difference of enthalpy between each structural phase using Equ. 4.5.

2. Calculation magnetic contribution of SFE:

   Use longitudinal spin-fluctuation (LSF) Monte Carlo to determine the magnetic/spin entropy. This requires performing a series of separate DFT calculations for each atom in the system with a linear perturbation to the magnetic moment. This allows for the determination of the enthalpy as a function of magnetic moment. These data are used as input for the LSF Monte Carlo calculations to determine the magnetic/spin entropy at a finite temperature by Equ. 4.10. Then, the magnetic contribution of SFE is evaluated by the difference of magnetic entropy between each structural phase using Equ. 4.5. We compute the magnetic entropy by doing a combination of VASP and Monte Carlo calculations to determine the average magnetic moment of each atom in the system at a given temperature.

This procedure is repeated for three crystallographic phases (face-centered cubic (fcc), hexagonal close-packed (hcp) and double hcp (dhcp)) to determine the SFE of a given

alloy composition. The computational expense associated with this approach is quite considerable. For a typical geometry optimization of a given crystallographic phase and alloy composition, 384 processors (24 compute nodes x 16 processors) are used with an average runtime of 48 hours. For the estimation of magnetic/spin entropy of a 64-atom system, 552 single-point DFT calculations are performed, each requiring 128 processors (16 compute nodes x 8 processors). Thus, a total of 70,656 processors are used for approximately 8 hours just to obtain the magnetic/spin contribution to the SFE.

4.5.5.1 Results from Monte-Carlo

Figure 4.9 shows these average moments for all atoms in a 64-atom system. We then repeat this calculation at various temperatures to quantify the dependency of average magnetic moment on temperature (as shown in Figure 4.10). Using these average magnetic moments within the analytic expression of magnetic entropy,

$$S_{mag} = k_B \sum_{s \in species} c_s \ln(m_s(T) + 1) \tag{4.15}$$

enables us to quantify the magnetic entropy and - when combined with the enthalpy - the free energy for the specific crystal structure being modeled. We have fully developed our approach and applied it to 64 atomic Fe-Cr-Ni stainless steels system, $Fe_{43}Cr_9Ni_{13}$.

In Figure 4.11, the average magnetic/spin moments, obtained from a LSF Monte Carlo simulation, for the individual atoms in a 64-atom system ($Fe_{66}Cr_{14}Ni_{20}$) are shown. This figure illustrates how the magnetic/spin moments are distributed among a range of values. This distribution is believed to be due to an atom's local chemical environment. The data also indicates that atoms in the FCC structure have a larger magnetic/spin moment on average than the DHCP or HCP phases. This leads to a positive contribution to the stacking fault energy. We estimate the magnetic entropy to be 10.5 mJ/m^2 at 300K. This value is in agreement with published results by Vitos [109] for a similar system.

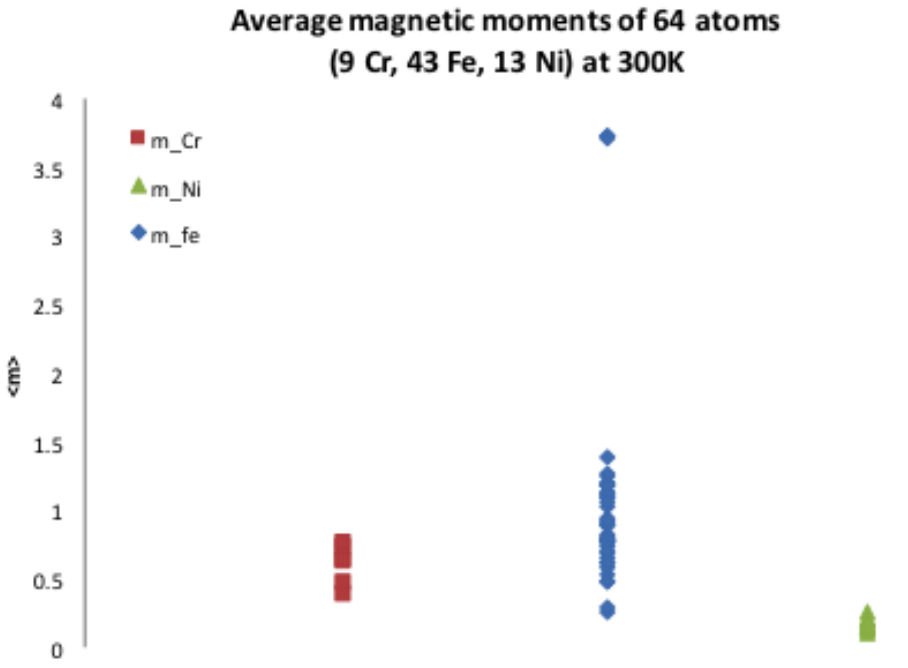

Figure 4.9: Average magnetic moments, $< m_s^i >$ of all atoms within a 64-atom system at a temperature of 300K in $Fe_{43}Cr_9Ni_{13}$ system

4.5.5.2 Magnetic contribution in SFE

In Figure 4.12, the magnetic/spin entropy contribution to the SFE as a function of temperature is shown. This indicates that with increasing temperature the magnetic/spin entropy increases, due to increased magnetic fluctuation, which will ultimately increase the SFE.

4.6 Discussion

Using thorough computational approach combining DFT and Monte-Carlo simulation based on LSF model, the magnetic contribution term of SFE due to the spin fluctuation is successfully evaluated. In this new computational modeling routine, we have successfully calculated and quantified the temperature dependent magnetic/spin entropy for a 64-atom system.

Our results are in agreement with what has been reported in previous literature. It is worth to note that, however, on the process of evaluating magnetic contribution

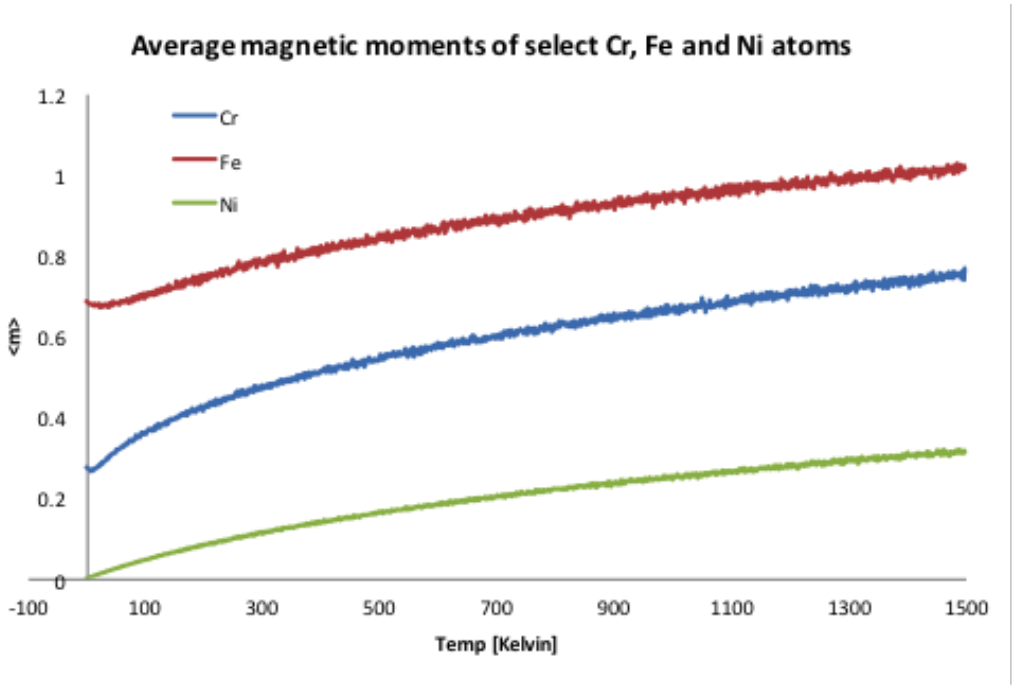

Figure 4.10: Average magnetic moments of select Cr, Fe and Ni atoms (3 of the 64-atom system, $Fe_{43}Cr_9Ni_{13}$) as a function of system temperature

of SFE, We have identified two key issues that make accurately predicting the enthalpy contribution to the SFE requires large effort of free energy calculation with high precision. The issues arise due to (1) thermal expansion and (2) electronic spin configuration. One of the difficulties with accurately determining the enthalpy is related to thermal expansion. In general, DFT calculations are performed at 0K. Therefore, the DFT optimal lattice parameter should theoretically be less than the experimental value at room temperature (300K). Initially, we sought to determine the DFT optimal lattice parameters for the different alloy compositions in order to incorporate volume effects (material density) due to alloy composition. We thought that this effect could be more important than thermal expansion at room temperature. However, this assumption led to the prediction of relatively large negative SFEs (-100 mJ/m2), even for Ni-rich alloys in contradiction to experiment. We concluded that at 0K the FCC phase is not the lowest energy structure but at room temperature the FCC phase stabilizes. This is schematically shown in Figure 4.13 . As mentioned, in order to achieve a positive SFE, consistent with experimental, the FCC phase must be lower in energy than at least one of the other two phases. It should be mentioned, that the transition point between positive and negative SFE is very sensitive to lattice parameter, further complicating the calculations. This result

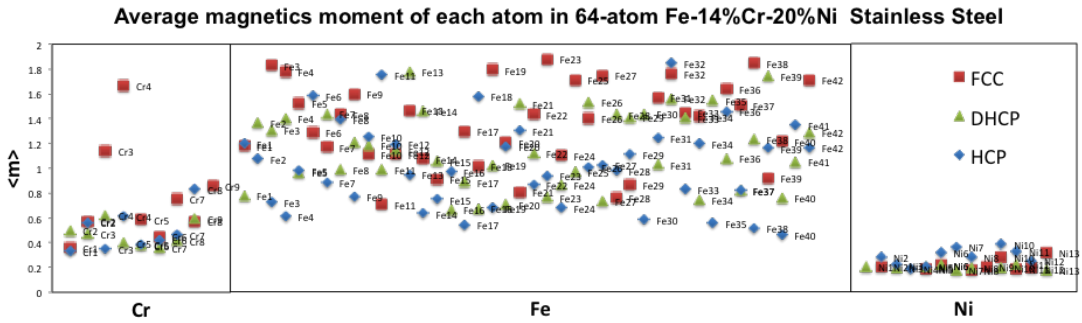

Figure 4.11: Comparison of average magnetic moments of all atoms within a 64-atom system between different structural phases- FCC, DHCP and HCP- at a temperature of 300K in $Fe_{66}Cr_{14}Ni_{20}$.

led us to perform calculations using the experimental lattice constant of 316 stainless steels. (Theoretically, DFT can be used to predict thermal expansion, however, doing so is impractical for the size (number of atoms) of systems needed to represent the random alloys.) In doing so we were able to achieve a positive SFE, 25.9 mJ/m^2, for a Ni rich alloy ($Fe_{67}Cr_{13}Ni_{20}$). Incorporating the magnetic/spin contribution, results in a SFE value of 36.4 mJ/m^2 which is in good agreement with experiment and published results by Vitos [109, 110, 108]. Upon performing calculations on other alloy compositions, we identified a second issue with accurately predicting the enthalpy contribution. This second issue with determining the enthalpy contribution to the SFE has to do with the electronic spin configuration. When performing a spin-polarized DFT calculation, one has the ability to guess at the initial spin configuration of the atoms (e.g. +3, 0, -3). In most materials (i.e. metals, metal oxides, organics), this is not much of an issue; however, Stainless Steel has a very complicated electronic structure due to structural disorder and the paramagnetic nature of the material. As a result, we have found that depending on the initial electronic spin configuration (initial guess), drastically different SFEs can result. For example, for the same alloy composition ($Fe_{67}Cr_{13}Ni_{20}$) and structural configuration we have achieve SFEs (based on enthalpy) as high as 150 mJ/m^2 and as low as -132 mJ/m^2. Typically, one would use the electronic configuration that has the lowest total energy. In this case, that would correspond to a predicted SFE energy of 150 mJ/m^2; however, experimentally we know that this value is too large. Moreover, this system has a ferromagnetic electronic configuration, not paramagnetic. The value of -132 mJ/m^2 does correspond to a paramagnetic electronic configuration, as does the value of 25.9 mJ/m^2 previously mentioned. To insure that we have identified the lowest energy

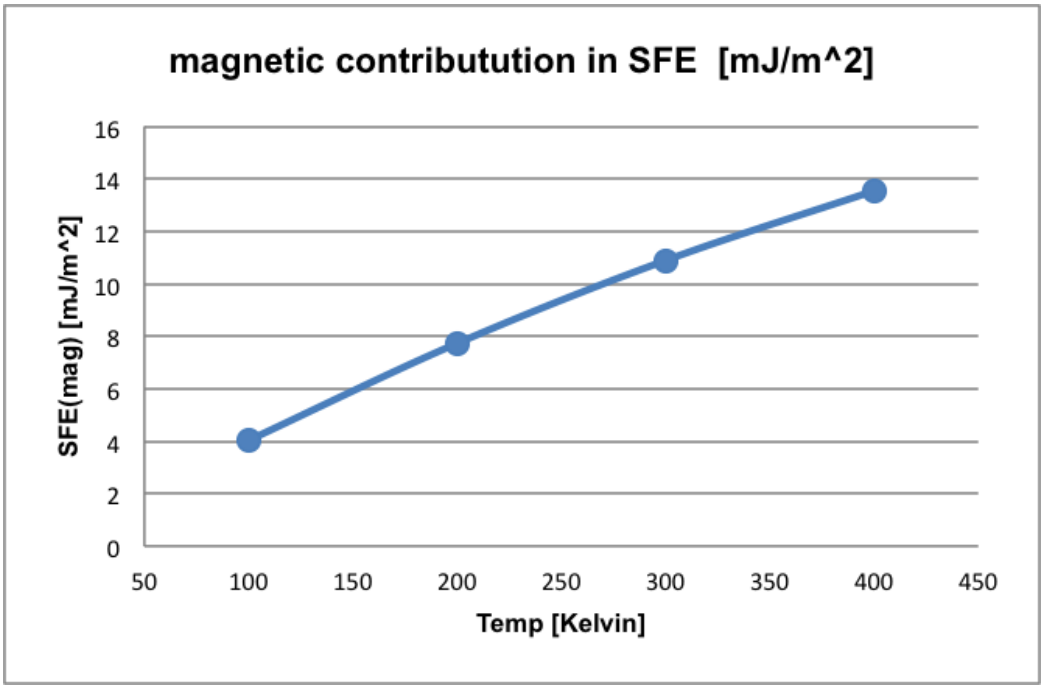

Figure 4.12: Magnetic fluctuation Contribution in Stacking Fault Energy for different temperature points in $Fe_{66}Cr_{14}Ni_{20}$.

paramagnetic structure, one potential solution would be the use of larger unit cells which would increase the computational expense of the calculations.

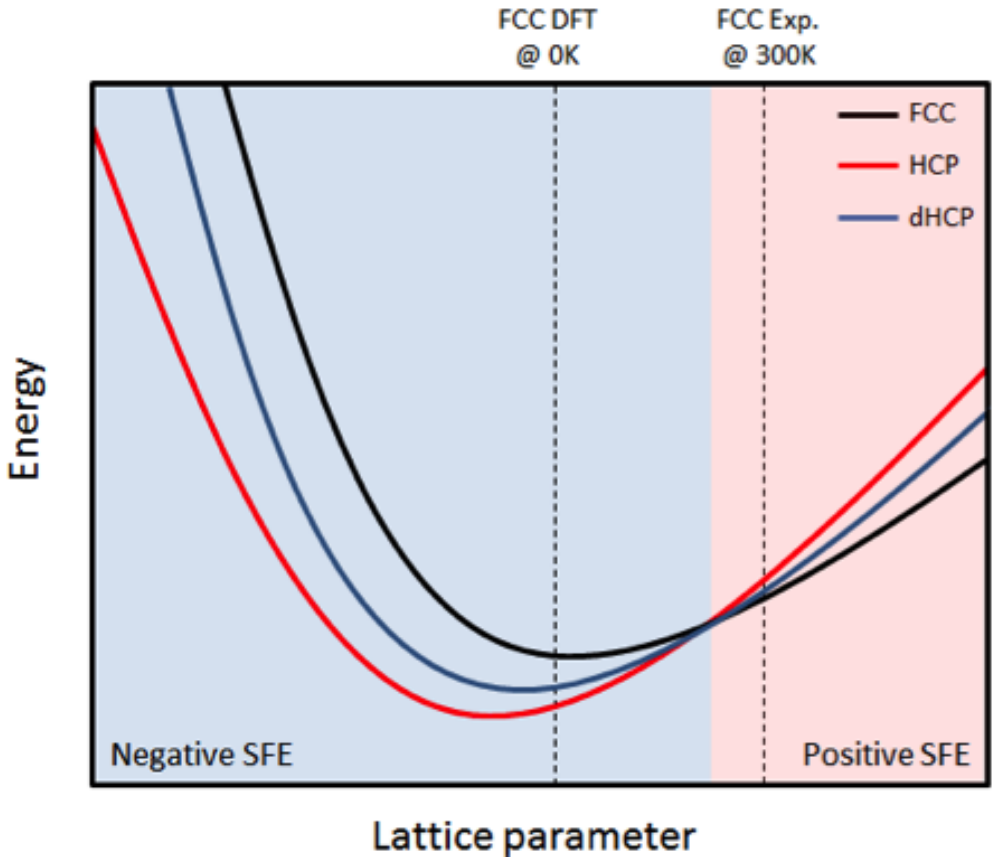

Figure 4.13: A schematic representation of the potential energy curves (energy vs. lattice parameter) for FCC, HCP and dHCP crystallographic phases.

Chapter V

GPU IMPLEMENTATION ON MONTE-CARLO SIMULATION USING ISING MODEL

5.1 Motivation

As mentioned above, DFT-based modeling of thermo-magnetic properties of material has limitation in that (1) It is ground state calculation, and (2) the important statistical effect in finite temperature, such as magnetic spin fluctuation, in magnetic material is not fully considered in calculation. Therefore, as the alternative modeling method, the combination modeling routing with DFT and Monte-Carlo simulation is approached. In Chapter 3, the Heisenberg Monte-Carlo simulation based on KKR-CPA calculation combined with DFT and it predicts quite accurate Currie temperatures of $(Fe_{1-x}Co_x)_2B$ which is almost same with experimental values. In Chapter 4, the LSF Monte-Carlo simulation predicts the magnetic entropy of austenitic Fe-Cr-Ni stainless steels, so the magnetic contribution to the stacking fault energy of alloy. Thus, we have validated the simulation model in terms of its functionality. However, there are large portion of area to be improved in terms of its efficiency. First issue is the speed of Monte-Carlo calculation. Monte-Carlo is generically stochastic methods for calculating the most probable state of many particle system in finite temperature. Due to its nature of stochastic method, multiple cases of state are sampled and iterate accept or reject processes. Therefore, its computationally slow and expensive process in nature. For example, in case of Heisenberg Monte-Carlo simulation introduced in Chapter 3, our Monte-Carlo software took about 13 seconds to run 1000 atomic system at one finite temperature point, which is quite slow. At current stage of our research, it was okay. Because the Monte-Carlo software package had been mainly used to calculate Currie temperature of $(Fe_{1-x}Co_x)_2B$ families. However, in order to consider this modeling software as the sub-routine of material discovery framework which is capable to mimic real physical picture of complicate material systems, the speed of this simulation would be the main drawback which will make the process unfeasible.

Second issue is the limitation of system size to be modeled. As Monte-Carlo simulation change the spin configuration one atom at a time and then calculate energy from modified snapshot of spin configuration, It takes tremendous monte-carlo step size to make the simulation converged. Also, the process to obtaining total energy of whole system become expensive in large system. For example, in Heisenberg model, in n-atomic system, we need $O(n^2)$ summation, multiplication and dot products to compute single point of total energy out of its Hamiltonian, because Heisenberg Hamiltonian principally considering all spin-pair interactions in evaluation of total energy of system. Therefore, in case of sequential Heisenberg Monte-Carlo simulation, the large material system is un-thinkable due to this polynomial computational complexity. The number of atoms of our system in Chapter 3 hasn't been exceeding 1000 atoms for every simulation. However, to mimic the real physical phenomenon as accurate as possible, the source code should be able to extend to the many-body system, such as several millions of spins, which is capable to consider defect, pinning or vacancy in atoms.

Those two limitations suggest the necessity to implement high performance feature in simulation. Therefore, to resolve those issues, we developed new software program implementing higher-fidelity features within our Monte-Carlo source code based on Ising model. Especially if larger cases or many runs are needed, a GPU implementation could be of great benefit. The program we developed supports parallelization, by taking advantage of Graphical Processing Units. The Compute Unified Device Architecture (CUDA) is a programming approach for performing scientific calculations on GPU as data-parallel computing devices. With significantly increased number of cores in conjunction with a memory bandwidth, a recent GPU offers incredible resources for scientific computing. By implementing a variant of the checkerboard algorithm, we expect to obtain faster calculation on the GPU than on a CPU core.

In this chapter, I present work on GPU implementation on Monte-Carlo simulation using simple Ising model, and performance of GPU program with parallel algorithm has been compared with CPU program with sequential algorithm for the simple bcc-Fe system.

5.2 Backgrounds

This part introduces GPU computing as parallelization and distributed simulation method that we implemented in our Monte-Carlo many particle simulation.

5.2.1 GPGPU computing

GPU stands for Graphical Processing Units which are high-performance many-core processors. [54] GPUs are peripheral devices connected to a host node, taking inputs from central processing units (CPUs), outputting images onto screens. [9] However, other than its initial purpose as the graphical processing, GPUs are also able to be used for general purpose computing. Denoting the usage of GPU in that performs non-specialized calculations that would typically be conducted by the CPU (central processing unit), the term general-purpose GPU (GPGPU) often used in high performance computing community. GPGPUs are used for tasks that were formerly the domain of high-power CPUs, such as physics calculations, encryption/decryption, scientific computations and the generation of cypto currencies. Because graphics cards are constructed for massive parallelism, they can dwarf the calculation rate of even the most powerful CPUs for many parallel processing tasks. The same shader cores that allow multiple pixels to be rendered simultaneously can similarly process multiple streams of data at the same time. GPGPU pipelines may improve efficiency on especially large data sets or data containing 2D or 3D imagery. It is used in complex graphics pipelines as well as scientific computing. Particularly in fields with large data sets like genome mapping, or where two- or three-dimensional analysis is useful - in particular at present biomolecule analysis, protein study, and other complex organic chemistry. There are many previous works reporting significant saving of computing time by a huge variety of scientific fields; GPU acceleration used in the area of astronomy [23] and radio astronomy [40]. Soft tissue simulation [103], algorithms for image registration [34], dose calculation [33], volume reconstruction from x-ray images [32], and the optimization of intensity-modulated radiation therapy plans [74] are examples for the numerous applications in medicine. Furthermore, DNA sequence alignment [104], molecular dynamics simulations [104, 4, 25], quantum chemistry [106], multipole calculations [36], density functional calculations [28, 116], air pollution modeling [76], time series analysis focused on financial markets [87, 86], and Monte Carlo simulations [117, 6, 75] benefited from GPU computing. For many

applications, the accuracy can be comparable to that of a double-precision CPU implementation. However, one challenge in optimizing GPUs for parallel computation is managing memory access patterns, which are under the control of the programmer, so as to minimize slow memory transactions as well as facilitate processor communication for calculation efficiency. In our work, the checkerboard approach is used to parallelize the Monte Carlo computation. That is, for a computation stencil where only one orthogonally adjacent data element is needed in each direction, the computation domain can be divided in a checkerboard fashion to allow for concurrent computation on each checkerboard subdivision.

5.2.2 Monte-Carlo for many-particle simulations on GPUs

Many-particle-simulation has been one of the main research areas which require high performance computation. One method to simulate many-particle system is Monte-Carlo method. Generally speaking, systems of thousands to million particles are not uncommon in Monte-Carlo. The involved interactions among particles will require intensive computation and produce large amount of information. In particular, in case of Heisenberg model, in n-atomic system, we need $O(n^2)$ summation, multiplication and dot products to compute single point of total energy out of its Hamiltonian, because Heisenberg Hamiltonian principally considering all spin-pair interactions in evaluation of total energy of system. Therefore high performance computation like GPU-based parallelism plays a critical role in the success of those simulations using method like Monte-Carlo[7].

5.2.3 GPU memory scheme

1. **Treads**

   A thread is basically a worker with a sequential process, and we can make an analogy to a single core in the context of a multicore CPU. GPU programs are usually written as functions, called 'kernels'. When we write GPU programs ('kernels'), we write them for a thread to execute sequentially. A GPU typically executes thousands of threads, with only sub-groupings of these threads executing concurrently at any given time. Threads have groupings to execute in GPUs and there are two main concepts to grouping threads.

- Warp: GPUs never actually execute a single thread at a time, but groups of threads, called warps. The warp size for most GPUs is 32.
- Block: We can group threads into blocks so that they can communicate via shared memory.

2. **Memory types**

   Figure 5.1 shows schematic description of GPU memory architecture. When we execute kernels (GPU programs), data must initially be transferred from CPU to global memory. We want to minimize global memory transfers, since they are easily and quite often the overall speed bottleneck. To do this, we can utilize shared memory and registers. Figure 5.2 describes memory structure in GPU and trade off between speed and scope. The programmer specifies threads per block and total blocks. Restrictions on maximum registers per thread/block, max shared memory per block, maximum resident blocks per multiprocessor, should be considered carefully for proper GPU resource utilization. If the program calls for too many registers per thread, it gets stored (or 'spilled') in global memory which would be very slow. Thus, defining memory types and allocating shared memory to data is very critical in CUDA coding [115] to speed up the simulation. Actual register usage can be determined by ptxas compiler flag.

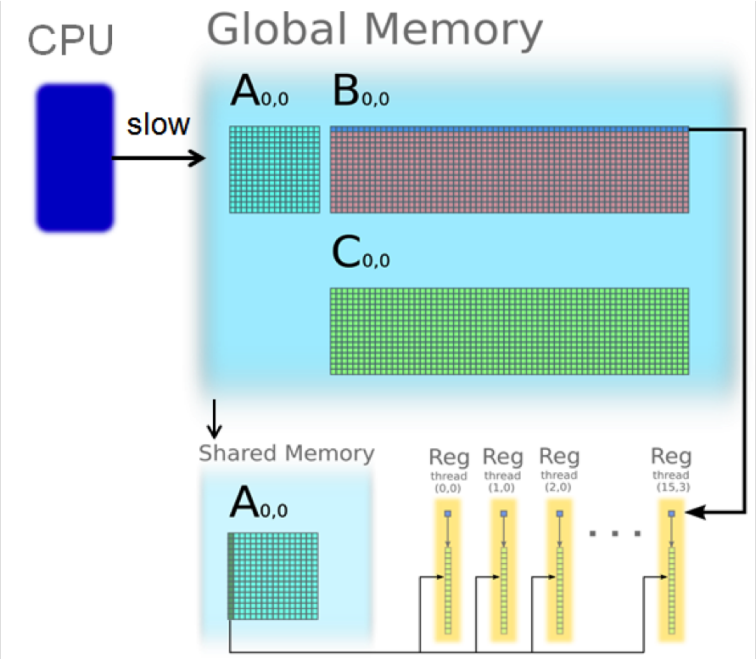

Figure 5.1: Schematic view of CPU and GPU Memory

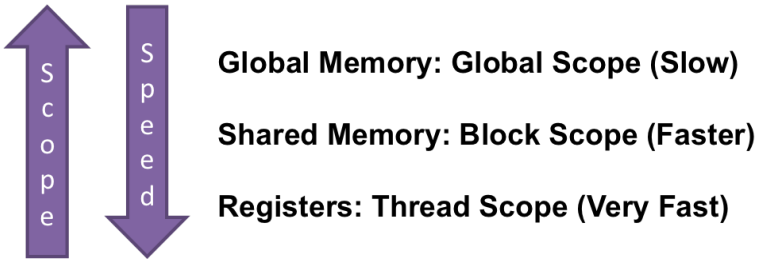

Figure 5.2: Memory types in GPU and trade off between their speed and scope

In our simulation, the global memory transfers required are the current spin states and the random numbers.

5.2.4 Monte Carlo simulation based on Ising model

The Ising Model is a simple model of a solid that exhibits a phase transition resembling ferromagnetism. In this model, there are two big assumptions to simplify the model. First, a spin direction is assigned to each vertex on a graph. Therefore, each spin direction is restricted only either up (+1) or down (-1), though generalized models may include more choices for spin direction. Second, the standard Hamiltonian for an Ising system includes only nearest-neighbor interactions though generalized models may include long-range interactions. The standard Hamiltonian is,

$$H = -J \sum_{neighbor} S_i \cdot S_j \tag{5.1}$$

where J is coupling coefficient which is always same for binary system. (In our case, we have used binary bcc Fe system) In our work, we consider an Ising system on a square grid, where each spin occupied in one thread in checkerboard shaped memory and interacts directly with four neighbors (above, below, to the right, and to the left).

5.3 Computational Method

5.3.1 Checkerboard algorithm

- **Checkerboarding Ising model spin domain**
  Figure 5.3 describe main idea of checkerboarding in typical 2-dimensional Monte-Carlo simulation for spins.[111] As shown, one spin only coupled with its neighbors (in case of 2D, there are 4 neighbors around one spin). Thus, we can use checker board pattern of thread structure to work in parallel. At first step, we

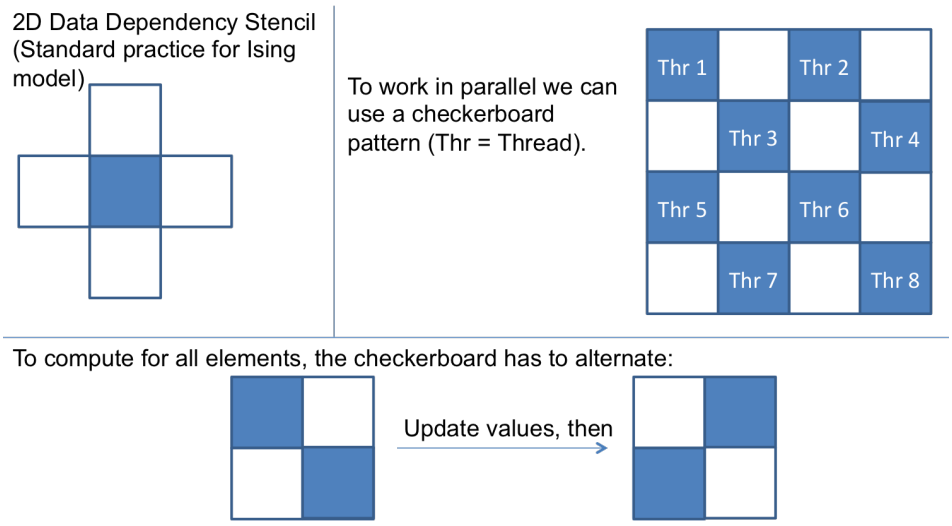

Figure 5.3: Checkerboarding in 2D Monte-Carlo simulation

update spin in blue thread, and we update spin in white thread in following step. By repeating alteration of update in blue and white, we can compute all elements.[63] In our checkboard model, only one spin is occupied in one thread to avoid ignoring long range interaction between boundaries of spin blocks. As memory sharing scheme, a domain of interest for a block of threads can be transferred into shared memory, then reused and rewritten for all threads in the block to share.

Alternatively, the Kepler shuffle functionality can be used for faster communication. As Kepler shuffle functional is more complicate in terms of its algorithm, we have used the first method to use shared memory saving domain of interest for a block of threads.

- **Checkerboard Algorithm**

  To implement the Metropolis Monte-Carlo algorithm on GPU, we use the checkerboard decomposition, which divide the entire lattice into even and odd sites, where a lattice site is said to be even if its Cartesian coordinates add up to an even value. Otherwise it is said to be odd. The procedure then is to first update all spins on even lattice sites, and afterwards to update all spins on odd lattice sites in a second step, where updating a spin means to use the Metropolis acceptance ratio for changing the spin's orientation. After having performed both of the update steps, defining so-called sweep, all spins were taking into account to change their orientation. Subsequently, we denote this

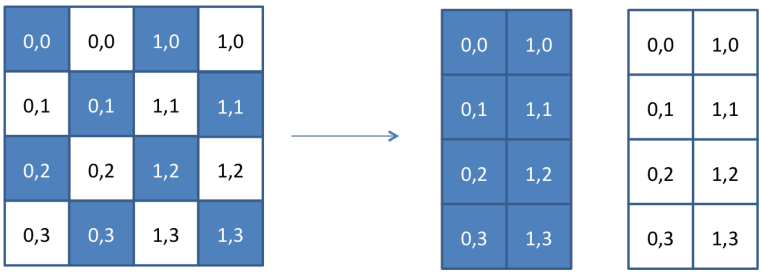

Figure 5.4: Visualization of checkerboard memory shame

way to update the entire lattice as checkerboard procedure.

5.3.2 Memory scheme

- **Global Memory Coalescing :**
  When GPU makes read from global memory, multiple transactions are coalesced, or combined into one, if the memory locations are (near-)contiguous. This allows for optimal global memory bandwidth. The bandwidth may be optimal for Ising int spins (stride = 1 int), but definitely not for Heisenberg (if stored as vector (stride = dimension*float)). When working on one checkerboard, only the other checkerboard is needed in the stencil besides the center. Thus, we can split the spins into 2 separate arrays so that all reads and writes are contiguous. We also reduce shared memory usage by a factor of 2 this way for 2D. This method extends straightforwardly to the 3D case. In 3D, we still have two exclusive sets that can be executed in parallel. In the iso-z-coordinate, the other checkerboard with z coordinate is needed as in 2D.

- **Checkerboard Memory Scheme :**
  In our simulation, the two checkerboard sub-domains are iterated upon in sequence. Because we are synchronizing whole spins per every step, two checkerboard run MC simulation independently at least in single step. Thus, we saved two checkerboard in one shared memory with $n \times \frac{n}{2}$ size rather than save whole spin map in one big memory of $n \times n$ size. Visualization of memory scheme and the stencil in 2D MC simulation is shown in Figure 5.4.

  Here is the stencil formula for $(top + right + bottom + left)$:

  (1) *Evenrow* :
  $Blue(x,y) : (White(x,y-1) + White(x,y) + White(x,y+1) + White(x-1,y))$

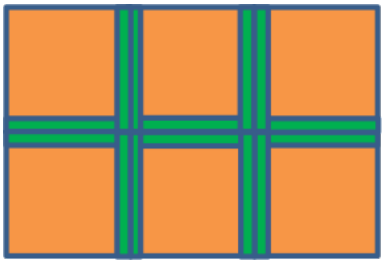

Figure 5.5: The schematic view of shared memory structure of Monte-Carlo simulation

$White(x, y) : (Blue(x, y-1) + Blue(x+1, y) + Blue(x, y+1) + Blue(x, y))$

(2) Odd row:

$Blue(x, y) : (White(x, y-1) + White(x+1, y) + White(x, y+1) + White(x, y))$

$White(x, y) : (Blue(x, y-1) + Blue(x, y) + Blue(x, y+1) + Blue(x-1, y))$

For a given x,y in an even row, white are right neighbors of blue. For a given x,y in an odd row, white are left neighbors of blue.

- **Block Communication :**

  Figure 5.5 represents the schematic view of memory structure of Monte-Carlo simulation.Orange denotes each thread block, and green edge denotes the shared memory communication. We can think as if the block (orange) contains multiple of threads as the checkerboard shape, and each thread occupy single spins. Because we should consider periodic boundary condition in periodic crystal lattice, outermost edges are also green (shared memory communication). As mentioned above, threads are grouped together as block. When GPU execute kernel, it is executed distinctively in multiple blocks. Therefore, we should make each block communicate each other. There are two ways for block communication.

  First method is utilizing shared memory as the bridge for communication between different block. In our model, we consider Ising model which only consider nearest neighboring interacting in updating spin. This has big advantage to utilizing shared memory for block communication in two aspect. First, due to the constrain of nearest neighbor only interaction, each block only communicate it's boundary information each other. Because the only the spin located on the boundary of block communicate with next block, we do not have to care about spin information other than boundary in block communication. Second, because spin update only depend on its nearest neighbor spins, only nearest neighboring blocks communicate each other. Those properties make the block

communication easy and simple. For every Monte-Carlo step, the shared memory write the boundary information from every block, and send them to nearest neighbor block in next step. Then, for every Monte-Carlo step, each block look up the boundary information of nearest block from shared memory and use them to update spins inside. However, in our simulation, we must update all global spin information to global memory since inter-block data cannot be synchronized. Therefore,the results of spins at the boundaries can be rewritten back to global memory so that changes are communicated across block domain boundaries. Thus, there may comes the trade off between the gain from shared memory usage for block communication and the overhead due to global memory synchronization.

Second method is directly write all spin information back to global memory without utilizing shared memory. Although data transfer to global memory is slower than data transfer to shared memory, this method may be faster then previous one when system size is not that big, because we can reduce the overhead from global memory synchronization.

- **Vertical line sharing vs Horizontal line sharing**
  As the new approach to optimize performance specialized on speeding up simulation, we implemented $VerticalLineAlgorithm$. If we compare the memory requirements for checkerboard spin stencil computations between horizontal and vertical traversal, we can see that horizontal calculation requires 3 rows of memory per one line of spin computation, while vertical calculation requires only 2 rows of memory per one line of spin computation. In traversing vertically (on the decomposed checkerboard sets), more of the stencil data is reused.

5.3.3 Random Number Generator

Monte Carlo methods rely mostly on being able to generate random numbers [11, 47, 62], it is really important to mention that having a good random number generator is important to guarantee the quality of the output of Monte Carlo method. The generation of random numbers on a computer is a notoriously difficult problem. An ideal random number generator would provide numbers that are uniformly distributed, uncorrelated, satisfy any statistical test of randomness, have a large period of repetition, can be changed by adjusting an initial seed value, are repeatable, portable, and can

be generated rapidly using minimal computer memory.

In our GPU Monte-Carlo program, we have tried two ways to generating random numbers; (1) Generating all random numbers requires for Monte-Carlo simulation in CPU, and make all of them transferred to the global memory in GPU. (2) Make the random number generated on each thread utilizing NVIDIA CUDA Random Number Generation library (cuRAND).

1. **Transferring RN from CPU to Global Memory**
   First method is generating all random numbers needed for Monte-Carlo simulation in CPU and make all of them transfer to the global memory in GPU, and send them to Kernel via PCI-e. As mentioned above, data transfer from CPU to global memory is the main bottle neck for the speed. Therefore, this method has the disadvantage that it may slow down the speed of Monte-Carlo simulation. However, by testing random numbers in CPU before we use them for Monte-Carlo simulation, we can guarantee the randomness of random numbers. In case of our Monte-Carlo simulation, our system size is about million (10^6) of atoms, and about 10^5 Monte-Carlo steps are preformed to make the system converged. Therefore, we generated 100 billions (10^{11}) random numbers using Mersenne Twister Random Number Generator in CPU and transferred them to global memory. As sequence of 32-bit Mersenne Twister Random Number Generator about $2^{19937} - 1$ which is is much longer than 100 billions, we can gurantee the randomness of generated 100 billions of random numbers.

2. **Use built-in RNG in each thread**
   Second method is generating unique random number in each tread of GPU and use them to update spin. There are two ways to generate random numbers in GPU. First, Generate Random numbers on GPU and use in Kernel. Second, Generate random numbers using Hashing function written inside the kernel. We have used first method utilizing the built-in random number generator library provided by NVIDIA CUDA (cuRAND). This library helps us to generate more than one unique random numbers on each thread based on thread id and/or kernel parameters based on different distribution. We have used XORWOW generator, based on XORShift algorithm, provided from cuRAND library. Random numbers for spin updates are generated for multiple sequences, each sequence based on a set of computed parameters. Contrast with

the first method to generate all random numbers and transfer them to GPU, this method has advantage in terms of fast speed because we do not need to go through CPU to GPU data transfer. However, there is significant disadvantage in that we can never guarantee the performance of those random numbers. This is significant drawback especially in the case of Monte-Carlo simulation as the accuracy of simulation results mainly rely on the quality of random numbers. Therefore, this method is not recommended usually for Monte-Carlo simulation in scientific computing.

5.4 Results

- **Validation of Random Number Generator**

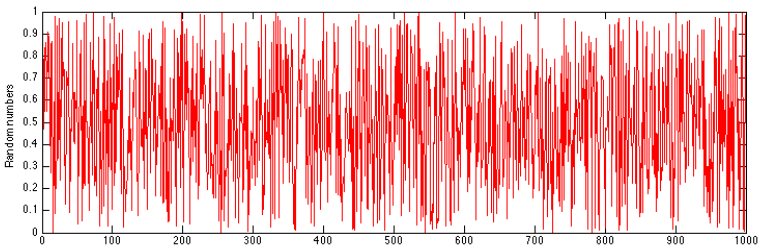

Figure 5.6: Random numbers between 0 to 1 generated by periodic sampling of sequence from Mersenne Twister PRNG

We have tried two methods to generate random numbers mentioned above. For the first method to generate random numbers in CPU and make it transfers to GPU, we have used the Mersenne Twister pseudo random number generator, which is one of the most extensively tested random number generators in existence. In our test sample, our system size has about million (10^6) of atoms, and at least about 10^3 Monte-Carlo steps should have preformed to make the system converged. Therefore, we generate a sequence of random numbers, then sample the random numbers of the sequence with sampling period length of 10^9. We input the sampled random number to each thread, for the threads to use as their random numbers.

We use the Mersenne Twister random number generator [73] utilizing add-on implementations provided in CUDA libraries [54]. Mersenne Twister, the name derives from the fact that it uses a period which is a Mersenne prime. It

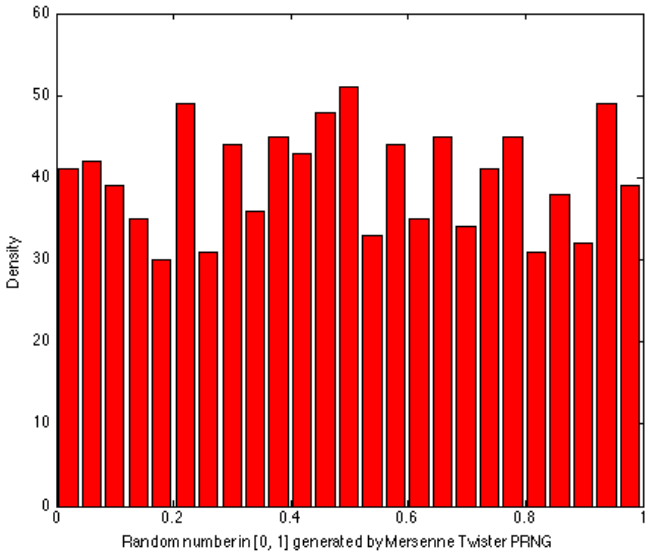

Figure 5.7: Histogram of our generated random numbers between 0 to 1 (1000 data points)

is a modification of a Twisted Generalized Feedback Shift Register (TGFSR) which takes in an incomplete array to realize a Mersenne prime as its period and uses an inversive-decimation method for primitivity testing of a characteristic polynomial of a linear recurrence with a computational complexity of $O(p^2)$ where p is the degree of the polynomial. Using CUDA API, CURAND_RNG_PSEUDO_MT19937, we can generate the random number sequence, as much as $2^{19937}-1$ length long with 32-bit word length, based on the Mersenne prime. The main reason we choose the Mersenne Twister, MT19937, for our Monte-Carlo simulation is we requires long period of random sequence more than 100 billions ($10^{11} \approx 2^{36}$). Mersenne Twister has a very long period of $2^{19937}-1$. While the whole long pereiod of $2^{19937}-1$ is not a guarantee of quality in a random number generator, short periods (such as below than 2^{40} common in many older software packages) cannot be problematic. Therefore, Mersenne Twister can cover 100 billions of random numbers for our Monte-Carlo. For 2^{36} period, it guarantees of quality in a random number generator. It has also known that random numbers from Mersenne Twister pass numerous tests for statistical randomness, including the Diehard tests. Also, It is considered to be fast, as it avoids multiplications and divisions and uses the advantages of cashes and pipelines and efficient in memory use as only 624 words needed for

the working area.

The formula which yields a sequence of pseudo-randomized numbers calculated with a discontinuous piece-wise linear equation. The generator is defined by the recurrence relation:

$$X_{k+n} = X_{k+m} \oplus (x_k^u | x_{k+1}^l)A$$

,where n is the degree of recurrence. Integer m,$1 \leq m \leq n$. x_n is a row vector of a word size w which is generated with k = 0. x_{k+1}^l are lower or rightmost r bits of x_{k+1}, and x_k^u are upper of leftmost $w - r$ bits of x_k. $\oplus$ denotes a bitwise XOR. $(x_k^u | x_{k+1}^l)$ means concatenating the upper $w - r$ bits of x_k and the lower r bits of x_{k+1}^l in order. Therefore, $(x_k^u | x_{k+1}^l)$ is $(x_{w-1}, x_{w-2}, ..., x_0)$. Finally, A is a constant $w \times w$ matrix chosen to ease the matrix multiplication shown below.

$$A = \begin{bmatrix} 0 & 1 & & & \\ 0 & 0 & 1 & & \\ 0 & ... & ... & & \\ & & \ddots & \ddots & \\ & & & \ddots & 1 \\ a_{n-1} & a_{n-2} & a_{n-3} & & a_0 \end{bmatrix}$$

The multiplication of $(x_k^u | x_{k+1}^l)A$ can be performed using simple bit shift operations as shown below.

$$(x_k^u | x_{k+1}^l)A = \begin{cases} x \gg 1, & \text{if } x_0 = 0 \\ (x \gg 1) \oplus (a_{n-1}, a_{n-2}, a_{n-3}, ...a_0), & \text{if } x_0 = 1 \end{cases} \tag{5.2}$$

Therefore, after concatenating the upper $w - r$ bits of x_k and the lower r bits of x_{k+1}^l in order, the matrix A is multiplied from the right by this vector, then bit-wise XOR ($\oplus$) performed to add x_{k+m}, and then generate the next vector x_{k+n}.

To validate our random number generator, we have plotted the sequence of random number by 1000 iterations(Figure 5.6) and the histogram of our 1000 random numbers(Figure 5.7). From our χ^2 goodness-of-fit test, we got 35.40 as χ^2 value when degree of freedom is 50 which shows 95% confidential level in our hypothesis that our random variables are iid (Independent and identically distributed) from uniform distribution. [71]

- **Test Results for Fe**

  In case of simple 2-D checkerboard lattice of 1024x1024 Fe system, the obtained results of mean magnetic moment versus temperature shows similar plot between GPU and CPU as shown in Figure 5.8. GPU plot shows more fluctuations below Curie temperature than CPU plot, and the reason for this is not clear. There are several possible theories. Firstly, It is possible that its because of the different random number generation methods between CPU and GPU. The random number allocation in GPU computing has been done separately per each thread compared with CPU computing which has been used all same random number generator. Secondly, checkerboard scheme we have used to compute in GPU might not efficient to form spin cluster domain. Because each checkerboard thread should be updated in parallel for every other steps, the spin cluster domain will be relatively easily randomized (spin cluster will be easily dissipated again) even though it will have higher probability to be formed in low temperature. This may end up with fluctuated plot in low temperature in GPU case compared with the smooth sigmoid curve in CPU case. To generate this plot, 10^5 Monte-Carlo steps are performed to calculate mean magnetic moment at single temperature point and 200 temperature points are obtained as quenching the temperature from 4500K to 0K. To perform 10^5 Monte-Carlo calculations at single temperature point, the average simulation time took 2101.549219 ms (around 2 seconds) in GPU case and 512778.0094 ms in CPU case (around 9 minutes). Overall speed up for GPU compared with CPU, therefore, has been shown as around 244 times in this case. Both of CPU and GPU plots shows good agreement in its Curie Temperature with experimental value of Tc in Fe system (1400K). Our test result represents that GPU can predict thermo-magnetic spin fluctuation as well as CPU in the simple Iron system.

- **Speed up**

  Interestingly, it has turned out that copying to shared memory does not result in increased performance. For the case of $n = 1024, 2D\ model$, original parallel GPU simulation without shared memory implementation showed 170 x speed up. However, shared memory implementation showed only 116 x speed up which is slightly lower than the case without shared memory. There are possible reasons for this. Firstly, It is because the original un-shared memory code has

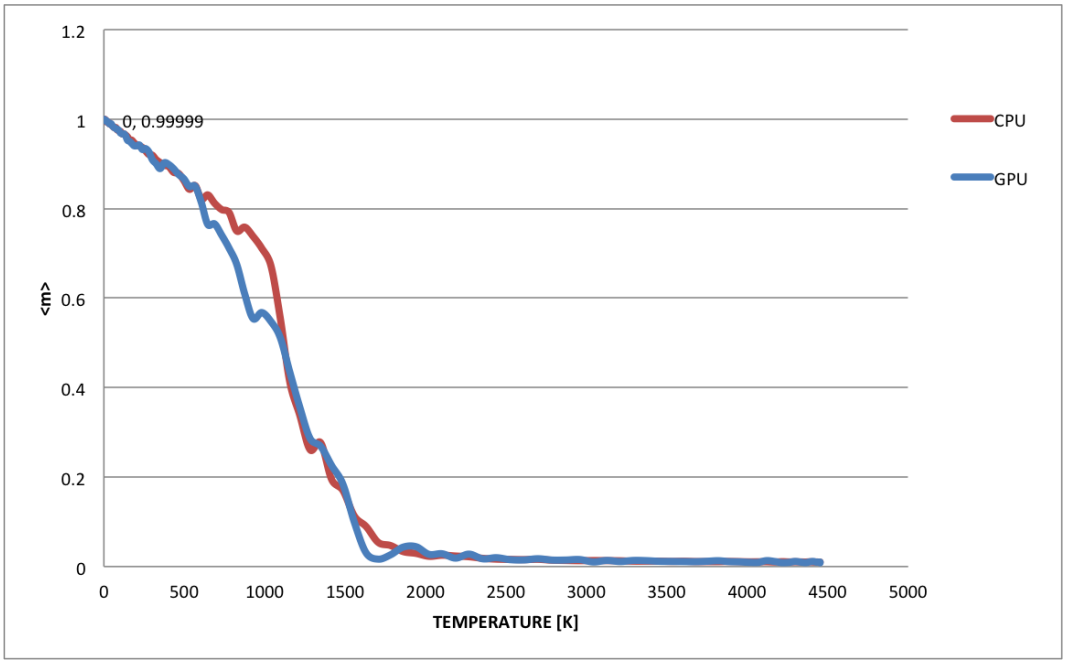

Figure 5.8: Comparison of mean magnetic moment versus temperature in CPU and GPU

no synchronization among all threads after each steps of MC. That means, since the stencil overlap and memory reuse is very low, the synchronization overhead may do not pay off that much. Secondly, code without shared memory performs 2 spin calculations per thread, thus it lead to reuse memory stored in register which may speed up more than shared memory implementation.

As we expected, a vertical line partitioning appears to minimize total memory requirements more effectively. In addition, it also works well in memory coarsening for row major checkerboard storage, because threads concurrently access adjacent memory locations. Thus, we used vertical line partitioning in our simulation. Here are our initial results of performance test using vertical line algorithm in GPU implementation in Table 5.1. Result shows great speed up in our simulation up to 2.4 X by using VLA and modified random number generation scheme. Our results has been compared with optimized baseline in previous works. [88]

Table 5.1: Results from our initial performance test by using Vertical Line Algorithm(VLA) and multiple random number generates per threads in 2-D Ising model

Runtime $L_x = L_y = 1024$	Threads per Block	Line length	Speed Up
Optimized Baseline	512	N/A	170
VLA wt transferring RN from CPU	256	4	204
VLA wt built in RNG in GPU	256	4	225

5.5 Discussion

Our GPU implementation runs **225 times faster** (double precision; 749 times faster in single precision) than the sequential implementation on the Jinx nodes with the M2090 GPU cards for calculations of single Monte Carlo steps in 2D. In case of 3D stencil computation, It is shown that our GPU implementation runs **184 times faster** than sequential algorithm. Both 2D and 3D stencil case, we have used checkerboard algorithm based on Ising model which is interacting only with nearest neighboring threads in considering periodic boundary condition. The simple 2D and 3D checkerboard stencil computations has been considered in our case. The GPU results shows good similarity compared with CPU results in our test case of simple cubic Fe system showing remarkable speedup. We found GPU result shows slight fluctuation in its thermo-magnetization curve in low temperature. It represents slow convergence of GPU than CPU and possibly can be improved by using other parallelization algorithm than checkerboard. It is worth to note that our model is simplified Ising model, and may not be fit for complicate multi-component magnetic system such as $(Fe_{1-x}Co_x)_2B$. In order to implement high performance feature for those systems, parallelization of Heisenberg based Monte-Carlo simulation is required. There is no complete algorithmic scheme for parallelization of Heisenberg model. There was a work use tree-based parallel reduction algorithm to reduce the sum of all pair interaction in sphere boundary of each atom, but the minimum computational complexity is still $O(nlog(n))$. It would be great future work and achievement in scientific computing community, if we can come up with brilliant parallel algorithm for Heisenberg Monte-Carlo simulation.

Chapter VI

CONCLUSION

In this work, I review and compare various computational modeling techniques for predicting thermos-magnetic properties of materials by applying those computational modeling approaches in the different systems. I also propose new computational modeling routine based currently available methods. Here, I would like to draw conclusions from our results.

6.1 DFT calculation for $MnBi$

In Chapter 2, we have investigated the thermomagnetic properties of $MnBi$ and $MnSb$ as a function of electronic temperature for the $NiAs$, MnP and *zincblende* structures. The first principles calculation has shown good agreement with experimental structural and thermomagnetic results for $MnBi$ and $MnSb$. Comparing results from the $NiAs$, MnP and $zincblende - type$ structures, our results clearly show a structural role in the thermomagnetic behavior of these compounds, with marked temperature sensitivity for $MnBi$ in its room temperature $NiAs$-type structure. $MnSb$ shows little temperature dependence. The magnetization of $MnSb$ and $MnBi$ in the MnP structure is markedly lower than the distorted $Zincblende$ values. Using thermal expansion effects derived from experimental measurement, total magnetization of $MnBi$ shows a small increase with larger cell volumes. Cold smearing method discussed in Chapter 2, however, only mimic the non-zero temperature by smearing electronic distribution function. This is because of that the ab-initio density functional theory calculation doesn't initially have a temperature variable in its Hamiltonian, and we couldn't fully take account statistical thermal effects. Due to this zero-temperature constraint of first principle DFT calculation, the change in the total magnetization of $MnBi$ over the temperature range up to 300K for the static structure was less than $0.1\mu B$, while for the expanding unit cell with temperature range up to 600K, the change is also small, less than $0.1\mu B$.

These observations point toward two problems of the approach Chapter 2. First, the

broadening of electronic occupation numbers by the smearing method is too small since the lattice temperature remained in a static ground state in our calculation.

Second, spin reorientation effect in $MnBi$ observed in the 90K – 150K temperature range could be existed. Scalar relativistic pseudo potentials, which I used in our previous work, do not fully take into account spin-orbit coupling effects, although previous investigation has estimated these to be small. Also, the collinear magnetic spin representation used in current ab-initio DFT software package doesn't consider spin rotation with every spherical orientation which is detrimental to predict spin reorientation effect.

To address the temperature dependent magnetic spin fluctuation and spin reorientation effect with full rotation of spin, Monte-Carlo simulation using Heisenberg model may be explored as alternative computational methodologies.

6.2 Predicting T_c for $(Fe_{1-x}Co_x)_2B$

The problem addressed in Chapter 2 have been resolved resolved by combining Monte Carlo simulation with DFT. The observation of Curie temperature in $(Fe_{1-x}Co_x)_2B$ in Chapter 3 showed, Monte-Carlo simulation of thermal fluctuation of magnetic moment can statistically address spin orbit coupling and dynamics in high temperature. Heisenberg model considering every spherical orientation of magnetic spin moment will achieve our aim to represent accurate spin reorientation in finite temperature.

The modeling routine have three steps of procedure,

- Step 1: Obtaining coupling constant J_{ij} in Heisenberg Hamiltonian from ab-initio KKR-CPA calculation in zero-temperature.
- Step 2: Plug in J_{ij} parameters between each atoms and experimental magnetic moments of Fe, Co and B in our Monte-Carlo source code.
- Step 3: Run the Monte-Carlo simulation and obtaining snap shot of spin dynamics and Curie temperature.

The result from our simulation procedure shows great agreement with experimental values. Compared with mean-field DFT calculation which is overestimated Tc about 40%, the agreement is excellent, though notable deviations can be seen for small x.

6.3 Stacking Fault Energy of $Fe - Cr - Ni$ Stainless Steels

Using thorough computational approach combining DFT and Monte-Carlo simulation based on LSF model, the magnetic contribution term of SFE due to the spin fluctuation is successfully evaluated. In this new computational modeling routine, we have successfully calculated and quantified the temperature dependent magnetic/spin entropy for a 64-atom system. Our results are in agreement with what has been reported in previous literature. We have divide stacking fault energy of the system by two term which is enthalpy contribution and magnetic entropy contribution, and summed two term after obtain two terms separately. The enthalpy contribution has been obtained by ground state DFT calculation in paradigmatic state with constraining magnetic moments, and the magnetic entropy contribution has been obtained by spin Monte Carlo simulation based on LSF model. The estimated magnetic/spin entropy contribution to the SFE as a function of temperature is shown. Our result indicates that with increasing temperature the magnetic/spin entropy increases, due to increased magnetic fluctuation, which will ultimately increase the SFE.

6.4 GPU implementation on Monte-Carlo simulation

In Chapter 3, our Heisenberg Monte-Carlo simulation predicts quite accurate Currie temperatures of $(Fe_{1-x}Co_x)_2B$ which is almost same with experimental values. Thus, we have validated the simulation model in terms of its functionality. However, there are large portion of area to be improved in terms of its efficiency. Especially, our Monte-Carlo software took about 13 seconds to run 1000 atomic system at one finite temperature point, which is quite slow. At current stage of our research, it was okay. Because the Monte-Carlo software package had been mainly used to calculate Currie temperature of $(Fe_{1-x}Co_x)_2B$ families, and the number of atoms of our system in Chapter 3 hasn't been exceeding 1000 atoms for every simulation. However, to mimic the real physical phenomenon as accurate as possible, the source code should be able to extend to the many-body system, such as several millions of spins, which is capable to consider defect, pinning or vacancy in atoms.

To resolve this issue, we suggest new software package implementing higher-fidelity features within our Monte-Carlo source code based on Ising model. The package we developed supports parallelization, by taking advantage of Graphical Processing Units. By implementing a variant of the checkerboard algorithm, we obtain faster

calculation on the GPU than on a CPU core. Our result of Monte Carlo simulation for millions of Fe atoms shows our GPU algorithm is 2.4X faster than previous work of the 2D Ising problem. For a 2D 1024×1024 atomic system, the speedup was 200X over optimized sequential CPU code.

REFERENCES

[1] Afshin Abbasi, Alexey Dick, Tilmann Hickel, and Jörg Neugebauer. First-principles investigation of the effect of carbon on the stacking fault energy of fe–c alloys. *Acta Materialia*, 59(8):3041–3048, 2011.

[2] Afshin Abbasi, Alexey Dick, Tilmann Hickel, and Jörg Neugebauer. First-principles investigation of the effect of carbon on the stacking fault energy of fe–c alloys. *Acta Materialia*, 59(8):3041–3048, 2011.

[3] S Allain, J-P Chateau, O Bouaziz, S Migot, and N Guelton. Correlations between the calculated stacking fault energy and the plasticity mechanisms in fe–mn–c alloys. *Materials Science and Engineering: A*, 387:158–162, 2004.

[4] Joshua A Anderson, Chris D Lorenz, and Alex Travesset. General purpose molecular dynamics simulations fully implemented on graphics processing units. *Journal of Computational Physics*, 227(10):5342–5359, 2008.

[5] VP Antropov and VN Antonov. Colossal anisotropy of the magnetic properties of doped lithium nitrodometalates. *Physical Review B*, 90(9):094406, 2014.

[6] Andreu Badal and Aldo Badano. Accelerating monte carlo simulations of photon transport in a voxelized geometry using a massively parallel graphics processing unit. *Medical physics*, 36(11):4878–4880, 2009.

[7] Kurt Binder and Dieter Heermann. *Monte Carlo simulation in statistical physics: an introduction*. Springer Science & Business Media, 2010.

[8] Eric Bousquet and Nicola Spaldin. J dependence in the lsda+ u treatment of noncollinear magnets. *Physical Review B*, 82(22):220402, 2010.

[9] Ian Buck. Gpu computing with nvidia cuda. In *SIGGRAPH*, volume 7, page 6, 2007.

[10] M Cardona, NE Christensen, and G Fasol. Relativistic band structure and spin-orbit splitting of zinc-blende-type semiconductors. *Physical Review B*, 38(3):1806, 1988.

[11] Paul D Coddington. Analysis of random number generators using monte carlo simulation. *International Journal of Modern Physics C*, 5(03):547–560, 1994.

[12] R Coehoorn and RA De Groot. The electronic structure of mnbi. *Journal of Physics F: Metal Physics*, 15(10):2135, 1985.

[13] JMD Coey. Permanent magnet applications. *Journal of Magnetism and Magnetic Materials*, 248(3):441–456, 2002.

[14] Pierre-Jean Cunat. Alloying elements in stainless steel and other chromium-containing alloys. *Euro Inox*, 2004:1–24, 2004.

[15] FERMI SURFACE DATA. Experimental muffin tin potential parameters.

[16] RW De Blois and DS Rodbell. Magnetic first-order phase transition and anisotropy in single-crystal mnas. *Journal of Applied Physics*, 34(4):1101–1103, 1963.

[17] Stefano de Gironcoli. Lattice dynamics of metals from density-functional perturbation theory. *Physical Review B*, 51(10):6773, 1995.

[18] A Debernardi, M Alouani, and H Dreyssé. Ab initio thermodynamics of metals: Al and w. *Physical Review B*, 63(6):064305, 2001.

[19] Paul AM Dirac. On the theory of quantum mechanics. In *Proceedings of the Royal Society of London A: Mathematical, Physical and Engineering Sciences*, volume 112, pages 661–677. The Royal Society, 1926.

[20] Eleftherios N Economou. *Green's functions in quantum physics*, volume 3. Springer, 1984.

[21] JS Faulkner and GM Stocks. Calculating properties with the coherent-potential approximation. *Physical Review B*, 21(8):3222, 1980.

[22] Enrico Fermi. Sulla quantizzazione del gas perfetto monoatomico. *Rend. Lincei*, 3:145–149, 1926.

[23] Eric B Ford. Parallel algorithm for solving keplerâĂŹs equation on graphics processing units: Application to analysis of doppler exoplanet searches. *New Astronomy*, 14(4):406–412, 2009.

[24] Christoph Friedrich, Stefan Blügel, and Arno Schindlmayr. Efficient implementation of the g w approximation within the all-electron flapw method. *Physical Review B*, 81(12):125102, 2010.

[25] Mark S Friedrichs, Peter Eastman, Vishal Vaidyanathan, Mike Houston, Scott Legrand, Adam L Beberg, Daniel L Ensign, Christopher M Bruns, and Vijay S Pande. Accelerating molecular dynamic simulation on graphics processing units. *Journal of computational chemistry*, 30(6):864–872, 2009.

[26] Georg Frommeyer, Udo Brüx, and Peter Neumann. Supra-ductile and high-strength manganese-trip/twip steels for high energy absorption purposes. *ISIJ international*, 43(3):438–446, 2003.

[27] C-L Fu and K-M Ho. First-principles calculation of the equilibrium ground-state properties of transition metals: Applications to nb and mo. *Physical Review B*, 28(10):5480, 1983.

[28] Luigi Genovese, Matthieu Ospici, Thierry Deutsch, Jean-François Méhaut, Alexey Neelov, and Stefan Goedecker. Density functional theory calculation on many-cores hybrid central processing unit-graphic processing unit architectures. *The Journal of chemical physics*, 131(3):034103, 2009.

[29] Xavier Gonze, B Amadon, P-M Anglade, J-M Beuken, F Bottin, P Boulanger, F Bruneval, D Caliste, R Caracas, M Cote, et al. Abinit: First-principles approach to material and nanosystem properties. *Computer Physics Communications*, 180(12):2582–2615, 2009.

[30] O Grässel, L Krüger, G Frommeyer, and LW Meyer. High strength fe–mn–(al, si) trip/twip steels developmentâĂŤpropertiesâĂŤapplication. *International Journal of Plasticity*, 16(10):1391–1409, 2000.

[31] Göran Grimvall. Spin disorder in paramagnetic fcc iron. *Physical Review B*, 39(16):12300, 1989.

[32] Daniel Gross, Ulrich Heil, Ralf Schulze, Elmar Schoemer, and Ulrich Schwanecke. Gpu-based volume reconstruction from very few arbitrarily aligned x-ray images. *SIAM Journal on Scientific Computing*, 31(6):4204–4221, 2009.

[33] Xuejun Gu, Dongju Choi, Chunhua Men, Hubert Pan, Amitava Majumdar, and Steve B Jiang. Gpu-based ultra-fast dose calculation using a finite size pencil beam model. *Physics in medicine and biology*, 54(20):6287, 2009.

[34] Xuejun Gu, Hubert Pan, Yun Liang, Richard Castillo, Deshan Yang, Dongju Choi, Edward Castillo, Amitava Majumdar, Thomas Guerrero, and Steve B Jiang. Implementation and evaluation of various demons deformable image registration algorithms on a gpu. *Physics in medicine and biology*, 55(1):207, 2009.

[35] Ch Guillaud and J Wyart. Particular polymorphism of the mnas compound at temperatures of disparition and reappearance of spontaneous magnetisation. *Comptes Rendus Hebdomadaires Des Seances De L Academie Des Sciences*, 219:393–395, 1944.

[36] Nail A Gumerov and Ramani Duraiswami. Fast multipole methods on graphics processors. *Journal of Computational Physics*, 227(18):8290–8313, 2008.

[37] BL Gyorffy, DD Johnson, FJ Pinski, DM Nicholson, and GM Stocks. The electronic structure and the state of compositional order in metallic alloys. In *Alloy Phase Stability*, pages 421–468. Springer, 1989.

[38] BL Györffy and GM Stocks. First principles band theory for random metallic alloys. In *Electrons in Disordered Metals and at Metallic Surfaces*, pages 89–192. Springer, 1979.

[39] J Häglund, A Fernández Guillermet, G Grimvall, and M Körling. Theory of bonding in transition-metal carbides and nitrides. *Physical Review B*, 48(16):11685, 1993.

[40] Chris Harris, Karen Haines, and Lister Staveley-Smith. Gpu accelerated radio astronomy signal convolution. *Experimental Astronomy*, 22(1-2):129–141, 2008.

[41] Seyed Arsalan Hashemi, Hojjat Gholizadeh, and Hadi Akbarzadeh. The role of temperature and magnetic effects on the stacking-fault energy in austenitic iron. *arXiv preprint arXiv:1505.00431*, 2015.

[42] Patrik Henelius and Anders W Sandvik. Sign problem in monte carlo simulations of frustrated quantum spin systems. *Physical Review B*, 62(2):1102, 2000.

[43] John P Hirth and Jens Lothe. Theory of dislocations. 1982.

[44] Pierre Hohenberg and Walter Kohn. Inhomogeneous electron gas. *Physical review*, 136(3B):B864, 1964.

[45] Atsushi Iga. Magnetocrystalline anisotropy in $(fe_{1-x}co_x)_2b$ system. *Japanese Journal of Applied Physics*, 9(4):415, 1970.

[46] Oscar Iglesias and Amílcar Labarta. Finite-size and surface effects in maghemite nanoparticles: Monte carlo simulations. *Physical Review B*, 63(18):184416, 2001.

[47] Frederick James. A review of pseudorandom number generators. *Computer Physics Communications*, 60(3):329–344, 1990.

[48] HJF Jansen. Magnetic anisotropy. In *Science and Technology of Nanostructured Magnetic Materials*, pages 349–365. Springer, 1991.

[49] DD Johnson, DM Nicholson, FJ Pinski, BL Gyorffy, and GM Stocks. Density-functional theory for random alloys: Total energy within the coherent-potential approximation. *Physical review letters*, 56(19):2088, 1986.

[50] DD Johnson, DM Nicholson, FJ Pinski, BL Györffy, and GM Stocks. Total-energy and pressure calculations for random substitutional alloys. *Physical Review B*, 41(14):9701, 1990.

[51] Noriaki Kazama and Hiroshi Watanabe. Magnetic properties of $cr_{1-x}mn_x$ as system. *Journal of the Physical Society of Japan*, 30(5):1319–1329, 1971.

[52] S Kibey, JB Liu, MJ Curtis, DD Johnson, and H Sehitoglu. Effect of nitrogen on generalized stacking fault energy and stacking fault widths in high nitrogen steels. *Acta materialia*, 54(11):2991–3001, 2006.

[53] S Kibey, JB Liu, MJ Curtis, DD Johnson, and H Sehitoglu. Effect of nitrogen on generalized stacking fault energy and stacking fault widths in high nitrogen steels. *Acta materialia*, 54(11):2991–3001, 2006.

[54] David Kirk et al. Nvidia cuda software and gpu parallel computing architecture. In *ISMM*, volume 7, pages 103–104, 2007.

[55] Walter Kohn and Lu Jeu Sham. Self-consistent equations including exchange and correlation effects. *Physical review*, 140(4A):A1133, 1965.

[56] Walter Kohn and Lu Jeu Sham. Self-consistent equations including exchange and correlation effects. *Physical Review*, 140(4A):A1133, 1965.

[57] Wo Kohn and No Rostoker. Solution of the schrödinger equation in periodic lattices with an application to metallic lithium. *Physical Review*, 94(5):1111, 1954.

[58] G Kresse and J Furthmüller. Software vasp, vienna (1999). *Phys. Rev. B*, 54(11):169, 1996.

[59] MD KuzâĂŹmin, KP Skokov, H Jian, I Radulov, and O Gutfleisch. Towards high-performance permanent magnets without rare earths. *Journal of Physics: Condensed Matter*, 26(6):064205, 2014.

[60] David P Landau and Kurt Binder. *A guide to Monte Carlo simulations in statistical physics*. Cambridge university press, 2014.

[61] P Larson, II Mazin, and DA Papaconstantopoulos. Calculation of magnetic anisotropy energy in $smco_5$. *Physical Review B*, 67(21):214405, 2003.

[62] Pierre L'Ecuyer. Random numbers for simulation. *Communications of the ACM*, 33(10):85–97, 1990.

[63] Che-Rung Lee, Zhi-Hung Chen, and Quey-Liang Kao. Parallelizing the hamiltonian computation in dqmc simulations: Checkerboard method for sparse matrix exponentials on multicore and gpu. In *Parallel and Distributed Processing Symposium Workshops & PhD Forum (IPDPSW), 2012 IEEE 26th International*, pages 1889–1897. IEEE, 2012.

[64] A Il Liechtenstein, MI Katsnelson, VP Antropov, and VA Gubanov. Local spin density functional approach to the theory of exchange interactions in ferromagnetic metals and alloys. *Journal of Magnetism and Magnetic Materials*, 67(1):65–74, 1987.

[65] AI Liechtenstein, MI Katsnelson, and VA Gubanov. Exchange interactions and spin-wave stiffness in ferromagnetic metals. *Journal of Physics F: Metal Physics*, 14(7):L125, 1984.

[66] Yongsheng Liu, Lin Peng, Jincang Zhang, Zhongming Ren, Jingjing Yang, Zhenglong Yang, Shixun Cao, and Wenjian Fang. Evidence of magnetic anisotropy and spin-reorientation in the textured mnbi crystal. *EPL (Europhysics Letters)*, 96(2):27015, 2011.

[67] EY Loh Jr, JE Gubernatis, RT Scalettar, SR White, DJ Scalapino, and RL Sugar. Sign problem in the numerical simulation of many-electron systems. *Physical Review B*, 41(13):9301, 1990.

[68] GG Lonzarich. Electron, edited by m. springford, 1997.

[69] AK Majumdar and P v Blanckenhagen. Magnetic phase diagram of fe 8 0- x ni x cr 20 (10âĽd' xâĽd' 30) alloys. *physical Review B*, 29(7):4079, 1984.

[70] Richard M Martin. *Electronic structure: basic theory and practical methods*. Cambridge university press, 2004.

[71] Wendy L Martinez and Angel R Martinez. *Computational statistics handbook with MATLAB*. CRC press, 2012.

[72] Nicola Marzari, David Vanderbilt, Alessandro De Vita, and MC Payne. Thermal contraction and disordering of the al (110) surface. *Physical review letters*, 82(16):3296, 1999.

[73] Makoto Matsumoto and Takuji Nishimura. Mersenne twister: a 623-dimensionally equidistributed uniform pseudo-random number generator. *ACM Transactions on Modeling and Computer Simulation (TOMACS)*, 8(1):3–30, 1998.

[74] Chunhua Men, Xuejun Gu, Dongju Choi, Amitava Majumdar, Ziyi Zheng, Klaus Mueller, and Steve B Jiang. Gpu-based ultrafast imrt plan optimization. *Physics in medicine and biology*, 54(21):6565, 2009.

[75] Jeremy S Meredith, Gonzalo Alvarez, Thomas A Maier, Thomas C Schulthess, and Jeffrey S Vetter. Accuracy and performance of graphics processors: A quantum monte carlo application case study. *Parallel Computing*, 35(3):151–163, 2009.

[76] Ferenc Molnár, Tamas Szakaly, Robert Meszaros, and Istvan Lagzi. Air pollution modelling using a graphics processing unit with cuda. *Computer Physics Communications*, 181(1):105–112, 2010.

[77] Hendrik J Monkhorst and James D Pack. Special points for brillouin-zone integrations. *Physical Review B*, 13(12):5188, 1976.

[78] K Motizuki, K Katoh, and A Yanase. Electronic band structures of nias-type compounds. i. nonmagnetic state. *Journal of Physics C: Solid State Physics*, 19(4):495, 1986.

[79] KK Murata and S Doniach. Theory of magnetic fluctuations in itinerant ferromagnets. *Physical Review Letters*, 29(5):285, 1972.

[80] TK Nath, N Sudhakar, EJ McNiff, and AK Majumdar. Magnetization study of γ-fe 80- x ni x cr 20 (14âľ¡ xâľ¡ 30) alloys to 20 t. *Physical Review B*, 55(18):12389, 1997.

[81] Kaan Oguz and JMD Coey. Room-temperature magnetoresistance in cofeb/sto/cofeb magnetic tunnel junctions. *Journal of Magnetism and Magnetic Materials*, 321(8):1009–1011, 2009.

[82] Marek Pajda, J Kudrnovskỳ, Ilja Turek, Vaclav Drchal, and Patrick Bruno. Ab initio calculations of exchange interactions, spin-wave stiffness constants, and curie temperatures of fe, co, and ni. *Physical Review B*, 64(17):174402, 2001.

[83] Mike C Payne, Michael P Teter, Douglas C Allan, TA Arias, and JD Joannopoulos. Iterative minimization techniques for ab initio total-energy calculations: molecular dynamics and conjugate gradients. *Reviews of Modern Physics*, 64(4):1045, 1992.

[84] Wolfgang Pfeiler. *Alloy physics: a comprehensive reference*. John Wiley & Sons, 2008.

[85] FJ Pinski, J Staunton, BL Gyorffy, Duane D Johnson, and GM Stocks. Ferromagnetism versus antiferromagnetism in face-centered-cubic iron. *Physical review letters*, 56(19):2096, 1986.

[86] Tobias Preis, Wolfgang Paul, and Johannes J Schneider. Fluctuation patterns in high-frequency financial asset returns. *EPL (Europhysics Letters)*, 82(6):68005, 2008.

[87] Tobias Preis, Peter Virnau, Wolfgang Paul, and Johannes J Schneider. Accelerated fluctuation analysis by graphic cards and complex pattern formation in financial marketssupplementary information can be found on http://www. tobiaspreis. de. *New Journal of Physics*, 11(9):093024, 2009.

[88] Tobias Preis, Peter Virnau, Wolfgang Paul, and Johannes J Schneider. Gpu accelerated monte carlo simulation of the 2d and 3d ising model. *Journal of Computational Physics*, 228(12):4468–4477, 2009.

[89] P Ravindran, A Delin, P James, B Johansson, JM Wills, Rajeev Ahuja, and O Eriksson. Magnetic, optical, and magneto-optical properties of mnx (x= as, sb, or bi) from full-potential calculations. *Physical Review B*, 59(24):15680, 1999.

[90] BW Roberts. Neutron diffraction study of the structures and magnetic properties of manganese bismuthide. *Physical Review*, 104(3):607, 1956.

[91] Xianwei Sha and RE Cohen. Lattice dynamics and thermodynamics of bcc iron under pressure: First-principles linear response study. *Physical Review B*, 73(10):104303, 2006.

[92] A Siegel, K Parlinski, and UD Wdowik. Ab initio calculation of structural phase transitions in aln crystal. *Physical Review B*, 74(10):104116, 2006.

[93] Travis Sjostrom, Frank E Harris, and SB Trickey. Temperature-dependent behavior of confined many-electron systems in the hartree-fock approximation. *Physical Review B*, 85(4):045125, 2012.

[94] Ralph Skomski. Nanomagnetics. *Journal of Physics: Condensed Matter*, 15(20):R841, 2003.

[95] Petros Souvatzis and Olle Eriksson. Ab initio calculations of the phonon spectra and the thermal expansion coefficients of the 4 d metals. *Physical Review B*, 77(2):024110, 2008.

[96] Paul Soven. Coherent-potential model of substitutional disordered alloys. *Physical Review*, 156(3):809, 1967.

[97] JB Staunton, BL Gyorffy, DD Johnson, FJ Pinski, and GM Stocks. Local density theory of magnetism and its interrelation with compositional order in alloys. In *Alloy Phase Stability*, pages 469–507. Springer, 1989.

[98] JB Staunton, J Poulter, B Ginatempo, E Bruno, and Duane D Johnson. Spin fluctuations in nearly magnetic metals from ab initio dynamical spin susceptibility calculations: Application to pd and cr 95 v 5. *Physical Review B*, 62(2):1075, 2000.

[99] Lutz Steinbeck, Manuel Richter, and Helmut Eschrig. Itinerant-electron magnetocrystalline anisotropy energy of yco_5 and related compounds. *Physical Review B*, 63(18):184431, 2001.

[100] Takanobu Suzuki and Hideaki Ido. Relation between structural and magnetic properties of compound $mnas_{1-x}p_x$ ($0 \leq x \leq 0.275$). *Journal of the Physical Society of Japan*, 51(10):3149–3156, 1982.

[101] Lajos Takacs, MC Cadeville, and I Vincze. Mossbauer study of the intermetallic compounds $(fe_{1-x}co_x)_2b$ and $(fe_{1-x}co_x)b$. *Journal of Physics F: Metal Physics*, 5(4):800, 1975.

[102] DW Taylor. Vibrational properties of imperfect crystals with large defect concentrations. *Physical Review*, 156(3):1017, 1967.

[103] Zeike A Taylor, Olivier Comas, Mario Cheng, Josh Passenger, David J Hawkes, David Atkinson, and Sébastien Ourselin. On modelling of anisotropic viscoelasticity for soft tissue simulation: Numerical solution and gpu execution. *Medical image analysis*, 13(2):234–244, 2009.

[104] Cole Trapnell and Michael C Schatz. Optimizing data intensive gpgpu computations for dna sequence alignment. *Parallel computing*, 35(8):429–440, 2009.

[105] Norman Troullier and José Luriaas Martins. Efficient pseudopotentials for plane-wave calculations. *Physical Review B*, 43(3):1993, 1991.

[106] Ivan S Ufimtsev and Todd J Martinez. Quantum chemistry on graphical processing units. 1. strategies for two-electron integral evaluation. *Journal of Chemical Theory and Computation*, 4(2):222–231, 2008.

[107] M Veithen, Xavier Gonze, and Ph Ghosez. Electron localization: Band-by-band decomposition and application to oxides. *Physical Review B*, 66(23):235113, 2002.

[108] Levente Vitos, Pavel A Korzhavyi, and Börje Johansson. Evidence of large magnetostructural effects in austenitic stainless steels. *Physical review letters*, 96(11):117210, 2006.

[109] Levente Vitos, Pavel A Korzhavyi, JO Nilsson, and Börje Johansson. Stacking fault energy and magnetism in austenitic stainless steels. *Physica Scripta*, 77(6):065703, 2008.

[110] Levente Vitos, J-O Nilsson, and Börje Johansson. Alloying effects on the stacking fault energy in austenitic stainless steels from first-principles theory. *Acta Materialia*, 54(14):3821–3826, 2006.

[111] Martin Weigel. Simulating spin models on gpu. *Computer Physics Communications*, 182(9):1833–1836, 2011.

[112] BTM Willis and HP Rooksby. Magnetic transitions and structural changes in hexagonal manganese compounds. *Proceedings of the Physical Society. Section B*, 67(4):290, 1954.

[113] H Winter and GM Stocks. Calculation of self-consistent potentials for substitutionally disordered systems with application to the $ag_x - pd_{1-x}$ alloy series. *Physical Review B*, 27(2):882, 1983.

[114] JB Yang, William B Yelon, William Joseph James, Qingsheng Cai, M Kornecki, Samit Roy, Naushad Ali, and Ph lâĂŹHeritier. Crystal structure, magnetic properties and electronic structure of the mnbi intermetallic compound. *Journal of Physics: Condensed Matter*, 14(25):6509, 2002.

[115] Zhiyi Yang, Yating Zhu, and Yong Pu. Parallel image processing based on cuda. In *Computer Science and Software Engineering, 2008 International Conference on*, volume 3, pages 198–201. IEEE, 2008.

[116] Koji Yasuda. Accelerating density functional calculations with graphics processing unit. *Journal of Chemical Theory and Computation*, 4(8):1230–1236, 2008.

[117] Junqi Yin and DP Landau. Phase diagram and critical behavior of the square-lattice ising model with competing nearest-neighbor and next-nearest-neighbor interactions. *Physical Review E*, 80(5):051117, 2009.

[118] K Yonehara, K Adachi, M OGASAWARA, N BABA, and K KANAYA. Application of a diffusion-model of an ion-beam penetrating a target to the specimen preparation technique in electron-microscopy. *Journal of Electron Microscopy*, 37(5):278–278, 1988.

[119] Jan Zabloudil, Robert Hammerling, László Szunyogh, and Peter Weinberger. *Electron Scattering in Solid Matter: a theoretical and computational treatise*, volume 147. Springer Science & Business Media, 2006.

[120] Jin-Cheng Zheng and James W Davenport. Ferromagnetism and stability of half-metallic mnsb and mnbi in the strained zinc-blende structure: Predictions from full potential and pseudopotential calculations. *Physical Review B*, 69(14):144415, 2004.

[121] Jin-Cheng Zheng, Michael C Payne, Yuan Ping Feng, and Adele Tzu-Lin Lim. Stability and electronic properties of carbon phosphide compounds with 1: 1 stoichiometry. *Physical Review B*, 67(15):153105, 2003.